# GOLD-CONTAINING BIMETALLIC NANOPARTICLES

by

DUNG TRUNG TRAN

A thesis submitted to

The University of Birmingham

for the degree of

DOCTOR OF PHILOSOPHY

School of Metallurgy and Materials

University of Birmingham

September 2010

# ABSTRACT

This thesis describes computational studies, syntheses and characterization of Cu-Au, Pd-Au, and Pt-Au bimetallic nanoparticles. The computational methodology is a combination of a genetic algorithm coupled with an empirical potential and density functional theory, which is used to study theoretically the geometrical structure, chemical configuration, and electronic properties of 38-atom Cu-Au and 40-atom Pt-Au nanoparticles. Experimental Cu-Au and Pt-Au nanoparticles are synthesized by wet-chemical methods: the two-phase method combined with a galvanic exchange procedure (dodecanethiol-stabilized Cu-Au nanoparticles), the polyol method (Polyvinylpyrrolidone-stabilized Pt-Au nanoparticles), and the Turkevich-Frens method combined with a successive reduction procedure (citrate-stabilized Pt-Au nanoparticles). The Pd-Au nanoparticles which are characterized in our work were synthesized by a microbial method. The nanoparticles are characterized using transmission electron microscopy (TEM) and scanning TEM (STEM) combined with high angle annular dark field (HAADF) imaging, energy dispersive X-ray elemental mapping using a silicon drift detector (SDD), tomography, and electron energy loss spectroscopy (EELS). Sizes and shapes of the Cu-Au, Pd-Au, and Pt-Au nanoparticles are studied by TEM. Morphological evolution and aggregation of the Cu-Au nanoparticles are also observed under the TEM electron beam. SDD-EDX elemental mapping combined with HAADF contrast is used to study the chemical configuration of all the three systems. HAADF-STEM tomography is performed for the Pd-Au nanoparticles. Surface plasmon resonances of the Cu-Au and Pd-Au nanoparticles are studied using EELS. The structures and configurations of the theoretical bimetallic clusters and the experimental bimetallic nanoparticles are found to be composition-dependent.

# ACKNOWLEDGEMENTS

The first grateful words are for my supervisors: Professor Ian Jones, Professor Roy Johnston, and Professor Jon Preece who professionally and sympathetically help and support me.

Prof. Jon Preece's Nanoscale Chemistry Group is a comfortable working environment for me, with youthful and friendly members (Scott, Paul, Vivek, Rachel, Katie, Rujikan, and others). Prof. Jon, with his scientific robustness, sensitiveness and sense of humour, always makes my research work more enjoyable. I also would like to thank Dr. Coen van den Brom and Dr. Jill Newton for their nice help and collaboration with me in the chemical synthesis work.

I have learnt useful knowledge from the members (Oliver, Andy, Sara, Paul, Ramli, and others) of Prof. Roy Johnston's Computational Chemistry Group. My theoretical work progress is nurtured by Prof. Roy's invaluable guidance, care, and kindness. I also would like to thank Dr. Oliver Paz-Borbón for his helpful tutorials in performing computational programs.

Prof. Ian Jones's Electron Microscopy Group is my home group. Prof. Ian is my patron, both scientifically and humanly. I would like to say that I can not accomplish my study without his role. He provides me with professional guidance, raises me up from my depression, connects me with nice people, and spiritually makes me feel happy and safe. In Ian's Group, I also have nice friends (Anqui, Ding, Ming, Gael, Hiroto, Jishen, Ruilin, Sattar, Winson, Xiaoning, Xin Xin, Yau Yau, Yu Lung, and others) who bring me warm help and friendliness. I also would like to say thanks to Dr. Ming Chu for her TEM tutorials, and Dr. Yu Lung Chiu and Dr. Ding Rengen for their support.

I would like to thank Prof. Lynne Macaskie and Dr. Kevin Deplanche (Biosciences, University of Birmingham) who provided me with their microbially synthesized Pd-Au nanoparticles. I acknowledge Dr. Quentin Ramasse's help in operating the Super STEM at Daresbury Laboratory.

The funding for my study is offered by the School of Metallurgy and Materials and the Overseas Research Students Awards Scheme (ORSAS). I'm highly grateful to these sponsors who allow me to pursue the PhD program.

Finally, the great spiritual mainstay for me is the constant support and care by my parents and my sister who always look forward to my mature and success. I also would like to mention the support and encouragement by my Vietnamese friends (Mai-Anh Tran, Duc-The Ngo, Van-Son Dang and Nga-My Nguyen).

This thesis and the work described in it are entirely my own, except where I have acknowledged *either* help from a named person *or* a reference given to a published source or a thesis. Text taken from another source will be enclosed in quotation marks and a reference will be given.

September 30, 2010

# CONTENTS

# LIST OF FIGURES

# LIST OF TABLES

# CHAPTER 1. INTRODUCTION

## 1.1. A brief history of nanoparticles

*Things originated from the passion for beauty*

Gold entered the human world in ancient times because of its beauty. Furthermore, gold-containing nanoparticles appeared in Roman era as an elaborate decorating material. The beautiful "Lycurgus Cup" (currently owned by the British Museum), which is red in transmission and green in reflection, contains silver-gold bimetallic nanoparticles of around 50-100 nm in diameter [1].

Until the seventeenth century, the synthesis of gold colloids to colour glass was described by some Italian glass makers. Two centuries later, in 1857, Michael Faraday carried out his first remarkable experiments on metal colloids and described various colours of gold particles using different preparations [2]. In his report, Faraday wrote: "gold is reduced to exceedingly fine particles which becoming diffused, produce a beautiful fluid…the various preparations of gold whether ruby, green, violet, or blue…". It was the first time the optical properties of gold nanoparticles from different preparations had been observed and described scientifically. Nowadays, it is well-known that the various colours of liquid-dispersed gold nanoparticles having different sizes represent a so-called *size effect* – a basic fact concerning nano-scale objects. That is, the properties of nanoparticles may change when their size changes.

For more than half a century after Faraday's experiment, there were only few scattered works relevant to nanoparticles. Albert Einstein, in his study of Brownian motion for nanoparticles, described their diffusion coefficient [3]. Among the most important of these

early studies was Gustav Mie's theory of the optical properties of nano-scale spherical particles [4], which is still used widely nowadays.

An important achievement in this period was Richard Zsigmondy's work. Zsigmondy discovered the seeding method which allowed him to prepare gold nanoparticles dispersed in dilute solutions [5]. Zsigmondy also developed the "ultra-microscope", an apparatus using light scattering to visualize nanoparticles which typically have diameters below or near the wavelength of visible light. These particles were around a few hundred nanometres in diameter [6]. They are usually called colloids and they are quite large compared to today's typical nanoparticles.

Zsigmondy was awarded the 1925 Chemistry Nobel Prize for his works. Some scientists felt that the interest of these tiny objects may not only be their beautiful colours (e.g., of colloidal gold) but also other novel properties. In 1914, Wolfgang Ostwald published a book called: "The World of the Neglected Dimensions" [7] - the resume of many lectures which this German chemist had given to attract the attention of the scientific community to colloidal chemistry. It was predicted by Frölich and Kubo that the electronic properties of colloidal metals might be different from those of bulk metals [8].

The huge rise of interest in nanoparticles only began a few decades ago, along with the development of modern instruments and the increasing power of computers. Since the first construction of the Transmission Electron Microscope (TEM) by Max Knoll and Ernst Ruska in 1931, it has become feasible to observe particles much smaller than the wavelength of visible light. The continuous development for nearly a century has raised the capacity of this instrument, making it become one of the most powerful and reliable techniques for studying nanoparticles, approaching the atomic scale for these tiny materials. Besides electron microscopes, the invention of the Scanning Tunnelling Microscope (STM) and

Atomic Force Microscope (AFM) in the 1980s, along with advances in microelectronics has given us the ability to manipulate, explore and study the physical characteristics of nano-scale structures, including nanoparticles. Concerning theory, while the quantum mechanical problems of a system consisting of many interacting atoms were too heavy in the first half of the 20$^{th}$ century, clusters of a few tens of atoms, in recent decades, can be modelled and calculated using supercomputers with codes based on modern methodologies such as Molecular Dynamics (MD), Monte-Carlo (MC), Genetic Algorithms (GA), and Density Functional Theory (DFT) [9].

As well as characterization techniques, methods for preparing nanoparticles have also been developing continuously for more than half a century. In recent decades, various approaches to make nanoparticles, including chemical, physical, physicochemical and biological, have become available. Chemical methods have the longest history and still are among the most common. In the early stage of nanoparticle technology, one of the first remarkable achievements was credited to Turkevich (1951) [10] and Frens (1973) [11] who established a simple and effective method for the synthesis of 10-20 nm gold nanoparticles dispersed in water. These particles are stabilized, because they have negatively-charged citrate ions attached to their surfaces, providing Coulomb repulsions between the particles, preventing their aggregating. After Turkevich and Frens, stabilized nanoparticles have been the subject of great interest. Various attempts have been made, using ionic surfaces or surfactant molecules to prevent particles from aggregating. For example, Brust and Schiffrin (1994) developed a method for preparing gold nanoparticles in a two phase liquid-liquid system, using thiol molecules as the surfactants [12].

Chemically stabilized nanoparticles have facilitated further steps for making bimetallic nanoparticles. For instance, citrate-stabilized gold nanoparticles can be coated with platinum

or palladium to form core-shell structures [13]. Galvanic exchange reactions can be used to make gold-silver, gold-palladium, and gold-copper bimetallic nanoparticles from alkanethiol-stabilized monometallic ones [14].

Modern metallurgy, in the age of nanotechnology, is not only "bulk alloys in furnaces" but also heterogeneous systems of nano-scale materials, including bimetallic nanoparticles synthesized in chemical flasks. At the current stage of nanotechnology, there is great interest in bimetallic nanoparticles, with important developments in three main areas: modelling, synthesis, and characterization [8,9,15].

## 1.2. Basic features of nanoparticles

### 1.2.1. Definition of nanoparticles and surface effects

The definition of nanoparticles depends on the context. That is, the definition may be slightly different for different fields, different materials, or different applications. From a theoretical viewpoint, nanoparticles are frequently called *nanoclusters* or simply *clusters* which are defined as aggregates of between a few and millions of atoms or molecules [9, 16, 17]. These atoms or molecules may be of the same or different types [6, 7]. For example, an aggregate will be called a pure metal nanocluster if it is built from one type of metal atom, or a metallic alloy nanocluster if it consists of more than one type of metal atom. *Bimetallic nanoclusters* consist of two different metals.

When the dimensions of a particle decrease, its surface-area/volume ratio drastically increases. When this ratio is large, the low-coordinate atoms on the particle surface predominate, and mainly govern the particle properties. This may lead to what called *surface effects* if the size of the particle becomes small enough. Surface effects make the properties of nanoparticles different from those of the corresponding bulk materials. A simple and basic

surface effect is the dramatic rise in chemical reaction rates, due to the increase in contact area. For catalytic applications which are simply based on the large area of contact, roughly, the particles which have diameters from around 100 nm to 1 μm can be called as nanoparticles [18] (they are traditionally called as colloids when suspended in liquids). Nanoparticles with diameters from around one to a few tens nanometres are the most common in current research.

### 1.2.2. Size effects

It has often been observed that in the nanometre size range, some specific properties, such as melting point and dielectric constant of nanoparticles depend on their sizes. As mentioned previously, this is called a *size effect*: for example, the gold particles from different preparations by Faraday are different in size, so they exhibit different colours. This varying optical property of nanoparticles is attributed to the characteristic of collective electron-density oscillations called *plasmon excitations*. Nanoparticles which differ in size have distinct plasmon resonances, resulting in different energy absorption spectra, including optical absorption spectra. For instance, the light absorption peaks at wavelength values of 517, 521, 533, and 575 nm for 9, 22, 48, and 99 nm-sized gold nanoparticles in water, respectively (see Figure 1.1) [19].

Naturally related to optical properties, the electromagnetic properties of nanoparticles also show size effects. It is known that dielectric constants of PbTiO3 nanoparticles increase significantly when their sizes are smaller than around 20 nm, and the magnetization characteristics for magnetic nanoparticles may change remarkably with size [18]. A famous result from the size-dependent change in physical and chemical properties of nanoparticles is

that gold, a noble metal, is inert in the bulk form, but exhibits novel catalytic behaviour as nanoparticles [20].

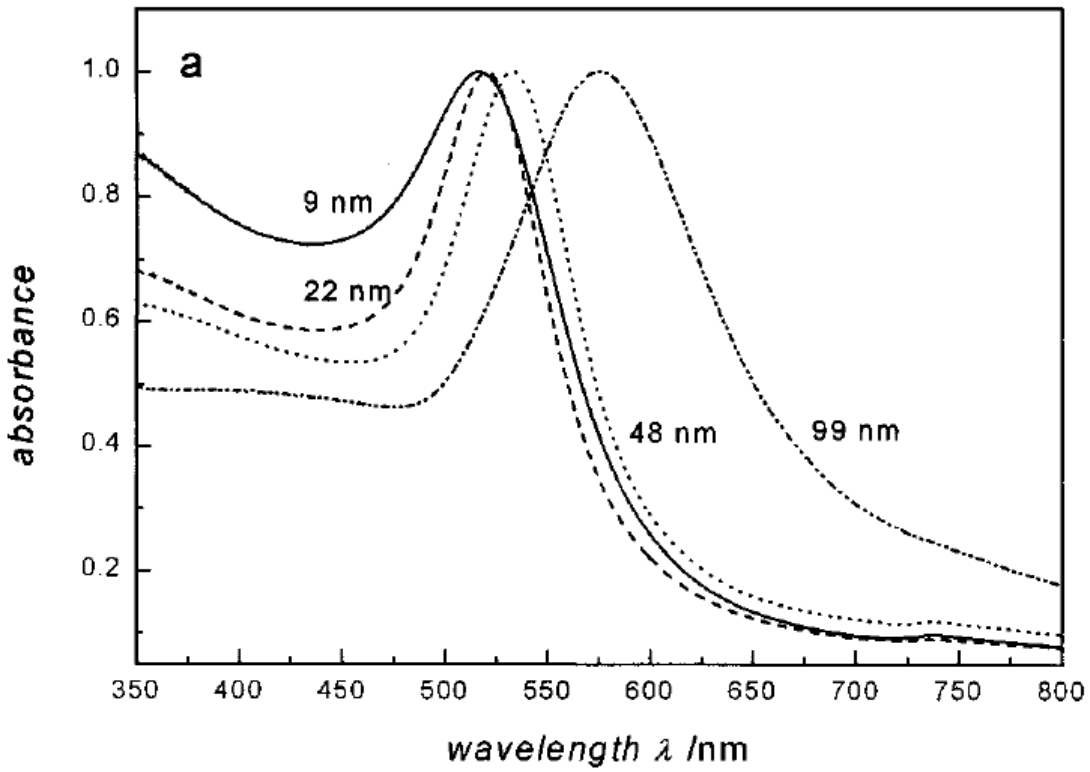


**Figure 1.1.** Optical absorption spectra (in the ultraviolet and visible ranges) of 9, 22, 48, and 99 nm-sized gold nanoparticles [19].

Another example of a size effect is the increase in melting temperature of gold nanoparticle with increasing size. Figure 1.2 shows the theoretical and experimental melting temperatures of gold nanoparticles as a function of their size [21], approaching the bulk value for the melting temperature of gold when the size increases up to a few tens of nanometres.

While bulk gold has a face-centered-cubic (FCC) structure, gold nanoparticles may be amorphous for certain sizes, or they may have various morphologies, including decahedra, truncated-octahedra, or icosahedra for different sizes [22]. Furthermore, some

crystallographic properties, such as lattice parameter, are believed to be size and shape dependent [23]. As a result of the changes in structure, size-dependent changes in mechanical properties of nanoparticles have also been reported [24].

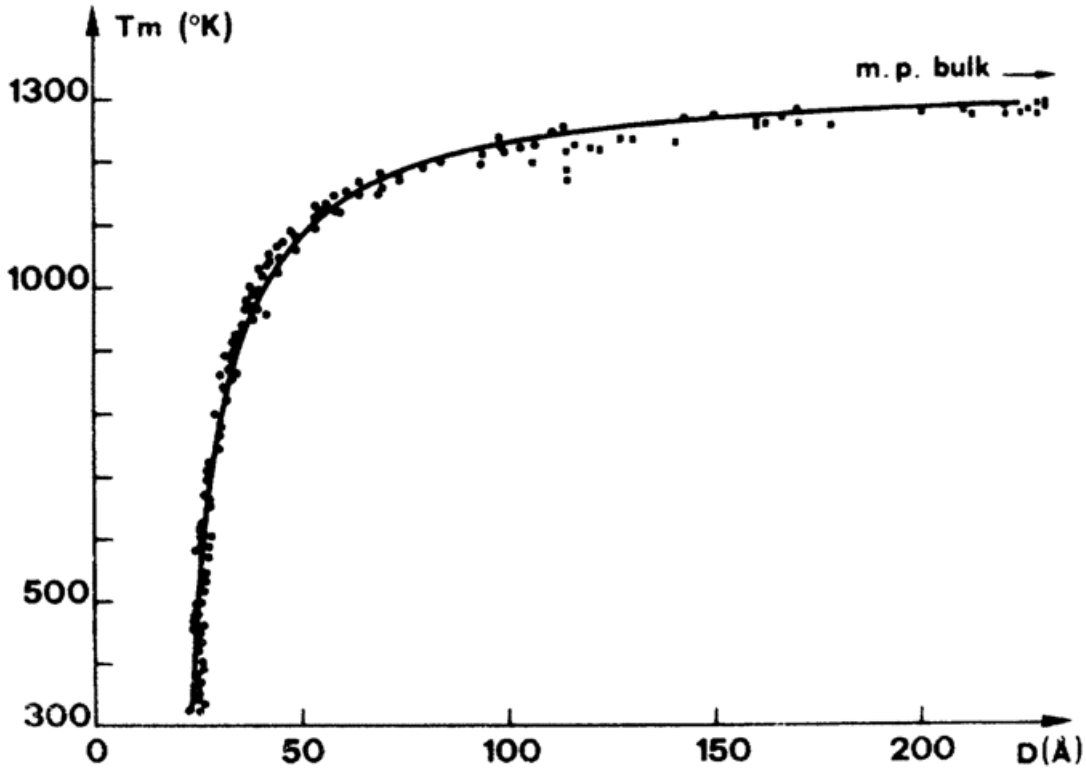


**Figure 1.2.** Experimental and theoretical values for melting-point of gold nanoparticles (circles and squares); the solid line results from a least-squares fit using the experimental data [21].

When the particle size is smaller than the electron mean free path, the electron scattering from the particle surface become considerable. This kind of scattering makes a significant contribution to modify the electronic structure of the particles. In other words, there is a confinement for electrons in the particles, which induces *quantum-size effects*. These effects in metallic nanoparticles have been studied for several decades [25]. For instance, in an experimental study of monometallic Pd nanoparticles, which were around 15 nm in size, quantum-size behaviour of the specific heat has been clearly observed [26].

At the nanoscale, because the translational symmetry is not imposed, the structure of nanoparticles can be different from the bulk structure of the same materials. This results in a complicated competition in energetic stability of various structural motifs. In addition, since the electronic structure depends on the local arrangement of atoms, as it will be discussed later, some physical-chemical properties of nanoparticles can be varied by changing their size and chemical composition. Thus, it is important to characterize both experimentally and theoretically the structure of nanoparticles.

## 1.2.3. Magic geometric numbers and magic electron numbers

### 1.2.3a. Magic geometric numbers

The tendency to minimize surface-to-volume ratio is one of the reasons causing atoms in metal clusters to be packed, usually making high-symmetry cluster structures. There are many classes of high-symmetry structures. Each symmetry class is constructed from specific shells of atoms which are also called *geometric shells*. When a number of atoms can be packed to complete the geometric shells of a high-symmetry structure, it is said to be *magic geometric number* [27]. For example, icosahedral structures ($I_h$ symmetry) are constructed from one central atom surrounded by geometric shells consisting of 12, 42, 92, 162, etc. atoms. Thus the respective magic atom numbers are 1 + 12 = 13, 13 + 42 = 55, 55 + 92 = 147, 147 + 162 = 309, etc.

As another example, for structures of octahedral symmetry ($O_h$), which has face-centred-cubic (FCC) packing, there are two ways to complete the geometric shells. The first way is the formation of the cuboctahedral geometry having the same magic atom numbers of the icosahedra: 13, 55, 147, 309, etc. In the other way, a basic octahedron is built from 6 atoms, and the larger clusters are constructed by surrounding that central octahedron with the

subsequent shells of 38, 102, 198, etc. atoms, resulting in octahedral clusters with the respective magic atom numbers are 6, 44, 146, 344, etc. By removing the corner atoms from the octahedral, truncated-octahedral species can be obtained. The truncated-octahedral species can be either cuboctahedral geometry which has triangular (111) facets or the plain called truncated-octahedral geometry which has hexagonal (111) facets. The magic atom numbers for the truncated octahedral geometry are: 38, 116, 260, etc.

Figure 1.3 shows images of some high-symmetry clusters having the geometric shells completed with the magic numbers: 147-atom icosahedron, 147-atom cuboctahedron, 116-atom truncated octahedron, 146-atom octahedron, 153-atom hexagonal close packing, 105-atom decahedron, 147-atom truncated decahedron, 146-atom Marks-truncated decahedron.

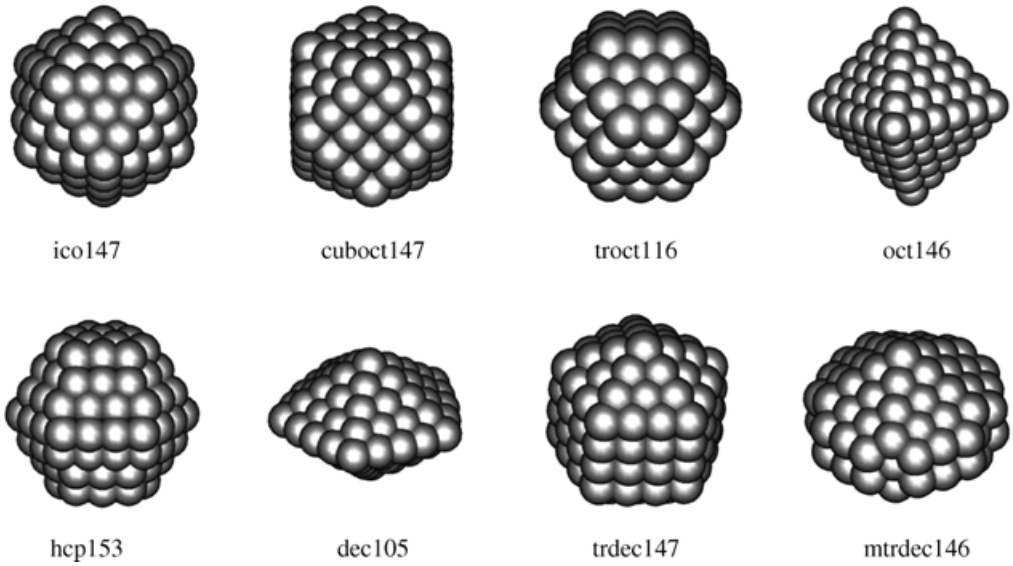


**Figure 1.3.** Some high-symmetry clusters having the geometric shells completed with the magic numbers [27]: 147-atom icosahedron (ico147), 147-atom cuboctahedron (cuboct147), 116-atom truncated octahedron (troct116), 146-atom octahedron (oct146), 153-atom hexagonal close packing (hcp153), 105-atom decahedron (dec105), 147-atom truncated decahedron (trdec147), 146-atom Marks-truncated decahedron (mtrdec146).

### 1.2.3b. Magic electron numbers

According to quantum mechanics, electrons within clusters occupy different energy levels. These energy levels form *electronic shells* in clusters. The electronic distribution for a cluster can be approximately described by the *jellium model* [28], in which a spherical charge distribution is assumed and the positive charges of the nuclei are considered as a uniform positively charged background. In the jellium model, each electron is in a potential field which resembles that of an isotropic harmonic oscillator, allowing the analytic solution for the single-electron Schrödinger equation. The electronic shells are determined as the energetic sequence of eigenfunctions (solutions of the single-electron Schrödinger equation): (1s), (1p), (1d, 2s), (1f, 2p), (1g, 2d, 3s), etc. The Pauli exclusion principle governs the occupations of orbital electrons, yielding the *magic electron numbers* [27]: 2, 8, 20, 40, 70, etc., for the completion of the respective shells. Figure 2.3 shows the jellium electronic shells and the corresponding magic electron numbers corresponding to the Schrödinger equations for one electron with spherical symmetry, interacting electrons with spherical symmetry, and interacting electrons with octahedral symmetry.

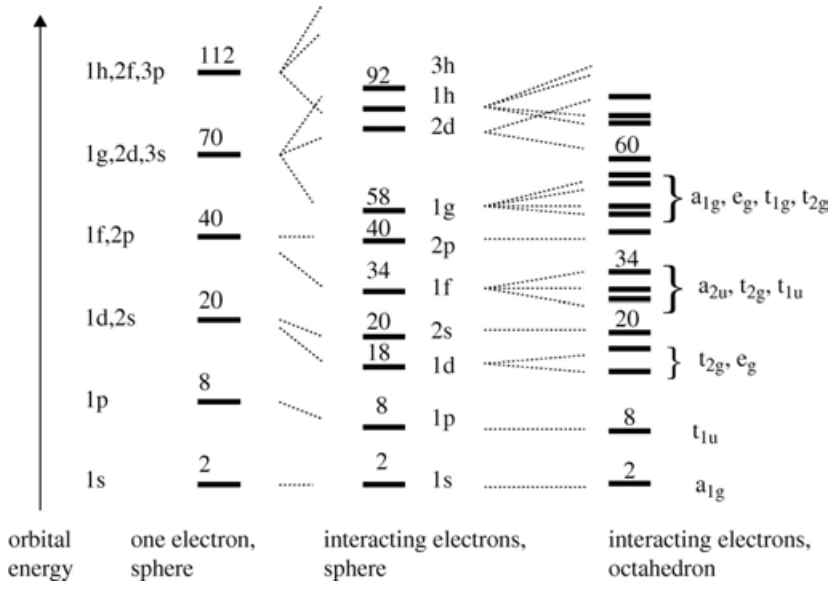


**Figure 1.4.** Diagram of energy levels in the jellium model [27].

### 1.2.4. Bimetallic nanoparticles

From monometallic to bimetallic nanoparticles, an extra degree of freedom (the composition) is introduced. In an analogous fashion to traditional bulk metallurgy, some properties of bimetallic nanoparticles can be modified by changing their compositions. However, the phenomena which one expects here are not simply related to what happens when the two coressponding metallic elements are mixed to form a bulk alloy. That is, the metallurgy for a certain bimetallic system at the bulk scale and at the nano-scale may be somewhat different from each other. In the bulk, Au can be mixed with Pt to form a continuous solid solution at high temperature (although these two species are immiscible at low temperatures) [29], whereas bimetallic Au-Pt nanoparticles of around 20 nm in size exhibit a layer segregation between Au and Pt when annealed at 600$^{o}$C [30]. The interaction between the two metals plays an important role in the properties of bimetallic nanoparticles. These characteristics are quite sensitive to the medium in which the particles are studied. This is because the elemental arrangements of bimetallic nanoparticles depend strongly on which method is used to produce them [9], and the system of the two metals is generally not in thermodynamic equilibrium. Moreover, surface passivating ligands, which are normally employed to prevent particle aggregation, may also affect the relation between the metallic components [9]. These circumstances make the mixing and segregation tendencies, as well as the elemental arrangements of bimetallic nanoparticles more diverse and complicated than in the cases of bulk alloys (see Figure 1.3 for some possible patterns). Away from random mixings and simple phase separations which are familiar to bulk alloys, one of the most interesting kinds of element arrangement for bimetallic nanoparticles is the *core-shell* structure, in which the two metallic phases segregate from each other, one mainly occupies the interior, and the

other covers the outer part of the particle (Figures 1.3a and 1.3d). Core-shell nanoparticles attract much interest because of their potential for catalytic applications.

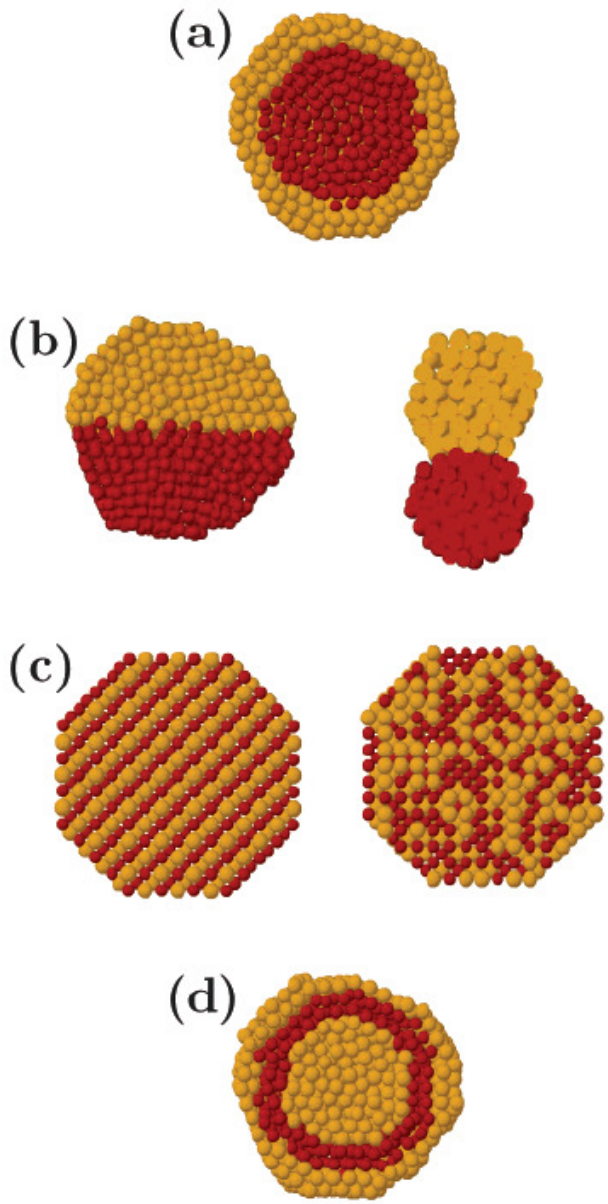


**Figure 1.5.** Cross section schematic representation of some possible patterns for different element arrangements of bimetallic nanoparticles: core-shell **(a)**; sub-cluster segregated or simple phase separated **(b)**; ordered and random mixed **(c)**; three-shell onion-like **(d)** [9].

## 1.3. Applications of nanoparticles.

Their use as decorating materials was the reason for nanoparticles to be made in ancient times (see 1.1). But nowadays, nanoparticles can find applications in various technological fields, ranging from catalysis to medicine and electronics.

### 1.3.1. Catalysis

Metallic and bimetallic nanoparticles, especially those containing a few tens or a few hundreds of atoms, are excellent catalysts because of their highly active surfaces. These catalytic nanoparticles have improved selectivity, efficiency, and recyclability, achieving the modern requirement for *green catalysts*. Tailoring catalytic properties can be focused on the size, shape, and homogeneity of nanoparticles which frequently influence catalytic processes [31].

There is a wide range of reactions which can be catalyzed by various nanoparticles. Among the most popular are the catalysts for hydrogenation and oxidation reactions [31]. For example, Au nanoparticles have been known for their capability in selective oxidation of CO [32-35]. Selective hydrogenation can be catalyzed by many transition metal nanoparticles, including Pd and Pt particles [36, 37]. The development of proton exchange membrane (PEM) fuel cells is closely integrated with the desire to have better systems of catalytic particles to reduce CO poisoning at the anode and increase efficiency [31, 38]. Catalytic Pt-based nanoparticles supported on carbon nanotube are the most common material for electrodes in PEM fuel cells. Improvements can be achieved thanks to the understanding of size, shape, chemical composition, and chemical ordering of these particles [39-42].

Going from monometallic to bimetallic nanoparticles, catalytic behaviour is often observed to be better, probably because of "synergistic effects" [9, 13]. Core-shell bimetallic particles are among the most studied nano-catalysts, due to potential improved catalytic activity and also in order to reduce manufacturing costs. For example, because Pt – a good catalyst for fuel cells is a very expensive material, studies of Pt-coated particles, which optimize the catalytic properties and make the application more economic, are of interest.

### 1.3.2. Biodiagnostics

For more than 10 years, nanoparticles and other nanostructures have been used in biodiagnostics (or molecular diagnostics), a field which belongs to biomedicine. Nanoparticles have been known to be robust, sensitive, and selective when used as cellular labels and DNA/protein markers for diagnosing disease [43, 44]. For example, citrate-stabilized Au nanoparticles can be used to detect sequences in PCR (polymerase chain reaction)-amplified genomic DNA [45]. Surface plasmon resonance (SPR) spectroscopy of Au-containing nanoparticles is used to probe real-time DNA hybridization on surfaces with high sensitivity [46]. Various colours (due to various SPR) of $Ag_{core}Au_{shell}$ nanoparticles having different sizes (50-100 nm in diameter) and different compositions are exploited as tunable probes for DNA detection [44]. In affinity biosensors, gold nanoparticles can be used as the inert substrates to immobilize the receptor molecules which have affinity for analyte molecules such as DNA and proteins [18].

### 1.3.3. Nanoelectronics

Unique electric and magnetic properties of nanoparticles can be exploited to create novel electronic devices.

It has been found that the capacitance of Au nanoparticles increases by approximately eightfold when a single redox reaction takes place at their surfaces [47]. In another experiment, a prototype of a nano-switch was built using a layer of Au nanoparticles, in which the conductivity of the system could be altered by electrochemically altering the redox state [48]. Switching behaviour, manifested in terms of varying resistance, has been observed for two Pd nanoparticles linked by a conjugated thiol molecule [49]. Some kinds of nanoparticles may be regarded as quantum dots which can be the basis of single electron transistor (SET) – a conceptual device for future computers [50].

Ideas concerning the use of magnetic nanoparticles as recording materials have been proposed. For instance, the sustained high-density magnetization transition found for ferromagnetic systems of Fe-Pt nanoparticles can be exploited in recording applications [51]. A composite of polystyrene and 2-naphtolenethiol-capped Au nanoparticles has been found to exhibit electrical transitions when induced by strong electrical fields, suggesting a potential application in memory devices [52]. Composites of Au nanoparticles and polyaniline nanofibers have also been observed to exhibit memory effects [53].

# CHAPTER 2. GENERAL METHODOLOGIES

**Abstract.** Methodologies for the three aspects of nanoparticle study: theory (modelling); chemical and biological synthesis; and electron-microscope characterization are described in this chapter. In the theoretical part, empirical potential (EP) genetic algorithm (GA) and density functional theory (DFT) approaches to study the structure, energetic stability, chemical ordering, and electronic property of clusters are described. In the synthesis part, methods for producing nanoparticles in wet-chemical and microbial media are described. The tools for observation and investigation of the chemically/microbially synthesized nanoparticles, which are described in the characterization part, are Transmission Electron Microscopy (TEM), Scanning TEM (STEM), and STEM-based techniques: High Angle Annular Dark Field (HAADF) imaging, Energy Dispersive X-ray (EDX) analysis, and Electron Energy Loss Spectroscopy (EELS).

## 2.1. Modelling

### 2.2.1. Overview of theoretical methodologies for cluster studies

Theoretical study of cluster structures relates to practical applications of nanoparticles. It is obvious that only sufficiently stable structures can be used for technological applications. Moreover, the structure influences a particle's properties, including surface characteristics in catalytic applications. For example, selectivity in catalysis can be tuned by controlling particle shape [54].

G*lobal optimisation* of geometry is one of the central problems of cluster studies. A cluster at a given finite temperature, with a given size and composition, can have different

structural states (isomers), that is, meta-stable states and the most stable state (thermodynamic equilibrium structure) which can be described as local minima (LM) and the global minimum (GM), respectively, on the potential energy hypersurface [55]. This hypersurface has 3N +1 dimensions, where N is the number of atoms (cluster size), 3N is the number of degrees of freedom, and the extra dimension is the potential energy. Solving a global optimisation problem means finding the GM – the structural state having the lowest potential energy, as well as low-lying LM, which are the best candidates expected to be observed in experiment together with the GM.

Generally, there are two kinds of approaches to global optimisation problems: *ab initio* and *non-ab initio*. Recently, the combination of these two approaches has been developed. The ab initio approach is the performance of calculations at the accuracy of quantum mechanics, applying many-body quantum theories such as Density Functional Theory (DFT). Despite their high accuracy, ab initio calculations for large clusters (consisting of hundred of atoms or more) are computationally expensive [56], even considering current development of computers. The non-ab initio approach (i.e., the empirical approach) involves the use of empirical atomistic potentials which have parameters fitted to experimental data.

There are two different models of atomistic potentials which are often used in cluster studies: pair-wise potentials and many-body potentials. Pair-wise potentials, such as the Morse potential and the Lennard-Jones potential, are approximations where the interactions only depend on the distances between pairs of atoms. Many-body potentials, such as the Gupta and Sutton-Chen potentials, take into account the many-body nature of interatomic interactions inside clusters [57-59].

The major simulation algorithms used for cluster studies are Molecular Dynamics (MD) Simulated Annealing (SA), Monte Carlo (MC), Monte Carlo with Basin Hopping (BH) [57], and Genetic Algorithms (GA). The effectiveness of these algorithms in solving global optimisation problems depends on how sophisticated the search routines are, which potential models are used, and cluster size. For example, for finding GM for the short range Morse potential, a GA developed at the University of Birmingham [56] has been shown to be more effective than traditional MC and MD-SA approaches [58].

Global optimisation becomes more difficult as the cluster size increases, because the number of dimensions of potential energy hypersurface (3N +1) increases, resulting in an exponential increase in the number of minima with cluster size [59].

The problem of ***homotops*** is another difficulty which has been described in studies of bimetallic clusters [16, 60]. Homotops (in binary systems) are $A_aB_b$ isomers having a fixed number of atoms ($N = a + b$), the same composition ($a/b$ ratio) and the same geometrical structure, but different arrangements of the A and B type atoms. Homotops can be interconverted by permuting atoms of different types in the bimetallic cluster. The number of homotops $H(A_aB_b)$ increases enormously with cluster size $(a + b)$ and also depends on the composition (the numbers of A atoms $a$ and B atoms $b$), as in the following formula:

$$H(A_aB_b) = \frac{(a+b)!}{a!b!} \quad . \tag{2.1}$$

For example, $H(Cu_{10}Au_{10}) = 184756$, $H(Cu_{19}Au_{19}) \approx 3.53\times10^{10}$, and $H(Cu_{20}Au_{20}) = 1.38\times10^{11}$. Although some homotops having high symmetries may be symmetry-equivalent, the huge numbers of homotops in larger bimetallic clusters make the global optimisation very difficult.

In this thesis, the theoretical study of gold-containing bimetallic clusters is performed using a combination of empirical and ab initio approaches. For the empirical level, the Birmingham Cluster Genetic Algorithm (BCGA) is used for global optimization on the empirical Gupta many-body potential energy hypersurface. At the ab initio level, geometrical reoptimisation and calculation of electronic properties are performed using DFT.

### 2.1.2. The Birmingham Cluster Genetic Algorithm

The Genetic Algorithm (GA) is an optimizing technique based on principles similar to those of natural selection, which were initiated by John Holland during 1960s and 1970s [61]. Since then GAs have been utilized successfully in solving optimisation problems in many scientific fields [62,63]. The application of GAs for geometrical optimisations of nanoclusters has been performed since the 1990s [64]. Basically, this approach is a simulation of natural evolution to single out the most "adaptive" clusters, which have the lowest energies.

In this work, the *Birmingham Cluster Genetic Algorithm* (BCGA) [56] is used to search for the GM (lowest energy) and other low energy LM (metastable isomers) of Cu-Au, Pd-Au, and Pt-Au clusters modelled by the empirical Gupta many-body potential. In the BCGA, the probability of a cluster taking part in genetic crossover and surviving into successive generations depends on its fitness, with high fitness structures corresponding to isomers with low potential energy. Figure 2.1 shows a schematic flow chart for the BCGA. Details of the routines and operators are described below [56]:

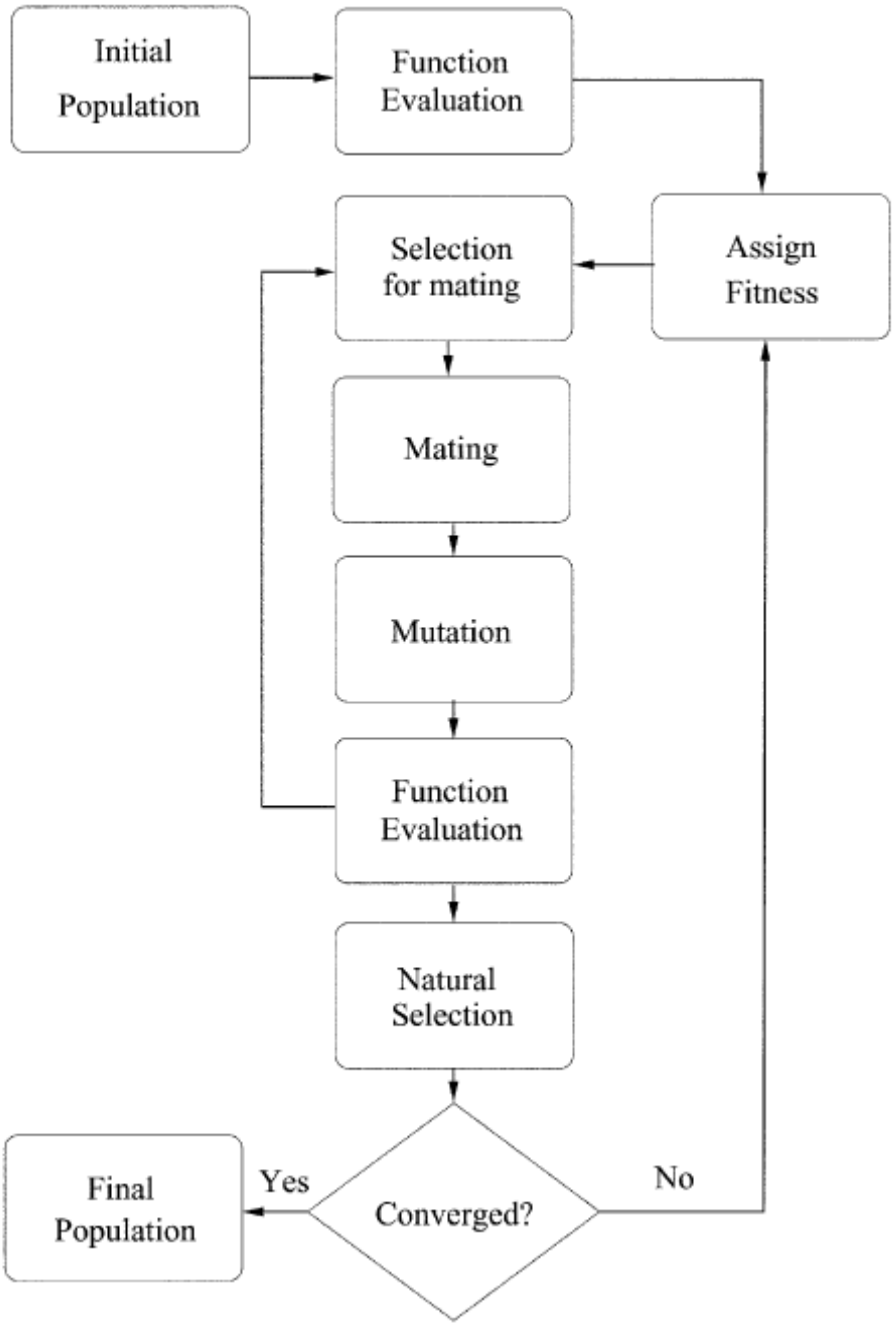


**Figure 2.1.** Flow chart of routines in the Birmingham Cluster Genetic Algorithm [56].

For a given cluster size, the *initial population*, or the zeroth generation $G_0$ consists of a number of clusters which are generated randomly. Each of the clusters is considered as an individual with its "genetic code" being the real-valued Cartesian coordinates of the cluster atoms (the Zeiri approach [65]). The cluster potential energy, which is a function of these

coordinates, is then minimized using the quasi-Newton routine [66], relaxing the clusters into the nearest LM.

*Fitness* is a scaling quantity which measures the relative stability of the clusters in a population. The highest fitness and the lowest fitness are attributed to the lowest-energy cluster and the highest-energy cluster, respectively. In the BCGA, an energy-normalized factor $\rho$ is introduced in the fitness calculations:

$$\rho_i = \frac{V_i - V_{\min}}{V_{\max} - V_{\min}} \quad , \tag{2.2}$$

where $V_i$ is the energy of the $i^{th}$ cluster, $V_{min}$ and $V_{max,}$ are the lowest and the highest cluster energies, respectively, of the current population. In this work, a hyperbolic tangent form is selected for the fitness function:

$$f_i = \frac{1}{2}[1 - \tanh(2\rho_i - 1)] \quad . \tag{2.3}$$

*Parents for crossover* are selected using either *roulette wheel* or *tournament selection*, which are based on the principle that the probability for an individual to be selected is proportional to its fitness. In the roulette wheel method, if a randomly chosen individual has a fitness greater than a random value generated between 0 and 1, it will be selected for crossover. In the tournament selection method, a number of individuals are picked at random to undergo a fitness competition; the two individuals of highest fitness are then selected as parents.

*Crossover* is performed using a variant of the cut-and-splice method developed by Deaven and Ho [67]. In our work (presented in this thesis), the *single-cut* method is adopted,

in which a random cutting plane is introduced. This cutting plane can be either placed to pass through the middles of the clusters, or weighted with respect to the relative fitnesses of the two parents (*one-point-weighted*): the fitter parent contributes more atoms. When a predetermined number of offspring ($N_{off}$) is reached, the crossover process will stop.

*Mutation* is needed to prevent stagnation and to enhance population diversity. In the BCGA, each individual has a probability of being mutated. A mutation operator is introduced to perturb the atoms of the clusters. There are several kinds of mutation operators adopted in the BCGA:

(a) *Atom displacement:* a mutation operator replacing the coordinates of a certain number of atoms with new coordinates randomly generated in the range $[0, N^{1/3}]$.

(b) *Twisting:* a mutation operator causing a z-axis rotation, by a random angle, of the upper half with respects to the bottom half of the cluster.

(c) *Cluster replacement:* this mutation operator swaps a whole cluster for a new cluster which is randomly generated in the same way with the one used to generate the initial population.

*(d)* *Atom permutation*: a mutation operator interconverting homotops of bimetallic clusters by exchanging the coordinates of atoms of different types without altering the cluster structure.

The whole process of fitness evaluation, crossover, mutation, and selection are repeated for each generation $G_i$. The subsequent generation $G_{i+1}$ is formed by selecting the highest fitness (lowest energy) clusters from the previous generation $G_i$, the new offspring clusters, and the mutated clusters. If there is no change in the range of cluster energies (from the lowest $V_{min}$ to the highest $V_{max}$) for a preset number of generations (typically 10), the population is considered to be converged.

In our work, we perform BCGA searches for $Cu_nAu_{38-n}$ (Chapter 3), $Pd_nAu_{54-n}$ (Chapter 5), and $Pt_nAu_{40-n}$ clusters. We adopt the following inputs for the program: the population size is 40 clusters; the number of offspring clusters $N_{off}$ is equal to 32; the selection of parents for crossover is based on the roulette wheel method; the chosen crossover (mating) type is one-point weighted; a mutation is set up to operate with probability 0.2, this is the probability of mutating each offspring cluster; the type of mutation consists of randomly moving approximately 1/3 of the cluster atoms to new random positions; the cluster population is evolved until a convergence criterion is satisfied. In this work, the convergence criterion is that the BCGA run will terminate if the population remains unchanged over 10 generations, otherwise the run will terminate after a total of 500 generations; for each composition, 100 GA runs are performed.

### 2.1.3. Gupta potential

The empirical Gupta many-body potential is based on the tight-binding second-moment approximation [68, 69]. The Gupta potential includes repulsive and attractive terms:

$$V_{clus} = \sum_{i}^{N} \left\{ V^r(i) - V^m(i) \right\}, \tag{2.4}$$

in which the repulsive pair terms $V^r(i)$ and the attractive many-body terms $V^m(i)$ are defined as:

$$V^r(i) = \sum_{j}^{N} (1-\delta_{ij}) A(a,b) \exp\left( -p(a,b) \left( \frac{r_{ij}}{r_0(a,b)} - 1 \right) \right), \tag{2.5}$$

$$V^m(i) = \left[ \sum_{j}^{N} (1-\delta_{ij}) \zeta^2(a,b) \exp\left( -2q(a,b) \left( \frac{r_{ij}}{r_0(a,b)} - 1 \right) \right) \right]^{1/2}, \tag{2.6}$$

where *a* and *b* indicate the element types; $\delta_{ij}$ = 1 if $i = j$, or 0 if $i \neq j$. The parameters *A, $r_0$, $\zeta$, p* and *q* are obtained by fitting equations (2.5) and (2.6) to experimental values of cohesive energy, lattice parameters and independent elastic constants for the corresponding bulk pure metals at 0 K.

## 2.1.4. Energetic analysis

The *excess energy*, which indicates the stability combined with the mixing tendency of bimetallic clusters, is defined as follows [70]:

$$E_{exc}(A_{N-n}B_n) = E(A_{N-n}B_n) - (N-n)\frac{E(A_N)}{N} - n\frac{E(B_N)}{N} \quad , \tag{2.7}$$

where $E(A_{N-n}B_n)$, $E(A_N)$ and $E(B_N)$ are the potential energies of the N-atom bimetallic clusters $A_{N-n}B_n$ and the pure clusters $A_N$ and $B_N$, respectively. Negative excess energies correspond to nanoalloys which are stable with respect to the pure metal clusters.

The *second difference in energy* is a quantity indicating the stability of a cluster of a certain composition relative to neighbouring compositions, written as:

$$\Delta_2 E(A_{N-n}B_n) = E(A_{N-n+1}B_{n-1}) + E(A_{N-n-1}B_{n+1}) - 2E(A_{N-n}B_n) \quad . \tag{2.8}$$

Positive values of $\Delta_2 E$ correspond to relatively stable compositions.

## 2.1.5. Density functional theory

Density functional theory (DFT) is an approach to solve the many-body problem (i.e., system of many interacting electrons) of quantum mechanics. DFT has not only been a popular

theory of atoms and molecules [71-73] but is also known as an effective method for the calculations of energy, geometry-local optimisation, and electronic structure of small metallic clusters [27]. The fundamental formalism of DFT is described below.

The time-independent, non-relativistic Schrödinger equation for a system of $N_e$ interacting electrons, in the Born-Oppenheimer approximation can be written (in atomic units):

$$\hat{H}\Psi(\mathbf{r}_1,\mathbf{r}_2,...,\mathbf{r}_{N_e}) = E\Psi(\mathbf{r}_1,\mathbf{r}_2,...,\mathbf{r}_{N_e}) \quad , \tag{2.9}$$

where $\boldsymbol{r}_i$ is the coordinate of the $i^{th}$ electron.

The Hamiltonian operator is the sum of three terms, from left to right: kinetic energy operator, external potential operator, and electron-electron interactions:

$$\hat{H} = -\frac{1}{2}\sum_{i}^{N_e}\nabla_i^2 - \sum_{i}^{N_e}\sum_{\alpha}^{N}\frac{Z_\alpha}{|\mathbf{r}_i - \mathbf{R}_\alpha|} + \frac{1}{2}\sum_{j\neq i}^{N_e}\sum_{i}^{N_e}\frac{1}{|\mathbf{r}_i - \mathbf{r}_j|} \quad , \tag{2.10}$$

where $Z_\alpha$ is the charge of the $\alpha^{th}$ nucleus of the coordinate $\boldsymbol{R}_\alpha$. ($N$ is the number of atoms). In the Born-Oppenheimer approximation, because the masses of atomic nuclei are much heavier than the electron mass, the motion of nuclei is neglected so $\boldsymbol{R}_\alpha$ = *constant*, only the motion of electrons is considered.

The average total energy of the system which is a *functional* of the state represented by the wave function $\psi(\boldsymbol{r}_1, \boldsymbol{r}_2, ...\boldsymbol{r}_{Ne})$ is written as:

$$E[\psi] = \int \Psi^*(\mathbf{r}_1,\mathbf{r}_2,...,\mathbf{r}_{N_e})\hat{H}\Psi(\mathbf{r}_1,\mathbf{r}_2,...,\mathbf{r}_{N_e})d\mathbf{r}_1 d\mathbf{r}_2 ... d\mathbf{r}_{N_e} \equiv \left\langle \psi \middle| \hat{H} \middle| \psi \right\rangle \quad . \tag{2.11}$$

This energy satisfies the *variational theorem*:

$$E[\psi] \geq E_0 \quad , \tag{2.12}$$

where $E_0$ is the *ground state energy.*

The conventional way to calculate the energy of the $N_e$-electron system is solving the Schrödinger equation (2.9) to find the $3N_e$-dimension wave function $\psi(\mathbf{r}_1, \mathbf{r}_2, \ldots \mathbf{r}_{Ne})$.

However, solving such an equation analytically is generally unfeasible. The Thomas-Fermi model [74,75] was an early attempt to tackle the problem without needing to solve the Schrödinger equation. The Thomas-Fermi model which can be called the "pre-DFT" method is a statistical model approximating the distribution of electrons in an atom to calculate the kinetic energy as a function of electron density.

Approaches to calculate the energy spectrum of the $N_e$-electron system have been developed to form the modern DFT which is based on the two *Hohenberg-Kohn Theorems* [76]:

Theorem 1: *The external potential, and hence the total energy* (i. e., represented by the Hamiltonian in Equation 2.10)*, is a unique functional of the electron density (to within an additive constant).*

Theorem 2: *The ground state energy can be obtained via the variational theorem: the density that minimises the total energy is the exact ground state density.*

That is, any positive and definite trial electron density $\rho_t(\mathbf{r})$ satisfies the standardization condition:

$$\int_{volume} \rho_t(\mathbf{r}) d\mathbf{r} = N_e \quad . \tag{2.13}$$

The variational theorem applies for the total energy as a functional of the electron density:

$$E[\rho_t] \geq E_0 \quad . \tag{2.14}$$

The two Hohenberg-Kohn theorems lead to the following fundamental statement (the *principle of least action*) for DFT:

$$\delta \left| E[\rho] - \mu(\int \rho(\mathbf{r}) d\mathbf{r} - N_e) \right| = 0 \quad . \tag{2.15}$$

The minimum of the functional *E[ρ]* corresponds to the ground state energy and density. Here, the change in energy due to the change in the number of electron is described, with the *chemical potential* $\mu$ as the Lagrange multiplier.

From Equation 2.10 for the Hamiltonian, the energy functional can be written as the sum of three terms:

$$E[\rho] = T[\rho] + V_{ext}[\rho] + V_{ee}[\rho] \quad . \tag{2.16}$$

The external potential functional $V_{ext}[\rho]$ is represented as:

$$V_{ext}[\rho] = \int \hat{V}_{ext}\, \rho(\mathbf{r}) d\mathbf{r} \quad . \tag{2.17}$$

The kinetic *T[ρ]* and electron-electron interaction $V_{ee}[\rho]$ functional can only be approximated. In an approximation proposed by Kohn and Sham [77] a fictitious system of

$N_e$ non-interacting electrons is described as a set of $N_e$ single determinant wave functions (orbitals) $\Phi_i$.

This allows the kinetic energy for $N_e$ non-interacting electrons to be written exactly as:

$$T_n[\rho] = -\frac{1}{2}\sum_i^{N_e}\left\langle \phi_i \left| \nabla^2 \right| \phi_i \right\rangle \quad , \tag{2.18}$$

and the ground state density:

$$\rho(\mathbf{r}) = \sum_i^{N_e} \left|\phi_i\right|^2 \quad . \tag{2.19}$$

The electron-electron interaction includes the classical Coulomb energy, which is the *Hartree energy* $V_H[\rho]$, and the *exchange-correlation functional* $E_{xc}[\rho]$. Hence the energy functional is rewritten:

$$E[\rho] = T_n[\rho] + V_{ext}[\rho] + V_H[\rho] + E_{xc}[\rho] \quad , \tag{2.20}$$

where the Hartree energy is:

$$V_H[\rho] = \frac{1}{2}\int \frac{\rho(\mathbf{r}_1)\rho(\mathbf{r}_2)}{\left|\mathbf{r}_1 - \mathbf{r}_2\right|} d\mathbf{r}_1 d\mathbf{r}_2 \quad . \tag{2.21}$$

The exchange-correlation functional is defined as the sum of the error arising when a non-electron-interacting kinetic energy is used and the error arising when the classical electron-electron interaction is introduced:

$$E_{xc}[\rho] = (T[\rho] - T_n[\rho]) + (V_{ee}[\rho] - V_H[\rho]) \quad . \tag{2.22}$$

This is a *universal functional* which can be used for any studied material.

Applying the principle of least action (Eq. 2.15) for the energy functional (Eq. 2.20), which can be written explicitly in terms of the non-interacting orbitals (Eq. 2.19), results in a set of non-linear equations called *Kohn-Sham equations:*

$$\left[ -\frac{1}{2}\nabla^2 + v_{ext}(\mathbf{r}) + \int \frac{\rho(\mathbf{r}')}{|\mathbf{r}-\mathbf{r}'|} d\mathbf{r}' + v_{xc}(\mathbf{r}) \right] \phi_i^{KS}(\mathbf{r}) = \varepsilon_i \phi_i^{KS}(\mathbf{r}) \quad , \tag{2.23}$$

where $\Phi_i^{KS}(\mathbf{r})$ is the Kohn-Sham electron wave function and the *local exchange-correlation potential* $v_{xc}(\mathbf{r})$ is the derivative of the exchange-correlation functional, with respect to the density:

$$v_{xc}(\mathbf{r}) = \frac{\delta E_{xc}[\rho]}{\delta \rho} \quad . \tag{2.24}$$

The main task in DFT is solving the Kohn-Sham equations which have been derived using the Hohenberg-Kohn theorems. Solving these equations is subjected to how the exchange-correlation functional $E_{xc}[\rho]$ can be approximated. One of the first approaches is the *local density approximation* (LDA) [78] for $E_{xc}[\rho]$. In the LDA, an inhomogeneous system is treated as *locally-homogeneous*, and the functional is approximated as an integral of the *local functional* $\varepsilon_{xc}(\rho)$ multiplied with the electron density, over the system volume:

$$E_{xc}^{LDA}[\rho] \approx \int \rho(\mathbf{r}) \varepsilon_{xc}(\rho) d\mathbf{r} \quad . \tag{2.25}$$

The local functional $\varepsilon_{xc}(\rho)$ is the exchange and correlation energy density of the uniform electron gas of density $\rho$. It can be written as the sum of the exchange and correlation terms:

$$\varepsilon_{xc}(\rho) = \varepsilon_x(\rho) + \varepsilon_c(\rho) \quad . \tag{2.26}$$

The LDA is considered as the zeroth order approximation of the semi-classical derivative expansion of the density matrix, in terms of the electron density [79]. The *generalised gradient approximation* (GGA) [80,81] is a higher order of approximation, which introduces the first order gradient terms in the expansion to the local functional. The GGA functional is typically written as:

$$E_{xc}^{GGA}[\rho] \approx \int \rho(\mathbf{r})\varepsilon_{xc}(\rho, \nabla\rho)d\mathbf{r} \quad . \tag{2.27}$$

Compared with the LDA, the GGA describes the binding energy of molecules and solids better [82].

Solving the Kohn-Sham equations requires information about the molecular orbitals which is represented by some sets of functions called the *basis set.* These functions are usually atomic orbitals. In our work on metallic clusters, the *Gaussian-type-orbitals* (GTOs) in the *linear combination of atomic orbitals molecular orbital* (LCAO) method are used. There are two kinds of GTOs which are commonly used: *Cartesian* and *spherical GTOs*. For example, the spherical GTOs are represented in the form [83]:

$$\phi_{nlm}(\alpha, r) = N_{nl}(\alpha)e^{-\alpha r^2} r^l Y_{lm}(r) \quad , \tag{2.28}$$

where *n, l, m* are orbital quantum numbers, *r* is the length of the vector coordinate of electron, $\alpha$ is a real parameter, $N_{nl}(\alpha)$ is the normalization constant, $Y_{lm}(r)$ are spherical harmonics. *Effective core potentials* are commonly used in DFT calculations. They are *pseudo-potentials* which include the contribution of core electrons in an effective core. Thus, only chemically active valence electrons are dealt. The use of pseudo-potentials reduces the number of electrons and the basis set size.

## 2.1.6. Geometrical reoptimisation

In our work, we adopt an *empirical - ab initio combined approach* [84]. That is, the optimized structures of bimetallic clusters found by the BCGA search using the Gupta empirical potential (EP) are refined by DFT (the *ab initio level*) calculations. At this DFT level, the structures undergo local geometrical reoptimisations (relaxations). The methodology used here for the DFT geometrical optimisation is different from that for the BCGA: it is based on the vanishing of forces at potential extrema [85]. In principle, the cluster total energy $E_{tot}$ corresponding to a certain structure gives the forces:

$$F_{i\alpha} = -\frac{\partial E_{tot}}{\partial R_{i\alpha}} , \tag{2.29}$$

where $R_{i\alpha}$ is the $\alpha^{th}$ component of $R_i$ (coordinates of the $i^{th}$ atom). If the total energy does not reach an extremum, the forces will be non-zero and make atoms move to a new structure. At an extremum, the forces vanish and a stationary point is found. The structure will be accepted as a new optimized one if the extremum is a minimum (local minimum).

## 2.1.7. Electronic analysis

### 2.1.7a. HOMO-LUMO gap

In the electronic structures of molecules and clusters, the gap between the *highest occupied molecular orbital* (HOMO) and *lowest unoccupied molecular orbital* (LUMO) is an energy gap equivalent to the *band gap* between the top of the valence band and the bottom of the conduction band in the electronic band structures of bulk insulators and semiconductors [86]. The energy gap between the HOMO ($\varepsilon_{HOMO}$) and LUMO ($\varepsilon_{LUMO}$) energy levels (which are negative) is simply defined as the positive quantity:

$$\Delta\varepsilon_{HL} = \varepsilon_{LUMO} - \varepsilon_{HOMO} \quad . \tag{2.30}$$

Generally, the HOMO-LUMO gap can be considered as a measure of the *quantum excitability*. The source of the quantum excitations may be thermal, optical, external electric fields, etc. The larger the gap is, the higher the excitation energy is needed to move electrons from the HOMO level to the LUMO level. For the metallic clusters in our work, the HOMO is identified by filling up from the low to the high orbitals found by performing DFT calculations with all the available electrons. Once all the available electrons occupy the orbitals, the highest electron-occupied orbital is the HOMO, and the upper adjacent orbital is the LUMO.

### 2.1.7b. Mulliken population analysis

*Mulliken population analysis* (MPA) [87,88] is one of procedures in computational quantum chemistry for the estimation of *partial atomic charges* [89]. Basically, the MPA formalism is described below:

The electron density $\rho(r)$ can be integrated over all space to calculate the total number of electrons:

$$N_e = \int \rho(\mathbf{r}) d\mathbf{r} = 2\sum_{i=1}^{N_e/2} \int \phi_i^{KS*}(\mathbf{r}) \phi_i^{KS}(\mathbf{r}) d\mathbf{r} \quad . \tag{2.31}$$

After expanding the wave function $\Phi_i^{KS}(\mathbf{r})$ in terms of the eigenfunctions $b_\mu(\mathbf{r})$:

$$N_e = 2\sum_{i=1}^{N/2} \sum_{\mu=1}^{K} \sum_{\nu=1}^{K} C_{\mu i}^* C_{\nu i} \int b_\mu^*(\mathbf{r}) b_\nu(\mathbf{r}) d\mathbf{r} = 2\sum_{i=1}^{N/2} \sum_{\mu=1}^{K} \sum_{\nu=1}^{K} C_{\mu i}^* C_{\nu i} S_{\mu\nu} \quad , \tag{2.32}$$

where $S_{\mu\nu} = \int b_\mu^*(\mathbf{r}) b_\nu(\mathbf{r}) d\mathbf{r}$ is the matrix element of the overlap matrix of the basis functions, $C_{\mu i}$ is the expansion coefficients, $K$ is the number of the eigenfunctions . The density matrix is defined as:

$$D_{\nu\mu} = 2\sum_{i=1}^{N/2} C_{\mu i}^* C_{\nu i} \quad , \tag{2.33}$$

and:

$$D_{\nu\mu} = 2\sum_{i=1}^{N_e/2} C_{\mu i}^* C_{\nu i} \quad . \tag{2.34}$$

If the sum in Equation 2.34 is taken over only one index, we obtain the *gross orbital population* (*GOP*):

$$GOP_\nu = \sum_{\mu=1}^{K} D_{\nu\mu} S_{\mu\nu} \quad . \tag{2.35}$$

The *gross atom population* for an atom A ($GAP_A$) is calculated by summing the *GOP* over all basis functions centered at the atom A (the number of these basis functions is $v_A$):

$$GAP_A = \sum_{\nu=1}^{v_A} GOP_\nu \quad . \tag{2.36}$$

The *Mulliken atomic charge* $Q_M(A)$ for the atom A is defined as the difference between the number of available electrons $N_a(A)$ and the $GAP_A$:

$$Q_M(A) = N_a(A) - GAP_A \quad . \tag{2.37}$$

In our work, MPA is performed to calculate the Mulliken atomic charges, investigating the charge transfer between atoms in bimetallic clusters (Chapter 3 and Chapter 6).

## 2.2. Synthesis of nanoparticles

### 2.2.1. Wet-chemistry

There are various methods for fabrication of metallic nanoparticles. These methods can be generally classified into two categories: *top-down* approaches and *bottom-up* approaches [90]. The top-down fabrications often use physical treatments, such as mechanical, thermal or irradiative methods, to divide bulk metals in to nano-scale structures. In contrast, the bottom-up approaches grow metallic nanoparticles from single atoms or ions which can be generated either in a gas phase or in a solution. *Wet-chemical methods* [8] are bottom-up methods, in which nanoparticles of rather uniform sizes and shapes are grown via chemical reactions in solutions. This kind of methods generally uses *capping agents* (or *passivating ligands*) [92] which are often organic molecules to protect nanoparticles (i.e., prevent

agglomeration). The most typical treatments used in wet-chemical methods are chemical reduction of metal salts and thermolytic decomposition of preformed organometallic compounds.

The first wet-chemically synthesized nanoparticles are actually the historical Au nanoparticles made by Michael Faraday [2]. In his experiment, citrate ions were used to reduce $Au^{3+}$ ions to metallic Au atoms. The citrate ions do not only play a role in controlling the growth of Au atoms to the metallic nanoparticles which are suspended in water but also, importantly, serve as the capping agent with the Coulomb electrostatic repulsion preventing particle agglomeration. Nowadays, wet-chemical methods have been developed systematically [8]. There are two types of wet-chemical syntheses: *single-phase* and *two-phase*. Faraday's particles reduced in an aqueous solution are an example of nanoparticles synthesized via single-phase reactions. In two-phase reactions, nanoparticles are formed at the interface between an aqueous layer containing the dissolved metal salt and an organic layer (organic solvents which are immiscible with water, such as benzene and toluene) containing the reducing agents and capping agents (stabilisers) [91]. Besides citrates, other reducing agents such as borohydrides and alcohols are used commonly. Wet-chemical nanoparticles are usually dispersed and suspended as colloids either in aqueous media or in organic solvents. Nanoparticles in aqueous media (water-soluble) are called *hydrosols* which can either be sterically or electrostatically stabilized, while nanoparticles in organic solvents (lipid-soluble) or *organosols* are only stabilized by steric effects [8]. As mentioned above about Faraday's particles, citrate stabilization is an electrostatic stabilization. Polymers are known to have steric effects which help stabilizing both hydrosols and organosols. Among the most common polymers used as stabilizing agents are polyvinyl pyrrolidone (PVP),

polyvinyl alcohol (PVA), and polymethyl vinylether. Beside citrate and polymeric ligands, alkanethiols ($CH_3(CH_2)_nSH$) are also well-known as effective capping agents [8].

Generally, a wet-chemical synthesis includes three steps: nucleation (seeding), particle growth and growth termination by ligand capping [8, 92]. The nucleation and growth processes are essentially subjected to the degree of solution supersaturation, temperature, and the surface tension at the solid-liquid interface. There is an important process occurring during the particle growth called *Ostwald ripening* [93] which is a mechanism of dissolving and releasing monomers or ions from small particles leading to the growth of larger particles. In this mechanism, there is a driving force causing the size-dependence of the particle solubility: larger particles have lower solubility. It is Ostwald ripening that is the main mechanism for the establishment of the high *monodispersity*, or the high uniformity in size, of nanoparticles synthesized by wet-chemical methods. However, the growth process can also be interfered by the activity of capping agents. The solubility of nanoparticles can be affected by the interactions between the metal surfaces and the passivating ligands, as well as by the ligands themselves [94]. High concentrations of capping agents can terminate the growth process early. All the three steps nucleation, growth and termination are interrelated to each other. Thus, the relative rates of the steps can be altered by varying experimental parameters such as concentrations and temperature to produce particles of different size distributions from the same reaction procedure [92].

Bimetallic nanoparticles can be synthesized using wet-chemical methods, via either *co-reduction* or *successive reduction* procedures [95]. In the co-reduction procedure, the solutions of the two metal salts are mixed from the beginning of the reaction. Generally, the metal species with the higher redox potential is reduced and precipitated first, establishing a core. Then the other species should be reduced later and deposited on this core as a coating

layer. Ideally, this scenario can establish a core-shell configuration for the bimetallic nanoparticles. However, countering this tendency, some surface-capping agents can bonds much more strongly to the metal with higher redox potential, drawing this metal species out to the surface [96]. Hence, the configuration may be altered by varying the concentrations of capping agents. In the successive reduction procedure, the monometallic nanoparticles are synthesized first, and then the solution of a different metal species is added into the reaction. This procedure is considered as one of the most commonly-used methods for the attempts to establish core-shell configurations [95]. The second metal species is expected to be deposited on to the surface of the preformed monometallic seeds either by reducing agents or by *galvanic exchange reaction* [14,97] between the two species.

In relevance to our work, we describe below two specific wet-chemical methods: the Turkevich-Frens method [10,11], polyol method [105,106], and the Brust-Schiffrin method [12,98] which are the fundamentals for our syntheses of bimetallic nanoparticles. In our work, the bimetallic Cu-Au nanoparticles (Chapter 4) are synthesized using the Brust-Schiffrin method combined with successive reduction (galvanic exchange) procedure, and the bimetallic Pt-Au particles (Chapter 7) are synthesized using two different methods: the *polyol method* and Turkevich-Frens method combined with the *Schmid successive reduction* procedure [13].

### 2.2.1a. Brust-Schiffrin method and galvanic exchange reaction

The *Brust-Schiffrin method* [12,98] is a two-phase wet-chemical method for reduction of metallic nanoparticles. This method was developed in 1994 and has been widely used to prepare organosols, or nanoparticles dispersed in organic solvents. The two phases used for the reaction are commonly water and toluene. The first mechanism in the synthesis is the

transfer of aqueous metal ions from the water layer to the toluene layer. This transfer is induced by the introduction of the phase transfer catalyst tetraoctylammonium bromide (TOAB) (or other halogenides) which also has a stabilization role. The main stabilizing agent (capping agent) alkanethiols, which also serve as an intermediate-reducing catalyst is initially dissolved in the toluene layer. When transferred to the organic layer, the metal ion complex is reacted with the alkanethiols to form polymeric thiolates. Aqueous borohydride (often $NaBH_4$ or $KBH_4$) is added as the reducing agent which reduces the metal from its thiolate complex at the interface of water and toluene. The alkanethiol molecules now function as the capping agents. The Brust-Schiffrin method was initially developed for synthesis of Au nanoparticles capped with thiol molecules, exploiting the knowledge that thiols bond effectively to Au surface, forming monolayers [99, 100]. Nanoparticles which are effectively capped with monolayers of thiol molecules are also called *monolayer protected clusters* (MPC) [14]. Figure 2.4 shows a scheme for a refined Brust-Schiffrin synthesis of Au nanoparticles [101].

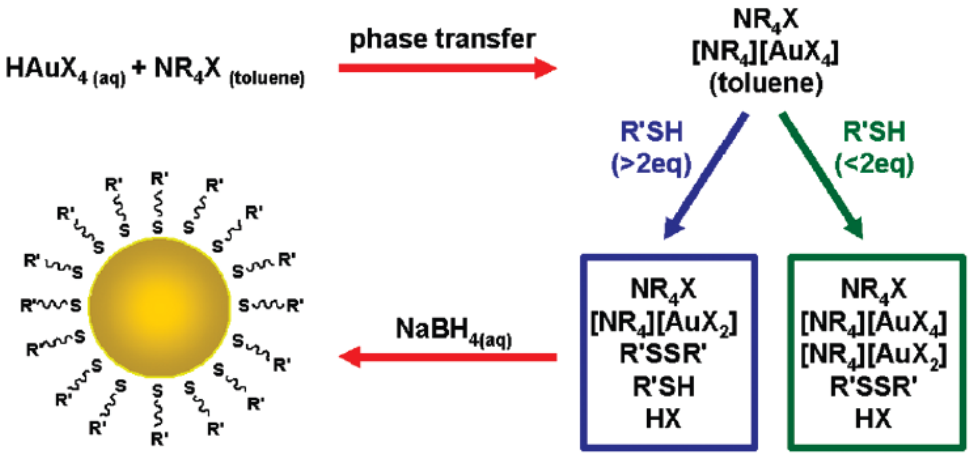


**Figure 2.2.** Scheme for a refined Brust-Schiffrin synthesis of Au nanoparticles [101]: the aqueous complex of gold salt $HAuX_4$ is transferred to toluene by forming the complex $[NR_4][AuX_4]$ with the tetraoctylammonium halogenide $NR_4X$; adding different ratios of alkanethiols (>2eq and <2eq) may result in two different thiolate complexes; finally, adding aqueous sodium borohydride $NaBH_4$ reduces Au nanoparticles capped with alkanethiol molecules.

Besides Au nanoparticles, the Brust-Schiffrin method has been adapted for syntheses of nanoparticles of other metals such as Ag, Pd, and Cu [97,101-103]. Typically, the method produces nanoparticles of around 1 – 3 nm in diameters. However, the concentration of borohydride and the alkane chain-length have some influences on the particle sizes [8,104].

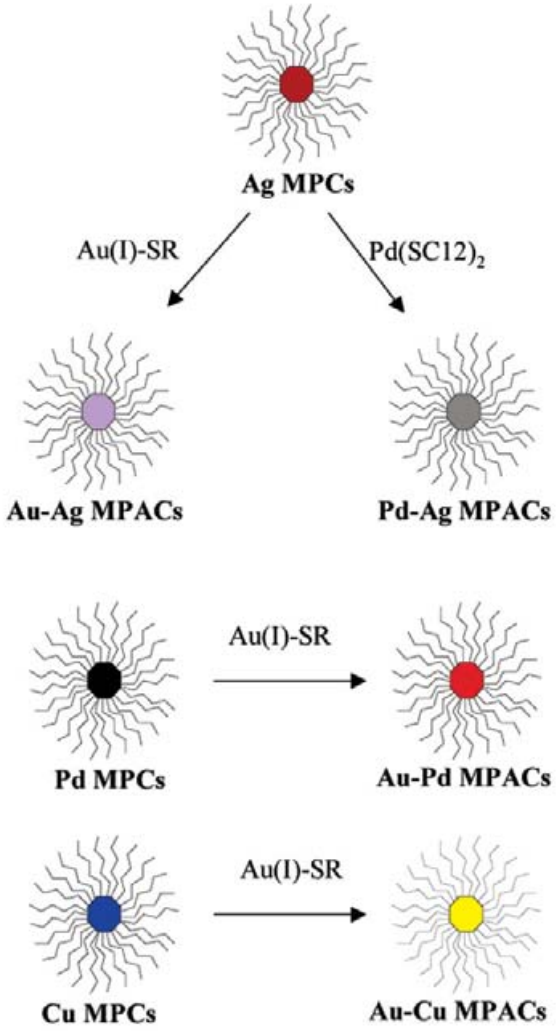


**Figure 2.3.** A scheme representing the galvanic exchange reactions to synthesize MPACs (monolayer-protected alloy clusters) from MPCs [14].

Thiol-monolayer capped monometallic particles can be used as the metal cores to synthesize stable bimetallic particles via galvanic exchange reactions which replace the surface atoms of the metal cores with the atoms of more noble metals [14,97]. The galvanic exchange procedure is performed by letting the thiol-protected A monometallic particles

react with the solution of $B^{n+}$ thiolate complex, where the metal B is more noble than A. For example, the thiolate complexes of Au and Pd are $[Au^{I}SCH_2\text{-}C_6H_4C(CH_3)_3]$ and $[Pd^{II}\{S(CH_2)_{11}CH_3\}_2]$, respectively. In the redox reaction between A and $B^{n+}$, A is the electron donor and $B^{n+}$ is the electron acceptor. The redox reaction is described as:

$$nA + mB^{n+} \rightarrow nA^{m+} + mB \quad . \tag{2.38}$$

A scheme for galvanic exchange syntheses of some bimetallic nanoparticles is shown in Figure 2.5 [14].

### 2.2.1b. Polyol method

The polyol method was developed by Figlarz and co-workers to synthesize metallic nanoparticles from metal salts, using polyols both as the reducing agent and the stabilizing agent [105,106]. The polyol itself is the solvent for the reaction, so no other solvents are required to dissolve the reactants. The most common polyol used in this method is ethylene glycol $HOCH_2CH_2OH$. The general procedure involves mixing metal salts with ethylene glycol and subsequently heating under reflux. This high temperature is required to lower the oxidation potential of the ethylene glycol. Once this oxidation potential is equal to the reduction potential of the metal ions, the reduction reaction will occur spontaneously, resulting in the nucleation of metallic nanoparticles. The reaction chain includes the dehydration of the ethylene glycol at high temperature, and subsequently the oxidation-reduction forming diacetyl and metallic atoms (see Figure 2.4).

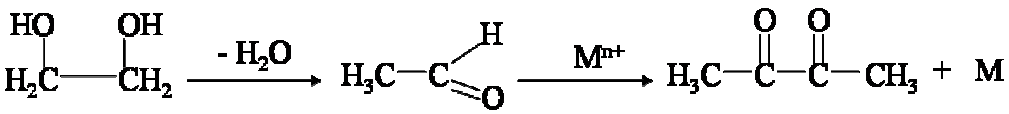


**Figure 2.4.** Diagram representing the reaction chain of ethylene glycol in the polyol method [106].

By the polyol method, large monometallic and bimetallic nanoparticles of different metals of around 100 nm to a few microns have been synthesized [107,108]. Small nanoparticles of a few nanometres can also be synthesized, as in the cases of Ru, Au, and Pt particles, with the introduction of PVP into the reaction as the capping agent [109, 110]. It has been reported that, the size distributions of these particles can be modified by varying the reaction temperature. By employing the successive reduction, PVP-capped Au-Pt bimetallic nanoparticles of around 2-4 nm have also been synthesized [110]. On the other hand, by using the co-reduction of mixed ions of Cu and Pd hydroxides, PVP-capped Cu-Pd bimetallic nanoparticles, which have an average diameter of 2 nm, have been obtained [111].

### 2.2.1c. Turkevich-Frens method and Schmid successive reduction

The Turkevich-Frens method involves employing citrate both as the reducing agent and the stabilizing agent for the reduction of Au nanoparticles in the hydrosol. After the Faraday's prototypes of colloidal Au, the synthesis procedure using citrates to produce Au hydrosols was first described by Hauser and Lynn in 1940 [112]. The citrate route to produce monodisperse Au nanoparticles has become popular after the development by Turkevich and co-workers in 1951 [10]. Basically, the Turkevich method is performed by adding chloroauric acid ($HAuCl_4$) to a boiling sodium citrate solution (at approximately $100^oC$) to obtain a ruby-red solution indicating the appearance of Au hydrosols. The Turkevich method can produce monodisperse Au nanoparticles of around 20 nm. By varying the concentration ratio between the chloroauric acid and the sodium citrate, the sizes of the nanoparticles can be altered from around 10-100 nm. As the citrate ions act as the (electrostatically stabilizing) capping agent, a lower citrate concentration will result in larger particles, due to the aggregation between small particles. The aggregation continues until the total surface area of all particles becomes small enough to be saturately capped by all citrate ions available in the

solution. The Turkevich method was continued to be refined by Frens and co-workers in 1973 [11].

The Frens' development has improved the size controllability of the method. Using this method, the size of the Au nanoparticles can be somewhat predetermined (in the range of around 16-147 nm) by choosing an appropriate citrate/gold ratio. Bimetallic nanoparticles can also synthesized by the Turkevich method. For example, the citrate co-reduction performed for a mixture of chloroauric acid and chloroplatinic acid can produce bimetallic Au-Pt nanoparticles [113].

From the citrate-reduced Au nanoparticles of around 18-19 nm, bimetallic Au-Pd and Au-Pt nanoparticles can be synthesized via a successive reduction procedure developed by Schmid and co-workers [13]. This procedure is performed to coat the preformed citrate Au nanoparticles with Pt or Pd shells by reducing $H_2PtCl_6$ or $H_2PdCl_4$, respectively, in the presence of the Au particles as the seeds for the successive precipitation of Pt or Pd. As the indication of the coating, the mixture after the reaction turns from ruby red of the Au nanoparticles to the dark brown or silver-grey of Pt or Pd species, respectively. The Schmid procedure was further applied for the formation of $Au_{core}Pt_{shell}$ nanoparticles with the introduction of ascorbic acid as a reducing agent for $H_2PtCl_6$ [30,114], in which the size of the final particles could be described in the following relation:

$$D = D_{core}\left[1+\frac{V_m(Pt)[Pt]}{V_m(Au)[Au]}\right]^{1/3} \quad , \tag{2.39}$$

where $D$ is the diameter of the final $Au_{core}Pt_{shell}$ nanoparticles, $D_{core}$ is the diameter of the Au seeds, $V_m(Pt)$ and $V_m(Au)$ are the mole volumes, $[Pt]$ and $[Au]$ are the overall concentrations

of the two metals. The thickness of the Pt shell can be tuned by varying the concentration of the $PtCl_6^{2-}$ ions.

## 2.2.2. Microbial methods

Our work includes the characterization of the bimetallic Pd-Au nanoparticles which were synthesized using bacteria (by Deplanche and Macaskie at the school of Biosciences, University of Birmingham). The microbial methods for syntheses of metallic nanoparticles are briefly described.

Biological methods have been recently developed for synthesis of metallic nanoparticles, in which microorganisms (i.e., bacteria) are used as "nanofactories" [115,116]. In comparison with conventional physicochemical methods, the synthesis methods employing bacteria or microbial methods have special advantages such as the high commercial benefits due to the high production rate, as well as less reducing agents and energy required, eco-friendly process, and ambient conditions (often room temperature and atmospheric pressure). Microbial methods have been also reported to be promising methods for the economical biorecovery of Au from jewellery wastes [117].

Experimental production of microbial nanoparticles in laboratories generally requires the same metal source as in wet-chemical methods. For example, the microbial synthesis of Au nanoparticles will require the solution of $HAuCl_4$. The size, monodispersity, shape and chemical composition (for bimetallic particles) of the microbially synthesized are affected by the experimental conditions such as pH, incubation time, light intensity, temperature and the culture medium [118]. For example, the size and the deposition site of Au nanoparticles synthesized using *Shewanella algae* bacteria are sensitive to pH: at pH = 7, the production of 10-20 nm particles occurred at the periplasmic space; at pH = 2.8, the production of 15-200

nm particles occurred on the bacterial cells; at pH = 2, particles of around 20 nm in size were distributed intracellularly and large particles of around 350 nm in size were distributed extracellularly [119].

The syntheses of Au and Pd nanoparticles using *Escherichia coli* and *Desulfovibrio desulfurican* bacteria have been recently developed [117,120,121]. $HAuCl_4$ and $[Pd(NH_3)_4]Cl_2$ are reduced in the presence of $H_2$ as the electron donor, forming metallic Au and Pd nanoparticles of the range size ~20-50 nm distributed in the periplasmic space and on the bacterial cell surface. Besides, small particles of around 5 nm in size are also deposited in the intracellular sites. It has been described that the enzyme *hydrogenase* existing in the microbial periplasmic space involves in the reduction of the $Pd^{2+}$ ions and the formation of the metallic Pd particles [122]. For the reduction of the $Au^{3+}$ ions, the hydrogenase has also been reported to play a significant role [117]. The size and shape of the Au particles are also known to be sensitive to the pH of the culture medium: at pH = 3, spherical and monodisperse particles having an average diameter of 10 nm are observed; a mixture of ~10 nm and ~ 50 nm particles having triangular prism, truncated-octahedral and rod shapes are observed at pH = 5 [119].

The successive reduction procedure can be combined with the microbial reduction process to synthesize bimetallic nanoparticles. The bimetallic Pd-Au nanoparticles in our work (Chapter 5) have been synthesized by sequential reductions of $Pd^{2+}$ and $Au^{2+}$ ions in the medium of D. desulfurican bacteria and $H_2$.

## 2.3. Transmission Electron Microscopy

Transmission electron microscopy (TEM) [123] is a powerful technique for characterization of nanomaterials, especially nanoparticles. TEM is excellent for imaging nanoparticles

typically of a few nanometres, revealing the size distribution, morphology, and crystalline structure of these particles. Although the surface morphologies of nanomaterials in general have been widely investigated using other sophisticated techniques such as scanning tunnelling microscopy (STM) and atomic force microscopy (AFM), which can resolve atoms, nanoparticles having their surfaces capped with organic layers can not be characterized sufficiently well by these techniques. TEM, a "penetrating" technique, is unique in its real-space imaging at atomic resolution of nanoparticles through their entire thicknesses, regardless of the capping organic molecules on the surface [124]. The control of observation direction in TEM and the image analysis available allow the visualization of the three-dimensional morphology. The intensity of the electron beam in the TEM can be adjusted to observe either nanoparticles with minimized damages or to study structural evolution driven by electron impact. Physical phenomena arising from the impact between matter and the electron beam lead to many TEM-based techniques which are extremely useful in characterizing the chemical composition, the elemental distribution at high-spatial-resolution and the electronic structure of nanoparticles. These techniques make TEM, one more time, unique in mapping the local composition and structure of a single nanoparticle by using a *nanoprobe* (can be smaller than 1 nm) formed from a finely focused electron beam.

We describe here the TEM and TEM-based techniques which has been used for the characterization of bimetallic Cu-Au, Pd-Au, and Pt-Au nanoparticles: high resolution TEM (HRTEM), high angle annular dark field (HAADF)-scanning TEM (STEM), electron tomography, energy dispersive X-ray (EDX) mapping, and electron energy loss spectroscopy (EELS).

### 2.3.1. HRTEM

The first most basic and simple explanation for the high resolution of TEM involves the wave nature of the electrons [125]. The shortest wavelength of visible light is around 400 nm and that is the reason why the conventional optical microscope can not resolve a distance shorter than around 200 nm. The wavelength of high kinetic-energy electrons, however, is much shorter (for example, 200 keV electrons have a wavelength of approximately 0.0025 nm) which implies a much higher resolution if the wave nature of the electrons is employed via an imaging technique. That idea was fundamental to the construction of the first electron microscope [126].

A modern TEM consists of an illumination system, a specimen stage, an objective lens, a magnification system, systems for data recording, and a system for elemental analysis [124]. The lenses in TEM use magnetic fields created by sophisticated coils with electric currents. These magnetic lenses bend the electron beam in a similar way to that in which an optical lens bends transmitted light. The central part of the illumination system is the electron gun which can be either thermionic emission type or field emission type. The field emission gun gives a more coherent and finer electron beam with a high current density, increasing the spatial resolution in nanoanalysis. Other important parts of the illumination system are the condenser lenses which help to form a fine electron probe. The specimen stage incorporates mechanisms to move and tilt specimens. The objective lens system crucially affects the resolution offered by the microscope. The system for magnification is built with intermediate lenses and projection lenses which can give a magnification of up to around 1.5 million. The data recording systems can include both a plate camera and a digital camera using a charge coupled device (CCD). The systems for elemental analysis generally are EDX and EELS.

Basically, the *electron optics* for TEM is analogous to the conventional optics of light. However, due to the very short wavelengths of electrons, there are some distinguishing phenomena in the TEM such as the diffraction of electrons by the periodic structures of specimens. The mechanism for image formation is illustrated in a simplified diagram (Figure 2.7), where only a single objective lens is included. This objective lens mainly determines the resolution of the TEM. The specimen is illuminated with a nearly parallel electron beam. The transmitted beam consists of two main components: the direct beam formed by the electrons transmitted through the specimen without a change in direction and the diffracted beam which makes with the direct beam an angle $2\theta$ according to Bragg's diffraction law [127]:

$$n\lambda = 2d\sin\theta \quad , \tag{2.40}$$

where $n$ is an integer, $\lambda$ is the electron wavelength, and $d$ is the spacing between atomic lattice planes.

The changes in phase and amplitude of the electron waves due to the electron-specimen interactions can be described by quantum mechanics. The electron wave before the specimen can be simplified as a plane wave $\psi_o$ . The interaction with the specimen changes the wave function $\psi_o \rightarrow \psi(\boldsymbol{r})$ where $\psi(\boldsymbol{r})$ is the transmitted wave function which contains the physical information of the specimen. Through the optic system, this wave is transmitted nonlinearly.

If the objective lens is ideally assumed to be a perfect thin lens, the parallel direct and diffracted beams, similar to light optics, are expected to be focused in the back focal plane. Diffracted parallel rays which are at the same angle $2\theta$ will be focused at the same point on the back focal plane, forming a diffraction pattern. The phase shift of the electron is known

to be a function of the diffraction angle $\theta$. There are two factors causing the phase shift: the spherical aberration which is associated with a change in focal length and the defocus of the lens which is involved with the spherical characteristics of the transmitted wave.

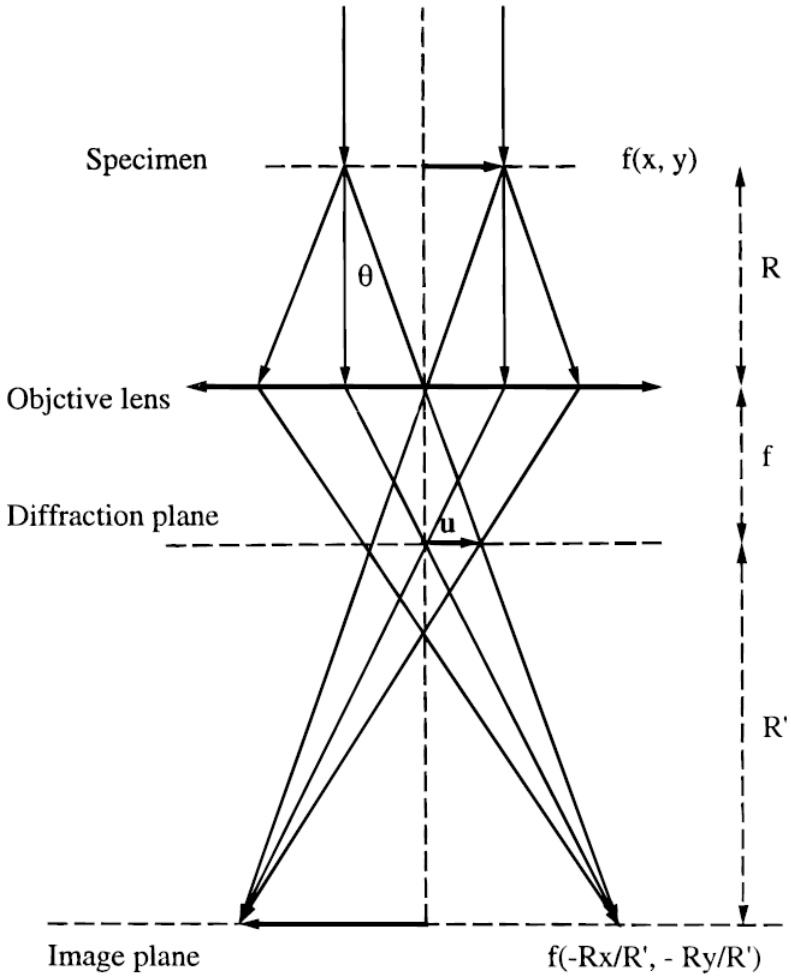


**Figure 2.5.** Diagram of image formation in a simplified one-lens TEM [124].

The diffraction amplitude function at the back focal plane is:

$$\psi'(\mathbf{u}) = \psi(\mathbf{u})\, e^{i\chi(\mathbf{u})} \quad , \tag{2.41}$$

where $\psi(\boldsymbol{u})$ is the Fourier transform of $\psi(\boldsymbol{r})$ at the exit face of the specimen, $\boldsymbol{u}$ is the reciprocal vector having modulus $u = 1/d$, $\chi(\boldsymbol{u})$ is the phase function determined by the lens defocus $\Delta f$ and the spherical aberration coefficient $C_s$ of the objective lens:

$$\chi(\mathbf{u}) = \frac{\pi}{2} C_s \lambda^3 u^4 - \pi \Delta f \lambda u^2 \quad . \tag{2.42}$$

It is the interference of the Bragg diffracted beams that forms an HRTEM image. The imaging information of the object is transmitted nonlinearly because diffracted beams of different diffraction angles have difference phase shifts induced by the spherical aberration and the defocus. The intensity of the observed image is:

$$I(x,y) = \left| FT^{-1}[\psi'(\mathbf{u})] \right|^2 = \left| \boldsymbol{\psi}(x,y) \otimes t_{obj}(x,y,\Delta f) \right|^2 \quad , \tag{2.43}$$

where $FT^{-1}[\psi'(\boldsymbol{u})]$ is the inverse Fourier transform of $\psi'(\boldsymbol{u})$, $t_{obj}(x,y,\Delta f) = \mathrm{FT}^{-1}[\exp(i\,\chi(\boldsymbol{u})]$, $\otimes$ denotes convolution between $\psi(x,y)$ and $t_{obj}(x,y,\Delta f)$. This equation is essentially Abbe's imaging theory which describes the relation between the object wave function $\psi(\boldsymbol{r})$ and the observed image intensity distribution $I(x,y)$.

There are three main types of contrast in TEM imaging: diffraction contrast, phase contrast and thickness/atomic-number contrast. Diffraction contrast originates strain of the crystal which perturbs the intensities of the diffraction beams. Diffraction contrast can give useful information for large nanoparticles (> 15 nm) which are more likely to have grain boundaries or other defects.

Phase contrast is caused by the phase modulation which occurs when the electron waves transmit through the crystal potential. Phase contrast can reflect the distribution of atoms in

the specimen. The phase modulation of the electron waves in the crystal potential *V(x,y,z)* can be described approximately in a presentation of wave function at the exit face of a thin specimen:

$$\psi(x,y) = e^{i\sigma V_p(x,y)} \quad , \tag{2.44}$$

$V_p(x,y) = \int_0^d V(x,y,z)dz$ is the thickness-projected potential,

where $\sigma$ is the interaction parameter. In the case where the electron beam is transmitted along a low-index zone axis, because each atom in the specimen can be considered approximately as a narrow potential well having a width of around 0.2-0.3 Å, the variation of $V_p(x,y)$ across atom rows will be saw-tooth-like. This behaviour of $V_p(x,y)$ is the basis of atomic-resolution in HRTEM imaging.

Thickness/atomic-number contrast relates intimately to the scattering of electrons by the specimen atoms. The number of scattering incidents increases with the specimen thickness along the beam direction. If the image formation derives from electrons scattered to high angles (Rutherford-like scatterings), the image intensity will be sensitive to the average atomic number along the beam direction.

If the specimen is thin enough for $|\sigma V_p(x,y)| << 1$ the wave function in Eq. 2.44 can be approximated to the first order term:

$$\psi(x,y) \approx 1 + i\sigma V_p(x,y) \quad , \tag{2.45}$$

and Equation 2.43 becomes, ignoring the $\sigma^2$ term:

$$I(x,y) \approx 1 - 2\sigma V_p(x,y) \otimes \mathrm{Im}[t_{obj}(x,y,\Delta f)] \quad . \tag{2.46}$$

The second term in Equation 2.46 represents the interference between the directed beam and the diffracted beams. The contrast variation in the observed image is subject to the phase shift caused by the objective lens (i.e., the defocus of the lens). Although the first-order approximation in Equation 2.45 is often insufficient to describe the practical object-scattering phenomenon, Equation 2.46 is still useful as a simple and effective way to interpret the physics of HRTEM imaging. Here, a TEM image is actually a two-dimensional projection of the object, in which atom columns can be resolved and projected as spots in the observed image if they are parallel with the incident beam. As mentioned above, the effects of the objective lens include the spherical aberration and the defocus. In a TEM, the spherical aberration coefficient $C_s$ is fixed and only the defocus $\Delta f$ can be varied. It is the variation of the defocus that alters the contrast in an HRTEM image. Subject to the defocus, the two-dimensional projection of atomic columns can be alternated bright spots and dark spots in the observed image. Figure 2.8 represents simulated HRTEM images of a decahedral Au particle with different orientations and different defocus values. [124,128].

There are two basic types of TEM imaging: the *bright-field* mode and *dark-field* mode. These correspond to the direct and diffracted beams. The bright-field mode is selected when a small objective aperture is centred on the (000) optical axis so that the image is formed predominantly by the direct beam. In the dark-field mode, the direct beam is excluded as the objective aperture is placed at a particular off-axis position to allow only one (or a few) diffracted beam(s) to form the image. A dark-field image exhibits diffraction contrast which is sensitive to the specimen thickness and the lattice distortion. Normally, HRTEM imaging is performed in the bright-field mode with the inclusion of a few diffracted beams. When a

specimen crystal is oriented along a low-index zone axis (e.g., [110] or [100]), the interference between the strong diffracted beams and the direct beam will form the phase contrast image. HRTEM imaging is mainly governed by two important factors: the astigmatism and the defocus of the objective lens.

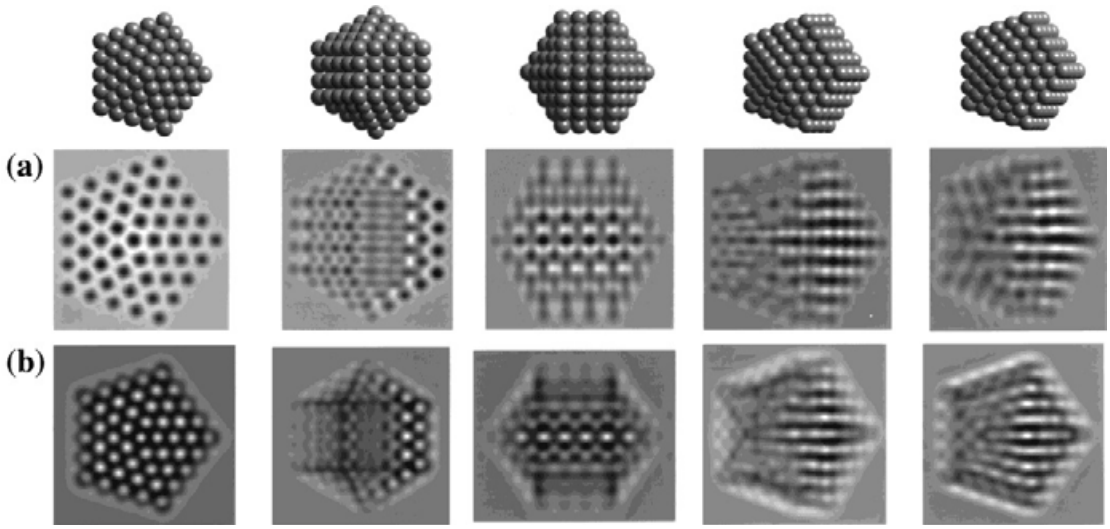


**Figure 2.6.** The contrast reversal in simulated HRTEM image for a decahedral Au particle in various orientations: a) defocus $\Delta f = 42\ nm$; b) defocus $\Delta f = 70\ nm$ [124, 128].

## 2.3.2. HAADF-STEM

High angle annular dark field – scanning transmission electron microscopy (HAADF-STEM) was developed the period from 1970 [129] to the early 1990s [130,131] and has become a powerful technique in the characterization of materials, especially nanomaterials like nanoparticles. HAADF-STEM is uniquely excellent in imaging heterogeneous systems where the atomic number, or *Z contrast*, is revealed, based on the elastic electron scattering by specimen atoms at high angles. The correlation with specimen thickness is another useful characteristic of HAADF-STEM signals, which offers semi-quantitative characterization of the dimensions of nanostructures.

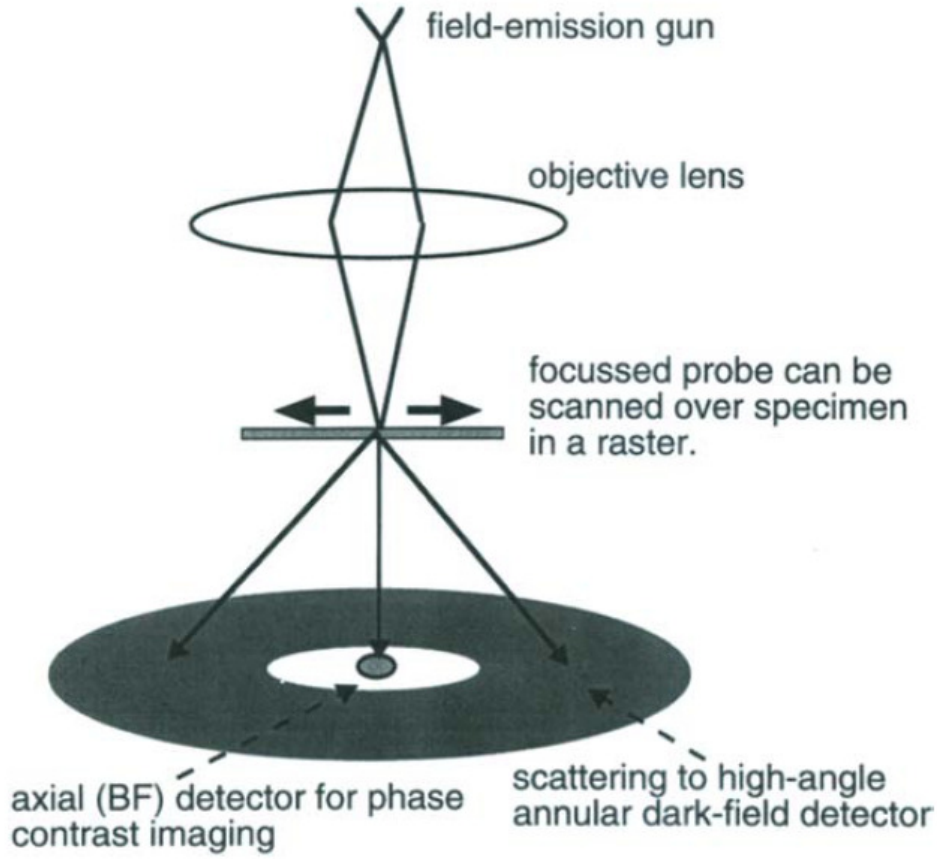


**Figure 2.7.** Schematic description of scanning transmission electron microscopy (STEM) with the bright-field (BF) and the annular dark-field (ADF) detectors [132].

HAADF-STEM is one of the options for the collection of the electrons in STEM mode (which has a reversed optical system compared with conventional TEM (CTEM)). In STEM mode, a very small electron probe (often generated from a field emission gun) is used to scan over the specimen in a raster fashion (see Figure 2.9 [132]). The directly transmitted electron and scattered electrons can be collected and transformed to images which are functions of the electron probe position. A bright-field STEM (BF-STEM) image is formed by collecting the directly transmitted and low-angle (typically < 10 mrad) scattered electrons which are close to the optical axis. Elastically scattered electrons are collected by an annular dark-field (ADF) detector to obtain ADF-STEM images. When the ADF detector is set to collect

electrons at high scattering angles (typically > 40-50 mrad), HAADF-STEM images are obtained.

An important distinction in the mechanism of image formation is that while CTEM imaging is *coherent*, HAADF-STEM is based on the *incoherent* scattering in which the thermal vibration of specimen atoms is considered (*thermal diffusion scattering*). The differences between coherent and incoherent image formation have been described by Lord Rayleigh in his paper on the resolution limit of optical microscopes (1896) [133]. Compared with coherent imaging, incoherent imaging gives significantly better resolution with a more truthful representation of the studied object. Although the physics behind ADF-STEM is more complicated than the assertion that incoherent TEM imaging simply requires the collection of incoherent thermally scattered electrons, ADF-STEM techniques are widely believed to allow direct visual interpretation [132].

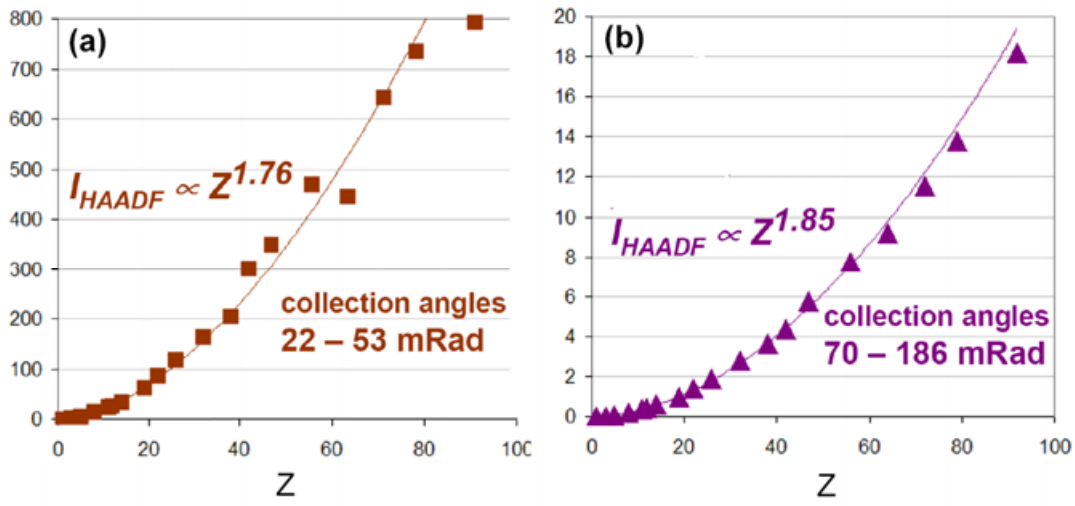


**Figure 2.8.** Measured and fitted dependence of HAADF intensity on the average atomic number (Z): **(a)** measured (squares) and fitted (solid line) intensities $I_{HAADF} \sim Z^{1.76}$ for a collection angle range of 22-53 mrad; **(b)** measured (triangles) and fitted (solid line) intensities $I_{HAADF} \sim Z^{1.85}$ for a collection angle range of 70-186 mrad [134].

Rutherford-like scattering is the physical nature of the Z-contrast in ADF-STEM. The laws for this type of scattering determine the dependence of the scattering cross section, and thus the image intensity, on the atomic number. HAADF-STEM intensity is a power function of the atomic number: $I_{HAADF} \sim Z^{\alpha}$ , where $\alpha$ can be between 1.6-2, depending on the range of collection angles. Figure 2.10 shows the measured and fitted dependence of $I_{HAADF}$ on the atomic number $Z$: $\alpha \approx 1.76$ for a collection angle range of 22-53 mrad (Figure 2.10a); $\alpha \approx 1.85$ for a collection angle range of 70-186 mrad (Figure 2.10.b) [134].

### 2.3.3. Electron Tomography

Tomography is a technique performed to obtain a three-dimensional (3D) visualization of the object studied [135]. In principle, transmission electron tomography includes two steps. The first step is acquiring a tomographic dataset, in which a number of images are recorded at different orientations of the specimen. This set of images is called a *tilt series*. The resolution ($d$) of a tomographic visualization depends on the number of images ($N$) acquired in the tilt series and the diameter (D) of the tomographic volume [136]:

$$d = \frac{\pi D}{N} \quad . \tag{2.47}$$

The second step is the alignment and reconstruction. The different views in the acquired tilt series are realigned precisely with respect to each other. It is essential that a common axis of rotation for the dataset, which crosses through the centre of the tomographic volume, is determined in this alignment process. The aligned dataset is then reconstructed to obtain the 3D visualization. The mathematical basis of tomographic reconstruction is the *projection-slice theorem*. In brief, this theorem states that *the Fourier transform of any 2D projection*

*image* (i.e., TEM/STEM images) *taken from a 3D object is a 2D slice at the same angle of projection through the 3D Fourier transform of the object being projected* [137, 138]. For example, the tilt series can be considered as 2D slices describing the 3D Fourier transform of the object. The reconstruction is performed by using algorithms based on the projection-slice theorem. From the output of the reconstruction procedure, a 3D visualization (tomograph) of the studied object can be obtained and displayed using appropriate visualization software.

Electron tomography can be performed in either CTEM or STEM imaging modes. Diffraction contrast and Fresnel fringes, however, are the problems frequently encountered when using CTEM for electron tomography; these may cause serious errors and artefacts. HAADF-STEM imaging, which can be considered incoherent, is more appropriate for tomography, because this technique effectively excludes phase and diffraction contrast [139, 140]. In HAADF-STEM mode, coherency effects can be minimized by choosing a sufficiently large inner collection semi-angle, typically $\theta_{HAADF} \geq 20$ mrad. Another advantage is that HAADF-STEM can provide Z-contrast which intensifies the contrast between high atomic-number objects (e.g., metallic nanoparticles) and low atomic-number supporting media (e.g., carbon thin film), and thus reduces unwanted signals from the medium.

In our work, HAADF-STEM tomography is performed on microbial bimetallic Pd-Au nanoparticles (Chapter 5).

### 2.3.4. EDX using a Silicon Drift Detector

Energy dispersive X-ray spectroscopy (EDX) is a chemical analysis technique which can be based on electron microscopy [141]. The physics behind this type of analysis is the interactions of fast electrons with the specimen, which produce X-rays characteristic of the elements present in the specimen. The electrons accelerated by the TEM system can knock

the inner-shell electrons of specimen atoms out of their orbits, bringing these atoms into excitation states. These atoms are relaxed when electrons in higher orbits (higher energy states) jump down to occupy the vacancies in the lower orbits, releasing an amount of energy via emitting either X-ray photons or electrons (*Auger electrons*). The X-rays emitted in such a way are discriminated from the continuous X-ray spectra (*Bremsstrahlung radiations*) generated when high energy electrons encounter the strong electric fields of atomic nuclei. They are characteristic of atomic structures of elements as their energies are equal to the energy differences between the higher and the lower atomic orbits. In EDX analysis, the characteristic X-rays can be collected to identify the corresponding elements present in the specimen. Table 2.1 shows transitions corresponding to some commonly observed characteristic X-rays lines [141].

**Table 2.1.** Some commonly observed characteristic X-ray lines [141].

| Line name | Transition | Line name | Transition |
|---|---|---|---|
| $K_{\alpha 1}$ | $L_{III}$–K | $L_{\alpha 1}$ | $M_V$–$L_{III}$ |
| $K_{\alpha 2}$ | $L_{II}$–K | $L_{\alpha 2}$ | $M_{IV}$–$L_{III}$ |
| $K_{\beta 1}$ | $M_{III}$–K | $L_1$ | $M_I$–$L_{III}$ |
| | | $L_{\beta 1}$ | $M_{IV}$–$L_{II}$ |
| | | $L_{\eta}$ | $M_I$–$L_{II}$ |
| | | $L_{\beta 4}$ | $M_{II}$–$L_I$ |
| | | $L_{\beta 3}$ | $M_{III}$–$L_I$ |
| | | $L_{\beta 2}$ | $N_V$–$L_{III}$ |
| | | $L_{\gamma 1}$ | $N_{IV}$–$L_{II}$ |
| | | $L_{\gamma 3}$ | $N_{III}$–$L_I$ |

An EDX system consists of a dedicated detector to collect characteristic X-rays, which is combined with a cooling mechanism, and analysis software. In general, an EDX detector

contains a crystal that releases free electrons when absorbing the energy of the incoming X-rays. The free electrons make the crystal become conductive and induce an electrical charge bias. In other words, the processes inside the detector convert the absorbed energies into electrical voltages or electrical pulses whose size corresponds to the characteristic X-rays of the element.

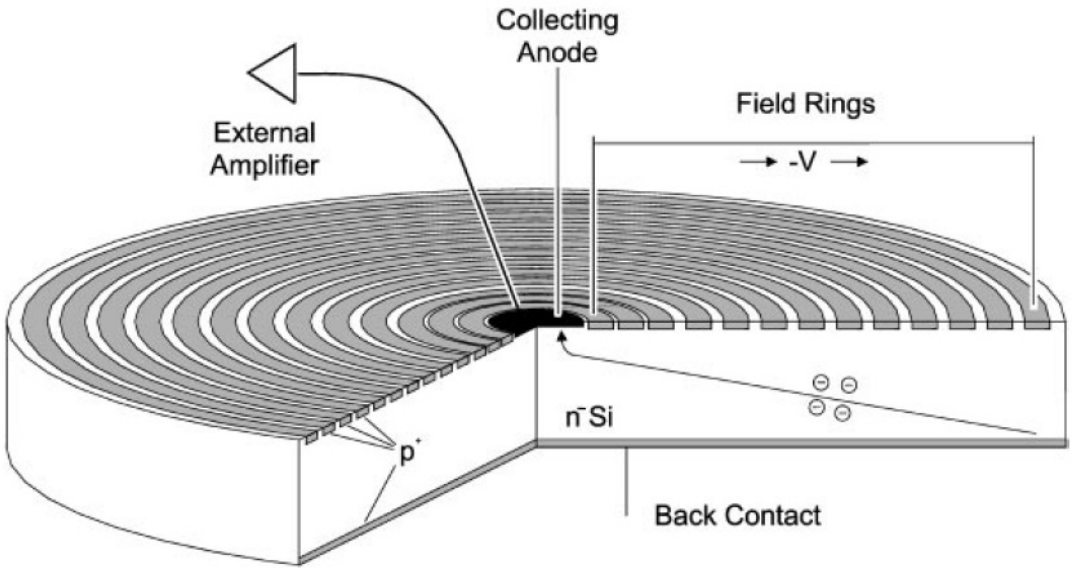


**Figure 2.9**. A SDD design optimised for X-ray spectroscopy. The drift field is generated by the concentric ring-shaped $p^+$ strip system, driving electrons toward the small collecting anode in the centre. The opposite surface is covered by a non-structured $p^+$ junction which acts as a homogeneous X-ray entrance window [142].

There are several types of EDX detector [141], but we only mention here the newly-developed Silicon Drift Detector (SDD) that was used in our work (Chapter 4, Chapter 5, and Chapter 7) to perform 2D element mapping and element line-scanning. A SDD consists of a high-resistivity silicon crystal with a series of concentric electrodes designed to generate transverse electric fields ("drift fields") which steer the charges caused by the absorption of the ionising X-rays toward a very small collecting electrode (anode) in the centre (see Figure 2.11 [142]). The unique property of SDD is that, due to its small size, the collecting anode

has a extremely low capacitance, independent of the active area. The system noise is then effectively lowered, the energy resolution is improved and the amplifier time constant can be reduced while the active area can be very large to increase count rates [143]. SDD can be operated with a simple thermo-electric cooling system (Peltier cooling) without needing the low temperature of liquid nitrogen as in traditional EDX detectors.

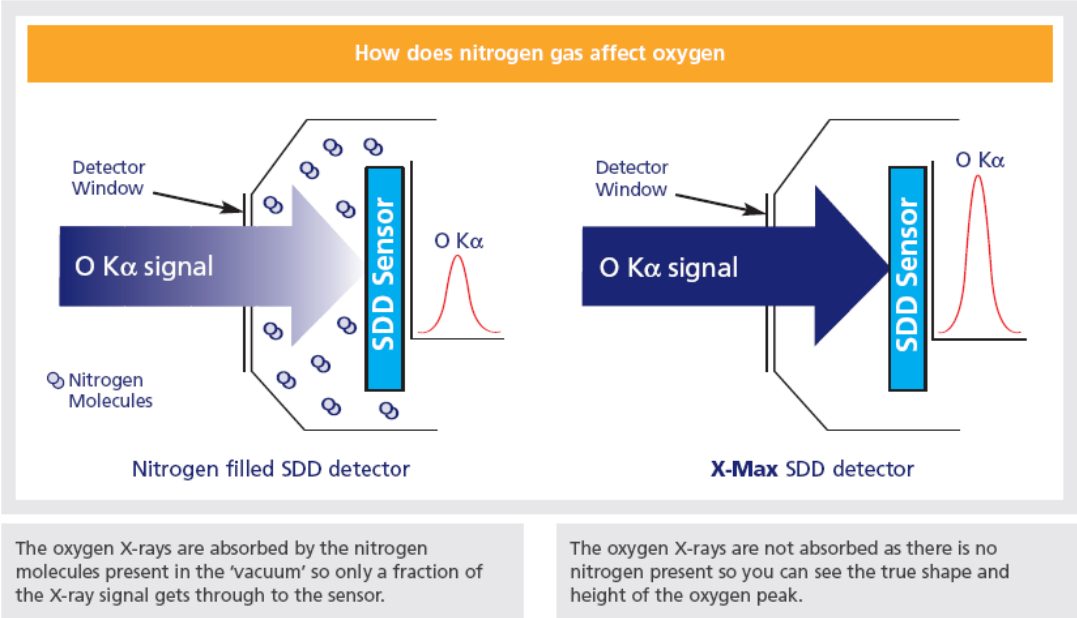


**Figure 2.10.** A demonstration of oxygen detection in an SDD with and without nitrogen gas [144].

An *Oxford Instruments* X-Max SDD [144] was used to perform EDX element mapping and line-scanning for the bimetallic nanoparticles in HAADF-STEM mode. This SDD has a large active area of 80 $mm^2$ with the count rate being increased up to higher than 500,000 counts per second. X-Max SDD is operated at a temperature range of $10^oC$ – $30^oC$, controlled by a Peltier cooling system. The absence of nitrogen gas in the cooling system of X-Max SDD brings in an improvement in oxygen detection because nitrogen gas can absorb oxygen and other low energy X-rays. Figure 2.12 shows the oxygen detection in an SDD with and without nitrogen gas [144].

## 2.3.5. Surface plasmon EELS

Electron energy loss spectroscopy (EELS) has been developed and combined with TEM as a widely-used technique for characterizing the chemical composition and electronic structure of materials. The physics of EELS is the physics of inelastic interactions between the accelerated electrons and the specimen material. These inelastic interactions include plasmon excitations, phonon excitations, inter and intra band transitions, inner shell ionizations, and Čerenkov radiation, which essentially make the electrons lose certain amounts of kinetic energy when they pass through the specimen [145, 146].

The system for EELS is set up below the image-viewing chamber of TEM. After being transmitted through the specimen, electrons are allowed to enter the EELS spectrometer, passing through an entrance aperture (Figure 2.13 [146]) having a diameter typically between 1 mm and 5 mm. The purpose of the spectrometer entrance aperture is to limit the range of entrance angles. The most important component in an EELS system is the *magnetic prism*. The magnetic prism supports a uniform magnetic field $B$ (of the order of 0.01 T) generated by an electromagnet with carefully shaped polepieces (Figure 2.13 [146]). The Lorentz force induced by this magnetic field makes electrons follow circular paths of radius $R = mv/(|e|B)$ where $v$, e, and $m$ are electron velocity, charge, and its relativistic mass, respectively. When passing through the magnetic prism, the electron beam is deflected by an angle of typically $90^{o}$. Electrons of different velocities (different kinetic energies) follow circular paths of different radii and hence they are energetically dispersed. The magnetic prism also has a focusing function that makes electrons of a given energy, originating from a point object, return to a single image point.

The dispersion spectrum of the electrons is recorded either by a *serial-recording* system or a *parallel-recording* system [146]. In our work, a parallel-recording system is used

(parallel EELS or PEELS), in which an electron lens projects an extended range of the energy-loss spectrum onto a fluorescent screen, coupled to a CCD (charge-coupled device) camera whose output signals are transferred to a data-recording computer. In PEELS, spectral peaks have extended tails due to light scattering in the fluorescent screen. These tails, however, can be removed by deconvolution procedures or minimized by using high spectral energy dispersions.

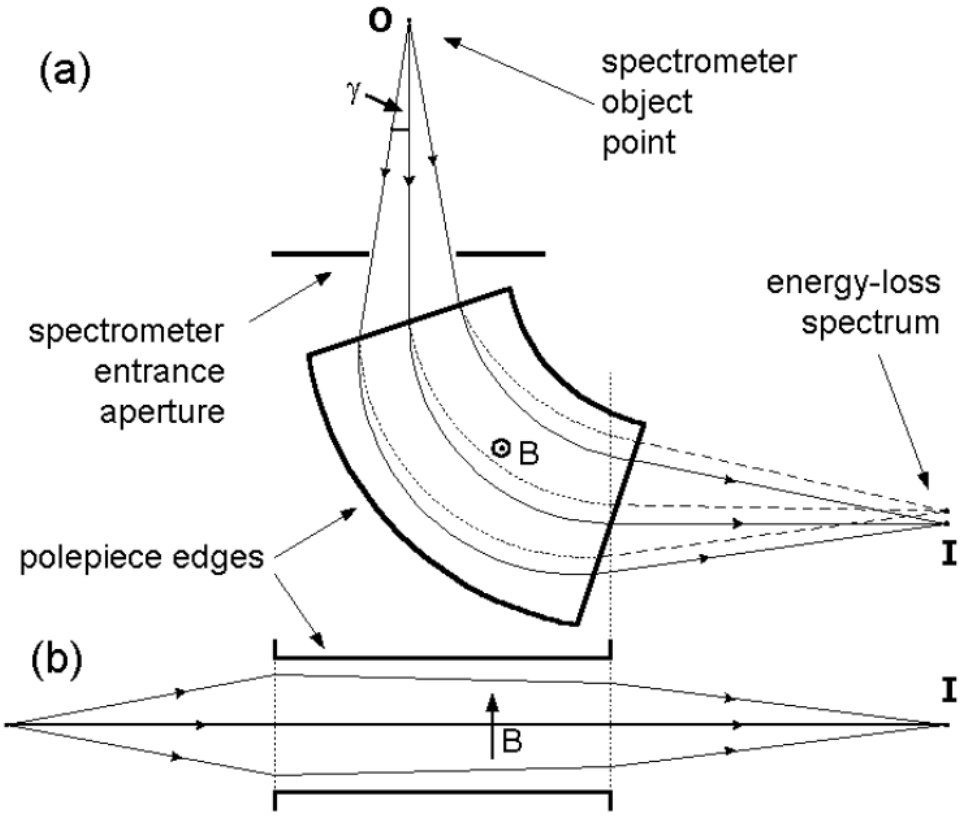


**Figure 2.11.** Dispersing and focusing function of a magnetic prism: **(a)** in a plane perpendicular to the magnetic field and **(b)** in a plane parallel to the field. Solid lines represent electrons transmitted through the specimen without energy loss; dashed lines represent electrons with energy loss [146].

An EELS spectrum can exhibit different features over different ranges of energy loss [147]. The major contribution to the detected intensity is an intense and narrow peak at an energy loss of zero (*zero-loss peak*), corresponding to electrons transmitted through the

specimen without measurable inelastic scattering. There are two predominating types of inelastic scattering causing a complex spectrum: plasmon excitations in the range 1 - 40 eV and core-loss excitations at of higher energy losses.

Plasmon excitations include *bulk plasmons* occurring in a typical range of 10-40 eV and *surface plasmons* in a typical range of 1-5 eV. In our work, the *surface plasmon resonances* (SPRs) of the bimetallic nanoparticles are investigated and so we describe briefly their nature below.

SPRs of nanoparticles relate intimately to their optical characteristics. They are collective electron charge oscillations occurring in the interface between two media of different dielectric constants (i.e., between the nanoparticle surfaces and the embedding medium). Generally, light is the most common excitation source for SPRs. In EELS, however, SPRs of nanoparticles are caused by fast electrons. Calculation of the SPRs of metallic spherical particles can be based on Mie's theory of light scattering [4]. Plasmonic oscillations can be quantized as quasiparticles having energies proportional to frequency $\omega$: $E = \hbar\omega$ ($\hbar$ is Planck's constant). In the Drude model [148], the SPR energy $E_s(l)$ for a spherical particle in vacuum is[149]:

$$E_s(l) = \frac{E_p}{\sqrt{\frac{2l+1}{l}}} \quad , \tag{2.48}$$

where $l$ is the angular quantum number ($l = 1, 2, 3\ldots$), $E_p = \hbar\omega_p = \hbar(ne^2/m\varepsilon_o)^{1/2}$ is the bulk plasmon energy ($\varepsilon_o$ is the dielectric constant of vacuum; $n$ is electron density; $e$ and $m$ are electron charge and mass, respectively). Each value of $l$ corresponds to an SPR mode and the mean SPR energy can be calculated as [149]:

$$\overline{E}_s = \frac{\sum_{l=1}^{\infty} E_l Q_l}{\sum_{l=1}^{\infty} Q_l} \quad . \tag{2.49}$$

where $Q_l$ is the excitation probability for mode $l$.

Nanoparticle SPRs are known to be size and shape dependent. For example, when the size of Au particles increases, their SPR energies decrease, corresponding to red shifts in the SPR frequencies [19,150]. The shape of a particle affects both its SPR energy and SPR peak width. Shapes with fewer faces and sharper vertices exhibit SPRs in a wider range of frequencies [151]. A non-spherical nanoparticle can have different SPRs corresponding to its different local structures. The variation of SPRs with respect to the local morphologies of a single nanoparticle can be studied using EELS in STEM mode with a very fine electron probe [152-154].

In our work, HAADF-STEM EELS was used to investigate the local morphology dependence of SPRs for bimetallic Cu-Au (Chapter 4) and Pd-Au nanoparticles (Chapter 5).

# CHAPTER 3. THEORETICAL STUDY OF 38-ATOM COPPER-GOLD CLUSTERS

**Abstract.** In this chapter, a theoretical study of 38-atom Cu-Au clusters using the combined EP-DFT approach [84] is reported. Structural distributions and energy landscapes, including calculations of electronic energy gaps for all compositions of $Cu_{38-n}Au_n$, are investigated. The energy competition between different structural motifs and different configurations are studied at the DFT level. The analysis of mixing and segregation effects results in confirmation of the preference for $Cu_{core}$-$Au_{shell}$ configurations at the DFT level. Charge transfer is calculated for different structural motifs of $Cu_{19}Au_{19}$ to study the role of this phenomenon in driving cluster configuration. (The content of this chapter has been published: Dung T Tran and Roy L Johnston, 2009, *Theoretical study of $Cu_{38-n}Au_n$ clusters using a combined empirical potential–density functional approach, Phys. Chem. Chem. Phys*., **11**, 10340).

## 3.1. Literature review

There have been a number of theoretical studies of the structures and energy landscapes of large and medium-sized Cu-Au clusters. Clusters of 456, 786 and 959 atoms have been studied using MC simulations [155]. The GA [56] search method, combined with the empirical Gupta many body potential, has also been used to investigate structural motifs, energetic landscapes and mixing and segregation tendencies of Cu-Au clusters having from a few tens to a few hundreds of atoms [156-162]. Nevertheless, for smaller clusters, where

quantum effects are more significant, empirical potentials (e.g., the Gupta potential) are insufficiently accurate [70,157]. Therefore, more accurate DFT calculations, including details of electronic structure, are needed. DFT reminimization of structures obtained from a Gupta-MC search for Cu-Au clusters of 40 atoms [163] and from a Gupta-GA search for $(Cu\text{-}Au)_N$ clusters (with N = 5-22) [164] have been carried out.

Four structural motifs were found in the study of 40-atom Cu-Au clusters by Barcaro et al. [163]: fcc-truncated octahedron (TO), capped decahedron, and two polyicosahedral (pIh) motifs (capped 5-fold pancake and capped 6-fold pancake). The competition between these motifs arises because 38 is the structural magic number for a complete TO while icosahedral (Ih) and decahedral structures are often found for clusters of a few tens of atoms [70, 157-159]. In the work of Hsu and Lai [161], using empirical many-body Gupta potentials, and the integration of a GA with a MC-based basin hopping algorithm, TO is found as the predominant structure for Cu-rich compositions of 38-atom Cu-Au clusters. Identical results have subsequently been found, for this system, by Wu et al., using a modified adaptive immune optimisation algorithm [162]. However, the presence of polyicosahedral and other structures as the global minima for Au-rich compositions suggests that there is a quite complicated competition between different structural motifs for clusters of the TO magic number. At the level of empirical potentials, the accuracy may not be sufficient to adequately reproduce the possible small differences in energy between different motifs, or between homotops. In a study by Rodrigues et al. [165], 38-atom Cu-Au clusters were also studied using a GA and the Gupta potential. Several $Cu_nAu_{38-n}$ compositions (n = 3, 6, 13, 15, 18, 37) were analyzed using DFT calculations but the structural competition at the DFT level was not discussed.

In this chapter, we describe a detailed EP-DFT study of 38-atom Cu-Au clusters, combining empirical level (Gupta potential) and high accuracy first principles (DFT) calculations. Energetic stabilities, structural distributions, TO/Ih competition, HOMO-LUMO energy gaps and charge-transfer phenomena are investigate

## 3.2. Computational details

The BCGA is used to search for the global minimum (lowest energy) and other low energy local minima (metastable isomers) at the Gupta EP level. The inputs for the BCGA program have been described in Chapter 2 (see 2.1.2). The Gupta parameters for the different types of bonding: Cu-Cu, Au-Au and Cu-Au were derived by Cleri and Rosato, which are listed in Table 3.1 [69].

**Table 3.1.** Gupta potential parameters for Cu-Au nanoclusters [69].

| Parameter | Cu-Cu | Cu-Au | Au-Au |
|---|---|---|---|
| A (eV) | 0.0855 | 0.1539 | 0.2061 |
| p | 10.960 | 11.050 | 10.229 |
| $r_0$ (Å) | 2.556 | 2.556 | 2.884 |
| $\zeta$ (eV) | 1.2240 | 1.5605 | 1.7900 |
| q | 2.2780 | 3.0475 | 4.0360 |

The structures of low energy Cu-Au clusters, at the EP level, found by the BCGA search, are subsequently further investigated by density functional theory (DFT) calculations. At the DFT level, the structures are subject to reoptimisation (local energy minimisation). In this work, the NWCHEM 5.1 quantum chemistry package [166] has been used to perform DFT calculations, with the Perdew-Wang PW91 exchange-correlation functional [167]. The basis sets adopted for Au are: spherical Gaussian-type-orbital basis sets of double-zeta valence quality [168] (7s5p5d)/[6s3p2d] with effective core potentials [169]; charge density fitting

for calculation of the Coulomb potential [170] (9s4p4d3f4g)/[8s4p3d3f2g]. For Cu, split valence basis sets [171, 172] (14s9p5d)/[5s3p2d], and Stevens-Krauss effective core potentials [173] with charge density fitting [174,175] (17s4p4d3f4g)/[7s4p2d3f2g] are used. Dealing with transition metal-containing systems like Cu-Au, a Gaussian-smearing technique for the fractional occupation of the energy levels (with a broadening factor of 0.136 eV) is applied to tackle the degeneracy problems [176-178]. The calculations were performed on the University of Birmingham's BlueBEAR high performance computer [179].

## 3.3. Results and discussion

### 3.3.1. Structural distribution and energy landscape at the EP level.

A range of different structures (putative global minima) are found by the Gupta-GA search for $Cu_{38-n}Au_n$ clusters for different compositions (see Figure 3.1). TO motifs predominate, being found for compositions n = 0-20 and 38. Icosahedral-based motifs (n = 21-34) are classified into incomplete Mackay icosahedra of type 1 or type 2 (inc-Ih-Mackay_1/2) [180] for n = 21-25 and 6-fold pancake-like polyicosahedra (pIh6) [70] for n = 26-34. The compositions n = 35-37 are found to have poorly-defined shapes: they are actually strongly distorted inc-Ih-Mackay or amorphous-like structures of low symmetry (LS) having at most a mirror plane of symmetry. The amorphous nature of these Au-rich nanoalloys is consistent with previous studies of Au and Pt clusters, with these elements being characterised by short-ranged "sticky" interatomic potentials [181,182]. It is also known that the relative stabilities of amorphous and TO structures for $Au_{38}$ are sensitive to the Gupta parameter set adopted [157, 183].

The structures and energies of our putative Gupta potential global minima (GM) are in agreement with the results of the previous studies by Hsu and Lai [161] and Wu et al. [162].

The structural distribution and calculated excess energies are shown in Figure 3.1 and our structural motifs are presented in Figure 3.2. At the Gupta level, in the Au-rich region, the TO is only found for $Au_{38}$, which is consistent with the stability of fcc structures for homogeneous (monometallic) systems.

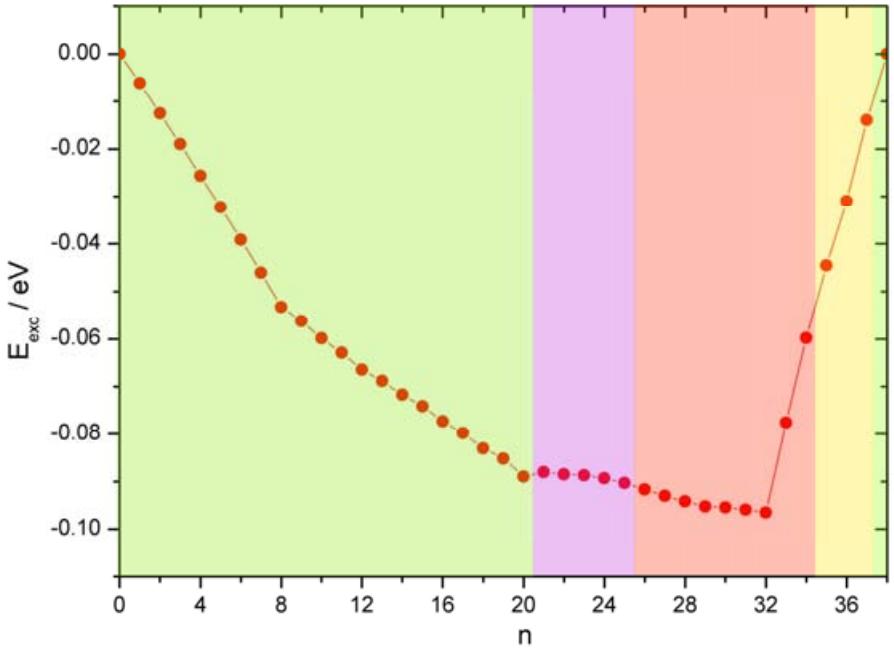


**Figure 3.1**. Structural distribution and excess energy for $Cu_{38-n}Au_n$ clusters at the Gupta level. Green region (*n = 0-20, 38*) truncated octahedral (TO); purple region (*n = 21-25*) incomplete-Mackay icosahedra (inc-Ih-Mackay); pink region (*n = 25-34*) 6 –fold pancake-like polyicosahedra (pIh6); yellow region (*n = 35-37*) amorphous-like and low-symmetry (LS) structures.

It is reasonable that pIh structures are more likely to be found in binary than in homogeneous clusters [163]. However, in the Cu-rich region, there is a stronger fcc-packing tendency and TO motifs are retained upon Au doping until n = 20. The substituting Au atoms prefer to occupy the central sites of the hexagonal (111) facets. According to Hsu and Lai, the larger Au atoms favour the surface centroids in order to make the heterogeneous system more symmetrical. Our explanation, however, is based on the mixing tendency and the correlation between the excess energies and the structural arrangements which was not

mentioned in Hsu and Lai's work. Because the larger size and the lower surface energy of Au atoms prevent them from occupying the inner core of a TO, Au atoms occupy the centres of (111) facets to maximize the number of Cu-Au bonds, and, thus, increase the exothermic mixing. After all 8 hexagonal facets of a TO are occupied by Au atoms, additional Au atoms occupy the remaining surface sites – i.e. the common atomic sites between (111) and (100) facets. Figure 3.1 shows a discontinuity in the excess energy, a factor measuring the mixing stability. The excess energy curve steps upwards at n = 8, indicating maximisation of the mixing when all the 8 (111) centroid sites of the TO are completely occupied by Au atoms.

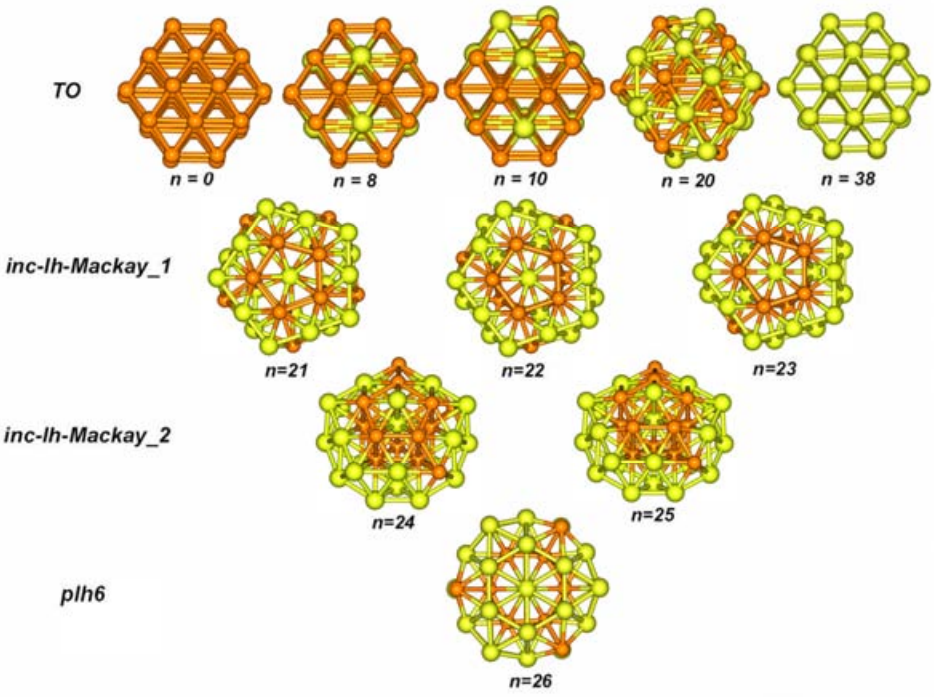


**Figure 3.2.** Structural motifs for $Cu_{38-n}Au_n$ clusters at the Gupta level. Cu and Au atoms are shown in orange and yellow, respectively.

The TO begins to be distorted when the number of Au atoms is larger than 8 (see the comparison between n = 8 and n = 10 in Figure 3.2). The TO motif, however, is retained with a regular central octahedron of 6 Cu atoms, establishing a $Cu_{core}Au_{shell}$ configuration, such that mixing occurs only on the cluster surface. Icosahedra-based motifs do not have

such complete core-shell establishment governed by geometrical symmetry (Figure 3.2). Mixing tends to occur in the core regions of inc-Ih-Mackay_1 and especially the inc-Ih-Mackay_2 structure. Unlike TO motifs, which are more geometrically isotropic, inc-Ih-Mackay clusters (which are actually large fragments of a complete 55-atom Mackay icosahedron) can have Au atoms in their core sites.

### 3.3.2. DFT calculations for EP global minima

As the balance of the factors favouring segregation (the mismatch in size and surface energies between Cu and Au atoms) and mixing (the difference in electronegativity between Au and Cu atoms) can not be described fully at the Gupta level, the Gupta-GA (putative) GM for the $Cu_{38-n}Au_n$ clusters have been reoptimized at the DFT level: the HOMO-LUMO gaps are presented in Figure 3.3. The second energy differences at the Gupta level, which are also shown in Figure 3.3, again agree completely with Hsu and Lai's work [161]. In agreement with the behaviour of the excess energies (Figure 3.1), compositions n = 8, 20 and (especially) 32 are singled out as being stable relative to neighbouring compositions and a correlation is observed between the DFT HOMO-LUMO gaps and the Gupta second energy differences, indicating a possible relationship between electronic properties and compositional ordering. In the work on 40-atom Cu-Au clusters by Barcaro et al. [163], the authors interpreted the large HOMO-LUMO gaps of capped 5-fold pancake polyicosahedral (c-pc5) structures in terms of a jellium-like electronic shell closure effect (as found by Ferrando et al. for 34-atom Cu-Au clusters [70]). Capped decahedral (c-Dh, quite similar to inc-Ih-Mackay), capped 6-fold pancake (c-pc6) and capped TO motifs were found to have small gaps. In our present work on 38-atom clusters, the pIh6 structures which are actually 6-

fold pancakes without the 2 extra capping atoms, have relatively large HOMO-LUMO gaps for the compositions n = 28-32.

The TO structures for the compositions n = 8 and 20 also have large gaps. With 8 Au atoms distributed regularly on the eight (111) facets, $Cu_{30}Au_8$ has high point group symmetry ($O_h$), though the Au atoms are displaced out of the (111) centroids (see below), which may explain the large gap. $Cu_{18}Au_{20}$, however, is a surface-reconstructed TO with rhombic $Cu_2Au_2$ facets (Figure 3.4). This agrees with the $Cu_{18}Au_{20}$ DFT structure previously presented by Rodrigues et al. [165]. The value of 0.775 eV calculated for the HOMO-LUMO gap of $Cu_{18}Au_{20}$ is comparable with the large gaps calculated for 40-atom Cu-Au clusters [163] and is larger than those previously calculated for Au-rich polyicosahedral 38-atom Cu-Au clusters [70].

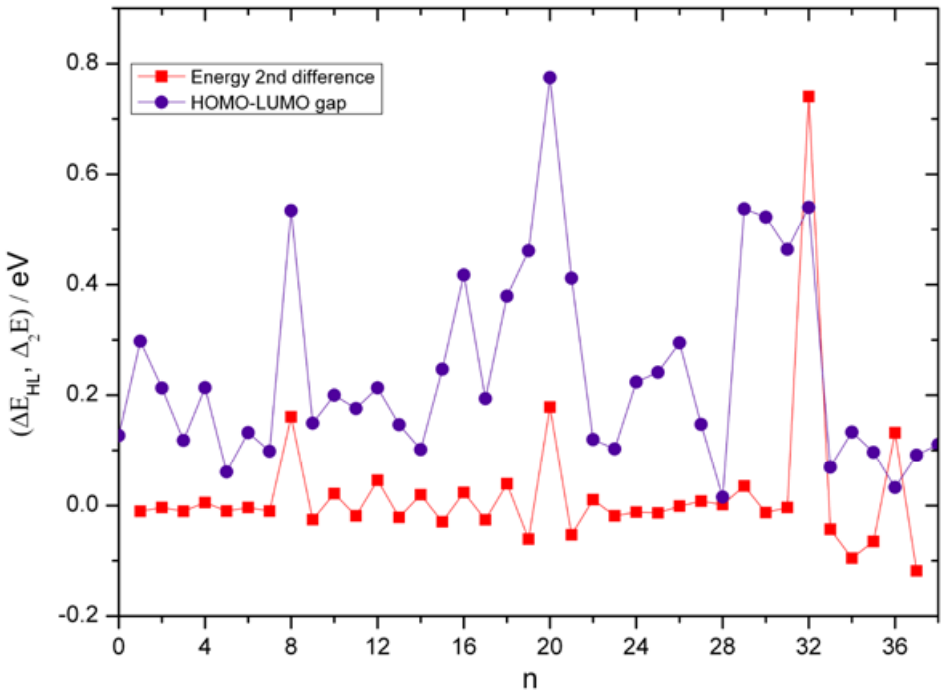


**Figure 3.3.** HOMO-LUMO electronic energy gaps ($\Delta E_{HL}$) calculated at the DFT level for the (putative) Gupta-GA global minima of $Cu_{38-n}Au_n$ (purple circles) and the second differences of binding energy ($\Delta_2 E$) at the Gupta level (red squares).

Figure 3.5 shows that at the DFT level the Cu-Au bonds expand, leading to the centroid Au atoms being displaced outwards from the centre of the (111) facets and distorting the TO. This phenomenon promotes segregation and establishes a clear Cu(core)-Au(shell) tendency for TO motifs. The expansion of Cu-Au clusters on going from the Gupta potential to DFT calculations has previously been noted by Rodrigues et al. [165]. The protrusion of atoms of "sticky" elements, such as Au or Pt, from fcc (111) facets has previously been explained in terms of directionality effects in the interatomic bonding [70,178,184].

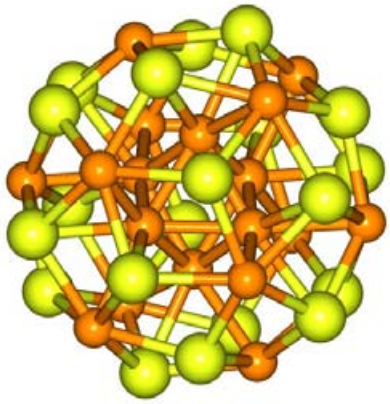

**Figure 3.4.** The $Cu_{18}Au_{20}$ TO is strongly distorted after DFT reoptimization. The square (100) and hexagonal (111) facets of a regular TO are converted to rhombic facets. This cluster has a particularly large HOMO-LUMO gap (0.775 eV).

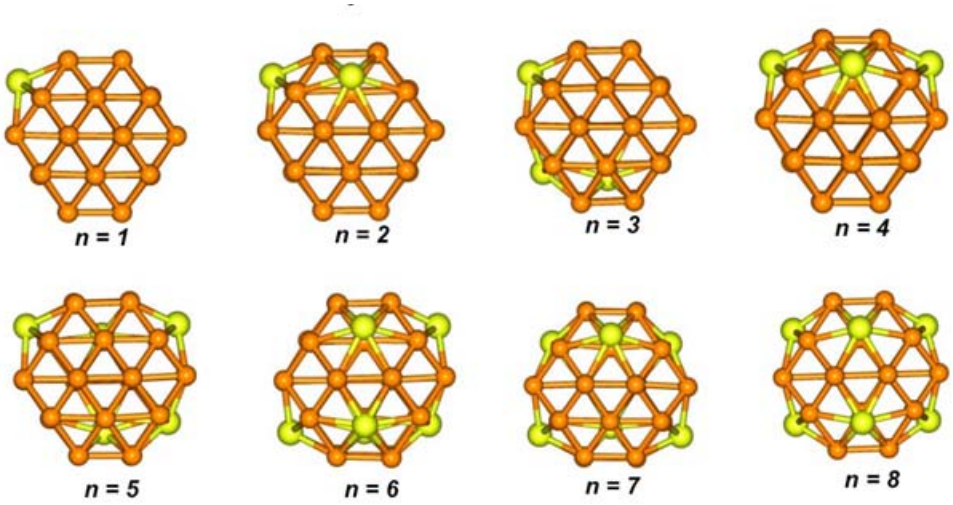


**Figure 3.5.** At the DFT level, the Cu-Au bond lengths are increased, resulting in distortions on the TO surface, where Au atoms are displaced out of the hexagonal (111) facets.

### 3.3.3. Structural competition at the DFT level

At the Gupta level, the TO structure predominates for Cu-rich compositions. However, as mentioned above, the structural competition needs to be tested at the higher level of theory. Therefore, all the Gupta global minima and other low energy isomers were reoptimized at the DFT level. For the compositions n = 0-25, there is a structural competition between the TO and inc-Ih-Mackay motifs, which are commonly found as low-lying isomers for Cu-rich compositions. The differences in the DFT energies of these two motifs are plotted in Figure 3.6. The putative DFT global minima are TO for compositions n = 0-8 and n = 22-25, while inc-Ih-Mackay are the lowest-lying isomers for compositions n = 22-25. For the compositions n = 4, 7, 8, 13, 22, 23, and 25, the energy differences between these two motifs are very small, especially for n = 13.

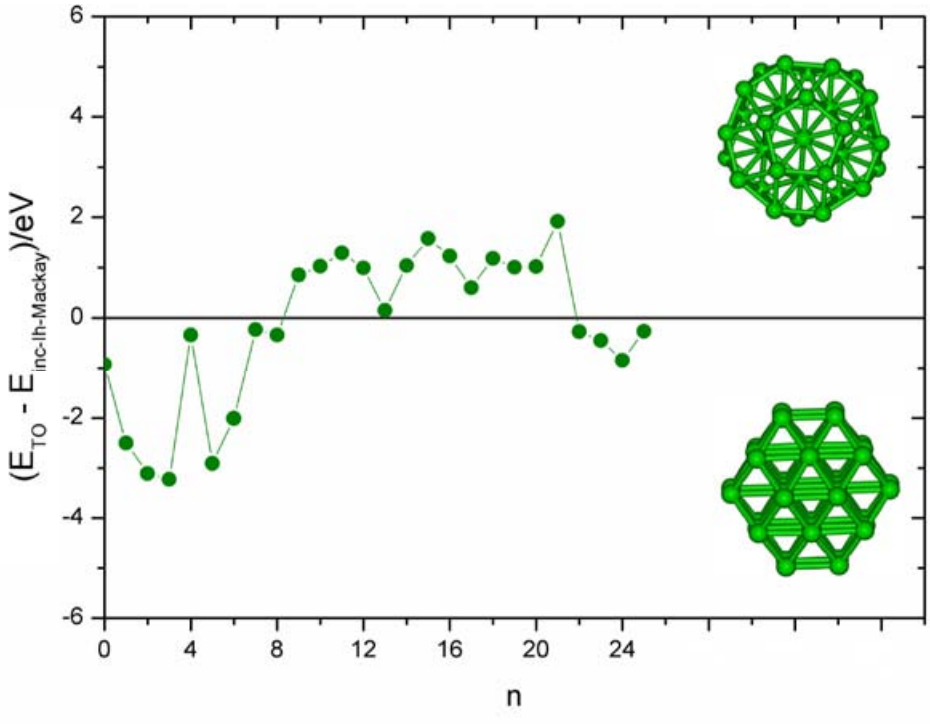


**Figure 3.6.** Energy comparison between the TO and the inc-Ih-Mackay structures of $Cu_{38-n}Au_n$ (n = 0-25) at the DFT level. If a point lies below zero, the TO is the DFT GM for the corresponding composition, otherwise the inc-Ih-Mackay is the GM.

The small calculated energy difference between the TO and inc-Ih-Mackay structures for $Cu_{30}Au_8$, indicates that one must be cautious in equating a high HOMO-LUMO gap for a particular cluster structure with high stability relative to other isomers. Figure 3.6 also shows that the distorted TO structure for $Cu_{18}Au_{20}$, which was also calculated to have a large HOMO-LUMO gap, is less stable than the corresponding inc-Ih-Mackay structure.

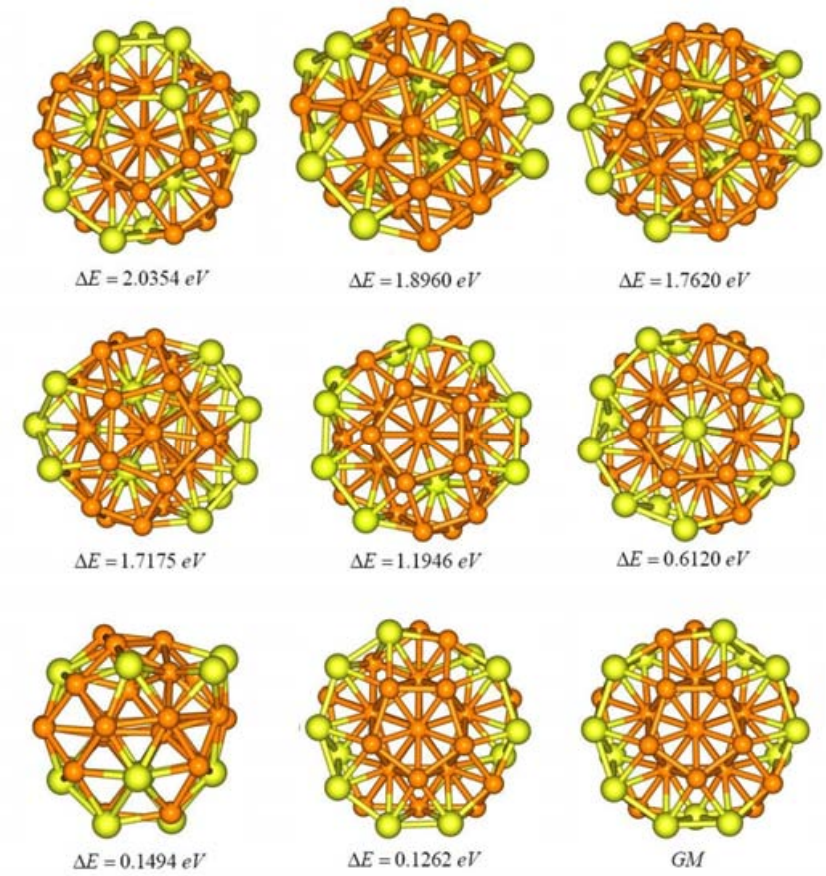


**Figure 3.7.** Comparison of the total electronic energies of the inc-Ih-Mackay homotops and the metastable TO of $Cu_{25}Au_{13}$ at the DFT level. The global minimum (GM) is an inc-Ih-Mackay_1 homotop with all the Au atoms segregated to the cluster's surface. $\Delta E$ is the energy relative to the GM: $\Delta E = E - E_{GM}$.

Details of the energy comparison between inc-Ih-Mackay homotops and TO are shown in Figure 3.7 for $Cu_{15}Au_{23}$. The number of TO homotops is found to be relatively small because of the high isotropy of the TO geometry. The chosen (putative) GM is an inc-Ih-Mackay_1, having all Au atoms segregated on the surface. The homotops which have some

Au atoms occupying the inner sites are about 2 eV higher in energy than the GM. The energy of the TO is only 0.15 eV higher than the GM. Surprisingly, the next-lowest inc-Ih-Mackay homotop lies only 0.02 eV below the TO isomer.

Energy comparisons at the DFT level confirm that there is a tendency towards core-shell segregation, preventing Au atoms from occupying the cluster core. All the (putative) DFT GMs have clear $Cu_{core}Au_{shell}$ segregation. This Cu-Au segregation is interpreted in terms of strain-relief effects, where the smaller atoms (Cu) preferentially occupy the cluster core and the element with the lower surface energy (Au) preferentially occupies the surface. However, the cohesive energy of Au (3.81 eV) is higher than that of Cu (3.49 eV) [269], which favours Au occupying the cluster core, but this effect is not strong enough to drive the configuration of the Cu-Au clusters. This DFT preference for Au surface segregation has also been discussed by Rodrigues et al. [165].

In order to investigate the effect of changing the exchange-correlation functional on the energetic ordering of homotops and structural motifs, the lowest nine isomers of $Cu_{25}Au_{13}$ obtained using the PW91 functional were geometry optimised with the $B97^{GGA}$-1 functional (a reoptimised version of the Becke97 functional [185]). As shown in Table 3.2, the energy ordering of the lowest isomers is unaffected, though one of the higher-lying homotops moves down from $9^{th}$ (PW91) to $7^{th}$ ($B97^{GGA}$-1). We are therefore confident that changing the exchange-correlation functional will have little influence on the structural motifs reported here as the GM (as a function of composition) – and on their qualitative chemical ordering. It should also be noted that hybrid exchange-correlation functionals (such as the popular B3LYP family) have been shown to be inappropriate for the study of medium sized metal clusters [70].

### 3.3.4. Structural distribution and energy landscape at the DFT level

In comparison with the scenario at the Gupta level, the structural distribution at the DFT level (see Figure 3.8) exhibits some crossovers between inc-Ih-Mackay and TO motifs in the composition range n = 9-25. The DFT excess energy curve is noisier than the Gupta curve and there is close competition between different structural motifs and different homotops at the DFT level. The TO experiences a decrease in stability for more than 8 Au atoms (in the range n = 9-21) because there are only 8 preferred (111) centroid sites on the surface of a TO. This favours the inc-Ih-Mackay in the range n = 9-21.

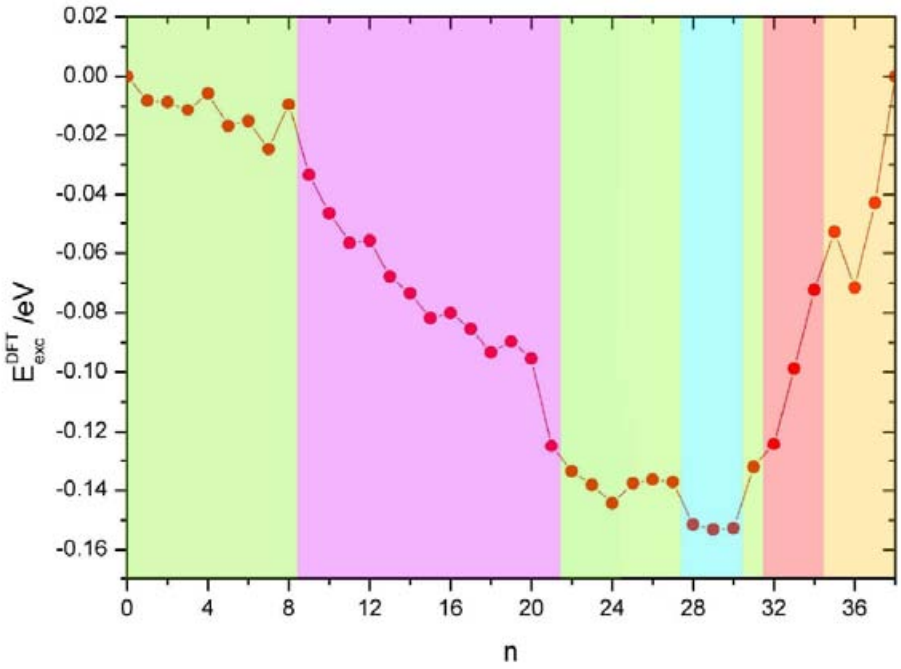


**Figure 3.8.** Structural distribution and excess energies for $Cu_{38-n}Au_n$ clusters at the DFT level. Green regions (n = 0-8, 22-27, 31) TO; purple region (n = 9-21) inc-Ih-Mackay; cyan region (n = 28-30) low symmetry pIh (type 2) (pIh-LS_2); pink region (n = 32-34) pIh6; yellow region (n = 35-38) amorphous-like and LS. The compositions n = 22-27 and n = 31 are severely deformed TOs, they are still classified as TO motifs because they maintain a regular $Cu_6$ octahedral core.

In agreement with previous DFT calculations by Garzón and co-workers [181,183] and Ferrando et al. [70], the DFT GM for $Au_{38}$ is an amorphous-like structure instead of a TO (as

at the Gupta level). The TO region is split, with some TO structures found for Au-rich compositions (n = 22-27 and n = 31). Actually, these compositions give rise to deformed TOs with no definable symmetry except some traces of reflection symmetry. However, they are still classified as TO motifs because a regular $Cu_6$ octahedron is retained as the cluster's central core (see Figure 3.9a for $Cu_{13}Au_{25}$).

We note that, in the work of Rodrigues et al. [165], only the inc-Ih-Mackay structure of $Cu_{13}Au_{25}$ (which was the putative GM at the Gupta level), was analyzed at the DFT level, while in our work (including metastable Gupta isomers in the DFT reminimisation step) indicates that the deformed TO is the GM at the DFT level for $Cu_{13}Au_{25}$.

In the DFT calculations, the pIh6 region is narrowed to n = 32-34 due to the presence of a new low-symmetry pIh motif (pIh-LS_2) [180] for compositions n = 28-30. These compositions also have the lowest excess energies, corresponding to maximized Cu-Au mixing. The pIh-LS_2 structure and its $C_s$ reflection plane of symmetry are shown in Figure 3.9b.

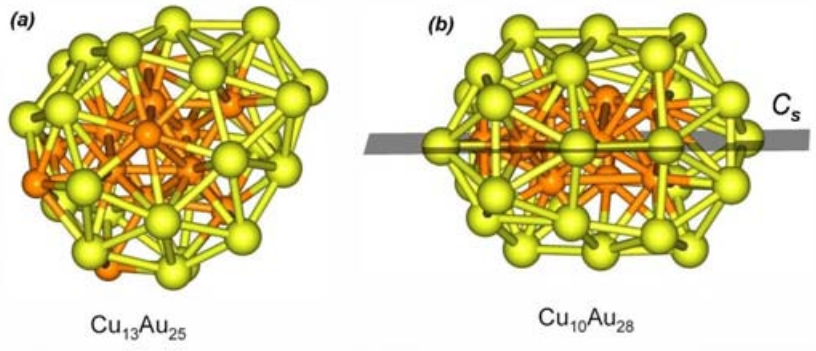


**Figure 3.9.** Two putative GM at the DFT level: **(a)** Severely deformed TO of $Cu_{13}Au_{25}$; **(b)** the pIh-LS_2 of $Cu_{10}Au_{28}$, which was not presented as a GM at the Gupta level, has a single mirror plane of symmetry.

**Table 3.2.** Comparison of relative energies of the lowest energy isomers of $Cu_{25}Au_{13}$ calculated using the PW91 and $B97^{GGA}$-1 exchange-correlation functionals.

| Isomer | $\Delta E(PW91)/eV$ | $\Delta E(B97^{GGA}-1)/eV$ |
|---|---|---|
| 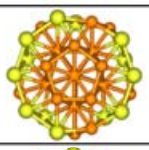 | 0.000 | 0.000 |
| 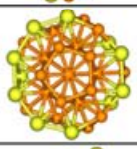 | 0.126 | 0.200 |
| 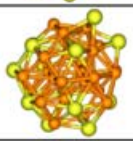 | 0.149 | 0.490 |
| 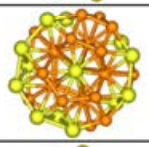 | 0.612 | 0.899 |
| 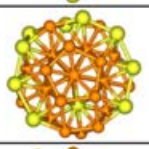 | 1.195 | 1.375 |
| 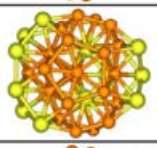 | 1.718 | 1.706 |
| 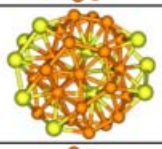 | 1.762 | 2.140 |
| 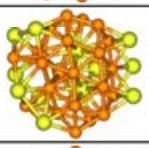 | 1.896 | 2.175 |
| 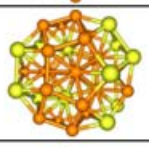 | 2.035 | 1.849 |

Although in the work on 40-atom Cu-Au clusters [163] there was found to be close competition between c-pc5 (capped pIh5) and c-pc6 (capped pIh6) motifs, the 5-fold pancake motif (pIh5) was not found as a low-lying isomer by the Gupta-GA in our present work, so this kind of structure is presumably not involved in the structural competition for

38-atoms. In a previous study of 38-atom Pd-Pt, Ag-Pt, Pd-Au and Ag-Au clusters [180], again the pIh5 structure was not found to be competitive. Our work shows a competition between deformed TO and pIh structures in the range n = 25-34. The TO becomes the GM for n = 26, 27, 31 and the remaining compositions belong to the pIh6 and pIh-LS_2 motifs. This is different from the case of 38-atom Pd-Au clusters [180], where pIh motifs were disfavoured at the DFT level and the TO was the preferred structure for both Au-rich and Au-poor compositions. A possible reason is that the Pd-Au TOs are not distorted but the Cu-Au ones are, with this deformation tendency making the TO lose out for n > 8. The distortions (surface reconstructions) found for the TO structures may be due to the size-mismatch between Cu and Au atoms (which is greater than that between Pd and Au) and should also be favoured by directionality effects (expected to be greater for Cu-Au than Pd-Au) and the "stickiness" of Au bonding, as previously discussed for pure Au clusters [184]. Finally, it is possible that the strongly distorted core-shell segregated structures shown in Figure 3.9 are related to the hybrid fcc-decahedral $Pt_{core}Pd_{shell}$ structures found to be stable at the DFT level across a wide composition range for 34-atom Pd-Pt clusters [180], though it should be noted that Pd and Pt exhibit a very small size-mismatch.

### 3.3.5. Charge transfer

The Pauling electronegativity is 2.4 for Au and 1.9 for Cu. The difference in electronegativity leads one to expect charge transfer between these two species, in which some negative charge is transferred from Cu to Au atoms. DFT optimization and Mulliken population calculations have been performed on the Cu-Au dimer, which has a net negative charge of –0.24 |e| on the Au atom (see Figure 3.10). In a previous study [186], the Mulliken

charge for the Au atom in an Ag-Au dimer was calculated as -0.22 |e| (note that Ag has the same electronegativity as Cu).

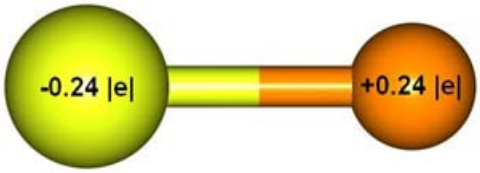


**Figure 3.10.** Charge transfer calculated at the DFT level for the Cu-Au dimer.

For nanoclusters, the charge transfer phenomenon is also the consequence of certain geometrical factors, rather than purely differences in electronegativity. For example, negative charge has been found to transfer from the central atom to the outer atoms in 13-atom icosahedral ($I_h$) and cuboctahedral ($O_h$) clusters of Ag and Au [186]. This electron transfer direction is consistent with the consideration that, when losing negative charge, an atom gets smaller and more likely to occupy central cluster sites. The combination of charge transfer induced by the geometrical structure and charge transfer induced by electronegativity differences may be an important factor driving the ordering of small binary clusters as in the case of 13-atom Ag-Au clusters [186].

Mulliken atomic charges calculated for the TO and inc-Ih-Mackay_2 motifs of $Cu_{19}Au_{19}$ are presented in Figure 3.11. The deformed TO is 1 eV higher in energy than the (putative) DFT GM (inc-Ih-Mackay_2). For the TO (Figure 3.11a), the 6 Cu atoms which form the octahedral core are positively charged. The significant amounts of negative charge transferred from the central atoms to the surface ones are consistent with the above consideration. The 6 central Cu atoms are not uniformly charged because the structure no longer has $O_h$ symmetry. It is surprising that the 19 Au atoms are not significantly involved in charge transfer. The sum of the electric charges of all Au atoms (only -0.25 |e|) suggests that there is little negative charge transferred from Cu atoms to Au atoms. Therefore, the

total charge transfer (3.43 e) can be mainly attributed to the interactions between the central and the peripheral Cu atoms.

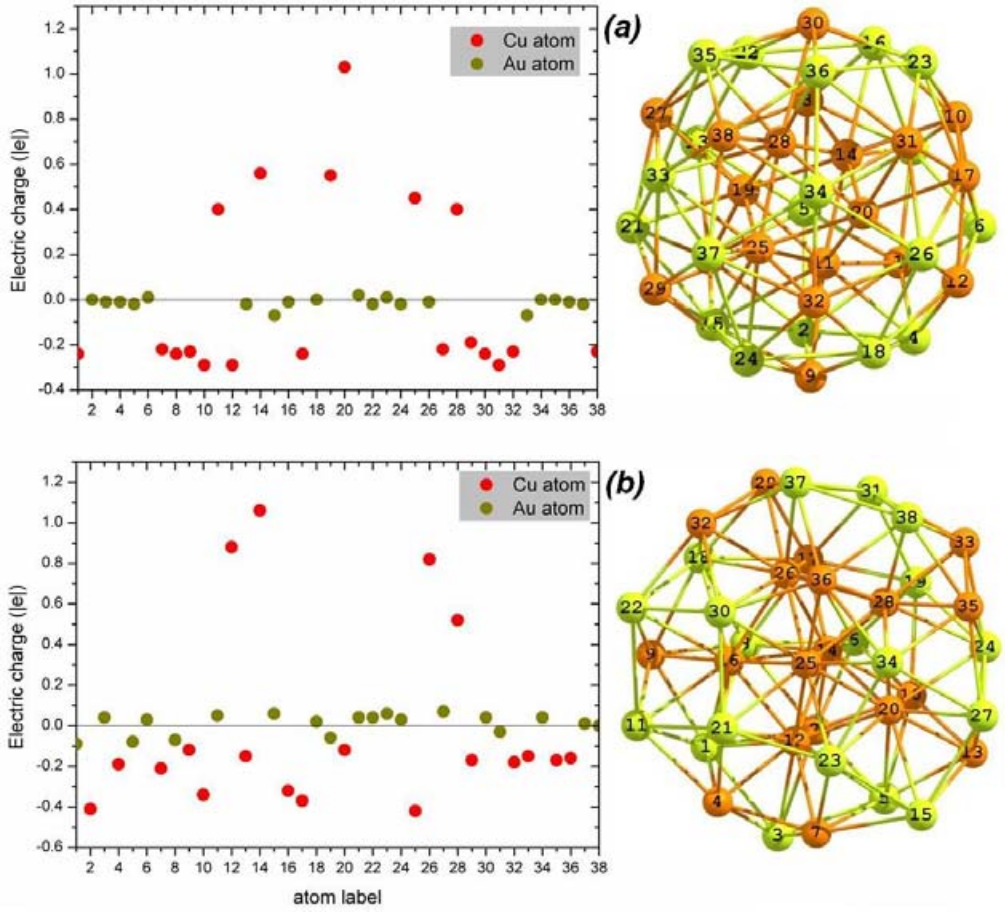


**Figure 3.11.** Charge transfer in the TO and inc-Ih-Mackay isomers of $Cu_{19}Au_{19}$: **(a)** deformed TO with total charge transfer of 3.43 e and sum of Au atomic charges of –0.25 |e|; **(b)** inc-Ih-Mackay_2 with total charge transfer of 3.48 e and sum of Au atomic charges of +0.20 |e|.

The scenario for the inc-Ih-Mackay_2 (Figure 3.11b) is not significantly different from that of the TO. This structure has a decahedral core of 7 Cu atoms, but only 4 Cu atoms (labelled 12, 14, 26, and 28) are positively charged. It is reasonable to suppose that the charge transfer behaviour of each central atom is sensitive to its atomic environment. The 7 Cu atoms do not exhibit the same behaviour because they have slightly different

environments. The positive sum of the charges on the Au atoms (+0.2 |e|) in this case is possibly due to the complex interplay between atomic environments and the geometrical structure.

The small difference in the total charge transfer between the TO (3.43 e) and the Inc-Ih-Mackay_2 (3.48 e) motifs suggests that the stabilization of the $Cu_{19}Au_{19}$ cluster does not arise solely from the maximization of charge transfer. Au atoms are nearly neutral for both TO and inc-Ih-Mackay_2 motifs, so they are not significantly involved in Coulombic interactions. Therefore, the charge transfer behaviour presented here is consistent with the segregation tendency because the neutralization (or slightly positive charging) of the Au atoms prevents them from being attracted to the cluster core. For example, in the inc-Ih-Mackay_2 structure, the distance between the 12-labelled Cu atom (with a charge of +0.88 |e|) and the 4-labelled Cu atom (with a charge of -0.19 |e|) is 2.43 Å, while the distance between the 12-labelled Cu atom and the 21-labelled Au atom (with a charge of +0.04 |e|) is 2.88 Å (for reference, the bond length of the Cu-Au dimer is 2.38 Å).

## 3.4. Conclusions

Using an EP/DF approach, we have performed a theoretical study of 38-atom Cu-Au clusters. We have presented the structural distributions and energetic landscapes at both Gupta (EP) and DFT levels. We have also studied the energy competition between different structural motifs and homotops, the predominance of segregation effects, and charge transfer phenomena and have found:

At the level of the EP (Gupta potential), our results agree with those of Hsu and Lai [161] using an alternative search method. The structural motifs found are: TO, inc-Ih-Mackay, pIh6 and amorphous-like structures. The TO motifs, including distorted TOs (n > 8)

predominate for Cu-rich compositions. Au atoms preferentially occupy the centroids of the hexagonal (111) facets on the TO surface. While the core-shell segregation behaviour is clear for TO structures, mixing in the cluster core regions is observed for inc-Ih-Mackay structures.

The HOMO-LUMO energy gaps calculated after DFT reoptimization of the Gupta GMs correlate with the Gupta energy second differences, with the compositions (n = 8, 20 and 32), having the largest HOMO-LUMO gaps. Investigation of alternative structural motifs, however, has shown that a high HOMO-LUMO gap for a particular cluster does not necessarily imply that it is the most stable isomer at the DFT level.

The distribution of structures, as a function of composition, changes significantly on going from the EP (Gupta) to the DFT level. There are crossovers between TO and inc-Ih-Mackay domains in the range n = 9-25. TO motifs are less favoured at the DFT level, possibly because they are severely deformed, apart from the regular $Cu_6$ octahedron which is still maintained as the cluster core. The reduction of the pIh6 domain is accompanied by the appearance of the pIh-LS_2 structure. This low-symmetry structure has a $C_s$ mirror plane and the compositions n = 28-30 have the lowest excess energies.

DFT calculations indicate a clear $Cu_{core}Au_{shell}$ segregation tendency for all compositions of $Cu_{38-n}Au_n$. Our results confirm the results for some sampled compositions in the previous work by Rodrigues et al [165]. For the Cu-rich TO structures with n = 1-8, core-shell segregation is promoted by the Au atoms in the hexagonal (111) centroids being pushed outwards due to the increased Cu-Au bond lengths (which has also been mentioned by Rodrigues et al.). The energy comparison of low-lying isomers of $Cu_{25}Au_{13}$ indicates that homotops having Au atoms on the cluster surface are strongly favoured at the DFT level.

Charge transfer is a complex phenomenon for 38-atom Cu-Au clusters. It appears that the geometrical structure of the cluster and individual atomic environments are the most important factors governing charge transfer. Indeed, the directional transfer of negative charge from Cu to Au atoms (due to the higher electronegativity of Au atoms) is neutralized in $Cu_{19}Au_{19}$ clusters. Although the nearly neutral Au atoms may be consistent with the segregation tendency, because of their non-attraction to the cluster core, we cannot conclude that the maximization of charge transfer is the driving force that lowers the cluster energy.

# CHAPTER 4. CHEMICALLY-SYNTHESIZED COPPER-GOLD NANOPARTICLES

**Abstract.** Dodecanethiol-capped Cu-Au nanoparticles, synthesized via a successive two-phase (water/toluene) and galvanic-exchange procedure, were characterized using TEM techniques. Electron-induced morphological evolution was observed under HRTEM. Cuboctahedral morphology was found to be thermodynamically stable. Electron-induced aggregation of two particles was also observed. Chemical ordering of cuboctahedral particles was studied by atomic-resolution HAADF-STEM imaging and SDD-EDX elemental mapping. The particles were found to be Cu-Au mixed, and to be stable in air. SPR, which is dependent on local structure, was investigated by EELS in STEM mode. (A part of this chapter has been published: Dung T Tran, Ian P Jones, Roy L Johnston, Jon A Preece, and Coenraad R van den Brom, 2010, *Truncated-octahedral copper-gold nanoparticles*, *J. Phys.: Conf. Ser.*, **241**, 012086).

## 4.1. Literature review

Bimetallic copper-gold nanoparticles are promising novel catalysts [187]. This consideration is based on the fact that monometallic copper nanoparticles are known for example to catalyse the oxidation of alcohols to aldehydes [188], and monometallic gold nanoparticles are not only active homogeneous catalysts but also are commonly used for selective oxidation reactions [34, 189, 190]. In addition, in CO oxidation reactions, Cu-Au

alloy catalysts has been found to be significantly more active than monometallic Cu and Au catalysts, due to a synergistic interaction between Cu and Au [187, 191].

Various experimental studies of bimetallic Cu-Au nanoparticles have been reported [9,187, 192-206]. In agreement with the three ordered stoichiometric bulk phases: $Cu_3Au$, $CuAu_3$, and CuAu for Cu-Au alloy [29], $(Cu_3Au)_M$, $(CuAu_3)_M$, and $(CuAu)_M$ structures (M = 1, 2, 3,….), which are often fcc-like, has been found in nanoparticles made by both chemical and physical methods [192-205]. In early work by Mori et al. [192-195], mixing at room temperature between Cu and Au in $(Cu_3Au)_M$ nanoparticles prepared by dual source electron beam vaporization were observed. In other work by Pauwels et al. [199], all three stoichiometric structures, with solid-solution conformations, have been found in HRTEM measurements of Cu-Au nanoparticles produced by laser vaporization. These particles, when deposited on amorphous carbon, frequently exhibit cuboctahedral, decahedral and spherical geometries with twinned structures. However, only truncated half octahedral shapes were observed for the particles deposited on MgO substrate.

A subsequent HRTEM study on chemically synthesized Cu-Au nanoparticles, with polyvinylpyrroidone (PVP) as the stabiliser, was performed by Pal et al.[201]. Compared with the above particles formed via high-energy impacts of electron beam or laser, these particles, which were chemically synthesized at room temperature, were found to have cubic-like, truncated-octahedral, decahedral, icosahedral, and non well-defined morphologies. The authors also reported that the size and structure of the particles are sensitive to the Cu:Au ratio in the synthesis. In fact, diverse structures can be expected from Cu-Au nanoparticles made by wet-chemistry at room temperature, because more metastable structures may be formed.

Chemical synthesis of PVP-stabilized Cu-Au nanoparticles continued to be developed by Schaak et al, using either tetraethylene glycol or borohydride as the reducing agents [202-204]. The authors also reported the diffusion of Cu into Au when the particles were heated, yielding solid solutions. Beside PVP, different stabilisers have also been used by other groups to synthesize bimetallic Cu-Au particles [187]. Shon, Murray et al. have developed a procedure using galvanic exchange (GE) [14], in which bimetallic Cu-Au particles are formed by the reaction between gold thiolate complex and dodecanethiol-stabilized Cu particles prepared by the Brust-Schiffrin method [12]. Ultraviolet-visible (UV-vis) spectroscopy performed for these particles soon after synthesis found a surface plasmon resonance (SPR) peak of Au at 532 nm, indicating that the metallic Au reduced by GE initially deposit on to the surface of the Cu seeds.

Alloying has been observed for Cu-Au nanoparticles produced by physical methods in some analytical HRTEM studies [199,201,206]. For Cu-Au particles prepared by wet-chemical methods, however, studies of structural properties and chemical ordering using HRTEM and TEM-based techniques, have not been reported. These studies are needed, because understanding of structure stability and element distribution is important for directing applications of Cu-Au nanoparticles.

In this chapter, we report characterizations using (HR)TEM and STEM-nanoanalysis for Cu-Au nanoparticles which are chemically prepared following an adapted Shon-Murray's procedure [14] in which the particles were prepared under an ambient nitrogen atmosphere to minimize oxidation of Cu. We observed the size-distribution, crystallinity, morphology, structural stability, as well as structural evolution and aggregation of the particles under the electron beam. We performed SDD-EDX elemental mapping to reveal the Cu and Au distribution inside a single particle. To relate to previous UV-vis studies of chemically-

synthesized Cu-Au particles, we carried out STEM low-loss EELS with electron beam positioning to measure localized SPRs, investigating the dependence of SPR on local structure and composition.

## 4.2. Experimental details

Dodecanethiol-stabilized Cu-Au nanoparticles were synthesized with a two-stage reduction [36]. The first stage is preparation of dodecanethiol Cu particles, following a two-phase (water/toluene) Brust-Schiffrin method [37]; the second stage is GE reaction between Cu and Au in 4-tert-butylbenzyl thiolate gold solution. To a purple solution of $Cu(ClO_4)_2.6H_2O$ (371 mg, 1 mmol) and tetraoctylammonium bromide (484 mg, 0.9 mmol) in toluene (35 ml) was added dodecanethiol (0.48 ml, 2 mmol). The resulting colourless solution was vacuum degassed, followed by an addition, under $N_2$, of $NaBH_4$ (378 mg, 10 mmol) in degassed water (15 ml) affording a brown dispersion. The dispersion was stirred for 1 hr and the toluene phase was separated and reduced (~10 ml) in vacuo (~ 35$^o$C). To this dispersion was added ethanol (~ 80 ml) followed by centrifugation (3500 rpm, 15 mins). The supernatant was decanted from the dark brown slurry of nanoparticles. The nanoparticle slurry was dried in vacuo (35$^o$C) to afford a dark brown powder (35 mg) of dodecanethiol-stabilized Cu nanoparticles. A dispersion of the Cu nanoparticles (35 mg) and 4-tert-butylbenzyl thiolate gold (25 mg, ~0.066 mmol) in degassed toluene (15 ml) was stirred for 3 hrs at room temperature, followed by evaporation of the toluene in vacuo to afford a dark brown powder. The dark brown powder was dispersed in a mixture of 2-butanol, acetonitrile, and ethanol (~ 90 ml, 1:1:1) and filtered through celite. The filtrate was centrifuged (3500 rpm, 15 mins) and the supernatant was decanted off. The dark brown slurry was dried in vacuo, affording Cu-Au nanoparticles as a dark brown powder (20 mg). It is noted that all the above steps

were carried out in Schlenk flasks and centrifuge tubes, which were vacuumed or quarantined from ambient air via a constant flux of nitrogen gas.

The Cu-Au particles were exposed to ambient air and dispersed in toluene then deposited on a carbon film on a copper TEM grid. HRTEM, HAADF-STEM EDX and mapping and low-loss EELS were performed using a field emission gun Tecnai F20 microscope operating at 200 kV. In (HR)TEM mode, a high electron beam current was adopted (large condenser aperture C2 = 150 μm, extraction voltage = 4200 V); the software ImageJ [207] was used to generate the size-distribution histogram and the Fast Fourier Transforms (FFT). In HAADF-STEM mode: C2 = 30 μm; spot size = 8 was set for the C1 lens; the electron probe size was smaller than 1 nm; a short camera length L = 150 mm was chosen; the inner semi-collection angle for the HAADF detector was 40 mrad.

EDX elemental mapping in HAADF-STEM mode was performed using an X-Max SDD attached (see Chapter 2: 2.3.4) to the microscope. The collection solid angle is approximately 1.3 srad, yielding high X-ray count-rates and thus reducing the acquisition time and easing drift errors for nanoparticles. To minimize the shadowing effect [208], the specimen was tilted to 18 degrees. The INCA software was used to control the acquisition process. The *SiteLock*$^{TM}$ function of this software was used to automatically correct the drift of the particles in a limited area. However, because of the high drift rate, the particles often drift away from the limited area, making the SiteLock function stop. Our method to solve this problem is moving the sample (corresponding to the particle drift) so that the particles are continuously kept inside the limited area.

A Gatan 666 PEELS system controlled by the Gatan EL/P 3.0 software was used to perform the EELS study. The holes in the carbon film were exploited to avoid the strong bulk plasmon signal of the carbon film (with a thickness of around 20-30 nm), which

overwhelms the low-loss region. Lying at the edge of a hole, the particles are suspended so that when the STEM electron probe is positioned on them, no carbon contamination is countered. The low-loss EELS spectra were recorded by positioning the electron probe on the particles and acquiring the transmitted electrons using a spectrometer with a semi-acceptance angle of approximately 4 mrad and an energy dispersion of 0.05 eV. A short acquisition time (10 accumulations for each spectrum, 1 second for each accumulation) was set to reduce particle drift and electron beam damage.

Atomic resolution HAADF-STEM imaging of the nanoparticles was performed using the dedicated VG HB601UX FEG-STEM microscope at Daresbury Laboratory.

## 4.3. Results and discussion

### 4.3.1. (HR)TEM

A conventional TEM image and the corresponding size-distribution histogram for the Cu-Au particles are shown in Figure 4.1. Sizes vary from around 1 to 10 nm. The average diameter of the Cu-Au particles in this work is 2.9 ± 1.8 nm, consistent with those of dodecanethiol-stabilized Ag-Au and Ag-Pd particles prepared via GE, which have average diameters of 3.0 ± 1.4 nm and 3.4 ± 1.5 nm, respectively [14].

Changes in particle morphology, under exposure to the high-density electron beam, were investigated by HRTEM. Initially, indefinable shapes were predominantly observed as metastable states of the particles which were prepared chemically at room temperature. When stimulated by an adequately high energy transfer from the fast electrons, the particle morphology continuously changed until hexagons were observed as the 2D-projections of the particles. The new morphology, which is identified as a cuboctahedron (a type of truncated-octahedral morphology), remained unchanged when further irradiated by the

electron beam. Previously, it has been reported that, gold nanoparticles also can undergo structural rearrangements induced by a TEM electron beam [209]. It has also been demonstrated that, the transfer of electron beam energy, which can equivalently increase the temperature by 100-200$^{o}$C, can cause perturbations in shape and structure as well as quasi-melting phenomena for small nanoparticles [210-212]. Changes in crystalline structure have previously been reported when a Cu-Au particle of around 3 nm was irradiated with an electron beam [206].

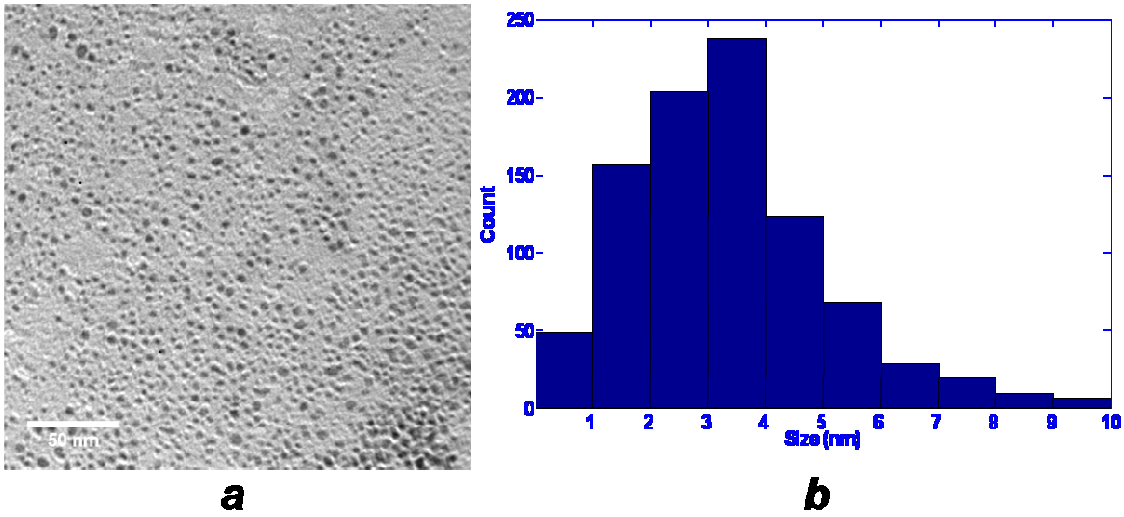


**Figure 4.1.** (a) Conventional TEM image of the Cu-Au nanoparticles and (b) the corresponding histogram of size-distribution (inset).

Thermodynamically, the cuboctahedral shape can be considered as the equilibrium state of the Cu-Au nanoparticles, adopted after morphological evolution under the electron beam. Figure 4.2a shows the HRTEM image of such a cuboctahedral Cu-Au particle (left), which has an fcc crystalline structure, and the corresponding FFT pattern (right), along the <011> direction. This equilibrium morphology, which may be affected by the interaction between the particle and the substrate [213], is consistent with the HRTEM observations for laser vaporization-synthesized Cu-Au nanoparticles deposited on amorphous carbon [199]. Figure

4.2b shows the HRTEM of a larger particle (left) and the corresponding FFT (right), also observed along the <011> direction. This particle is twinned, as a result of an aggregation between two smaller particles. The distorted cuboctahedral shape suggests that the particle is undergoing morphological evolution.

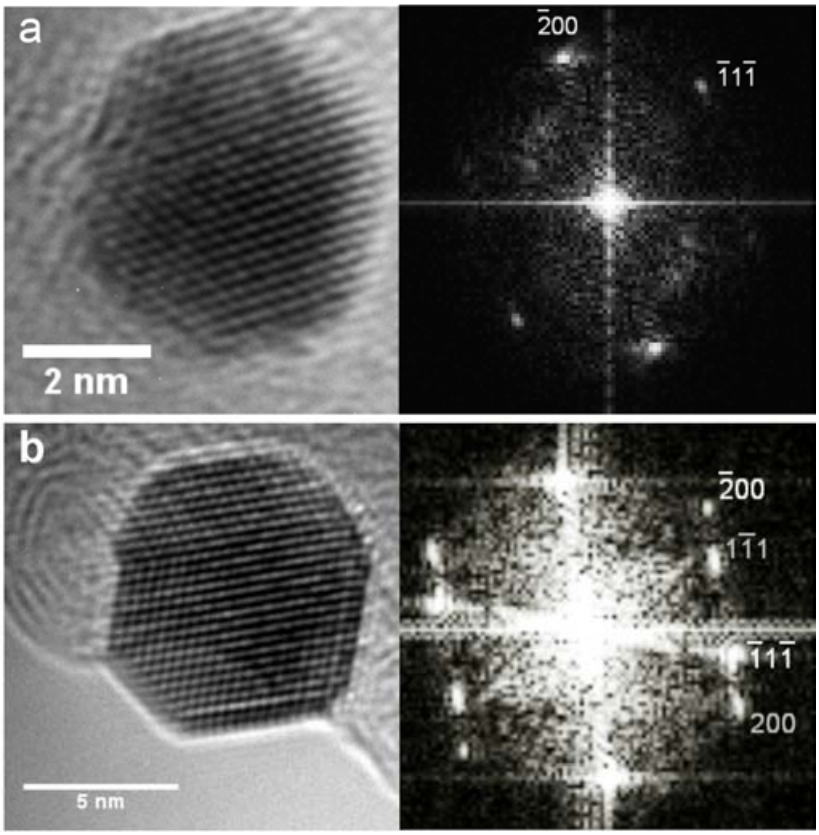


**Figure 4.2.** HRTEM images of two different Cu-Au particles (left) and the corresponding FFTs (right): **(a)** a cuboctahedral particle which has a single-crystal fcc structure; **(b)** a particle having a twinned and deformed structure which is still evolving under the electron beam, grey and white indices are used to discriminate the different orientations of the twin.

The sintering of gold nanoparticles under electron irradiation, as demonstrated previously [214], suggests that "metallurgical processes" may be performed using the TEM. Figure 4.3 shows the aggregation of two Cu-Au particles, stimulated by the electron beam. Originally, two cuboctahedral particles of around 5 and 6 nm (Figure 4.3a) were close to each other and under the electron beam. After around 2 minutes, the two particles were

suddenly stuck to each other (Figure 4.3b), forming a system which is similar to the union of two liquid drops. The system exhibited a continuous change in shape, following a tendency to minimize the surface energy. After the 5$^{th}$ (Figure 4.3c) and 8$^{th}$ (Figure 4.3d) minutes, the interaction between the two different crystallographic orientations of the two particles could be recognized. The possible difference in pressure between the two orientations can be one of the factors which induce mixing of the two crystalline structures. At the 15$^{th}$ minute (Figure 4.3e), one could observe that, the morphological evolution was no longer governed by the tendency to minimize surface energy, but by a regular re-crystallization, forming a new cuboctahedral morphology with an fcc single-crystal structure. The new cuboctahedral particle was observed as stable at the 20$^{th}$ minute (Figure 4.3f), and no significant change in morphology was observed after irradiating this particle for a further 10 minutes.

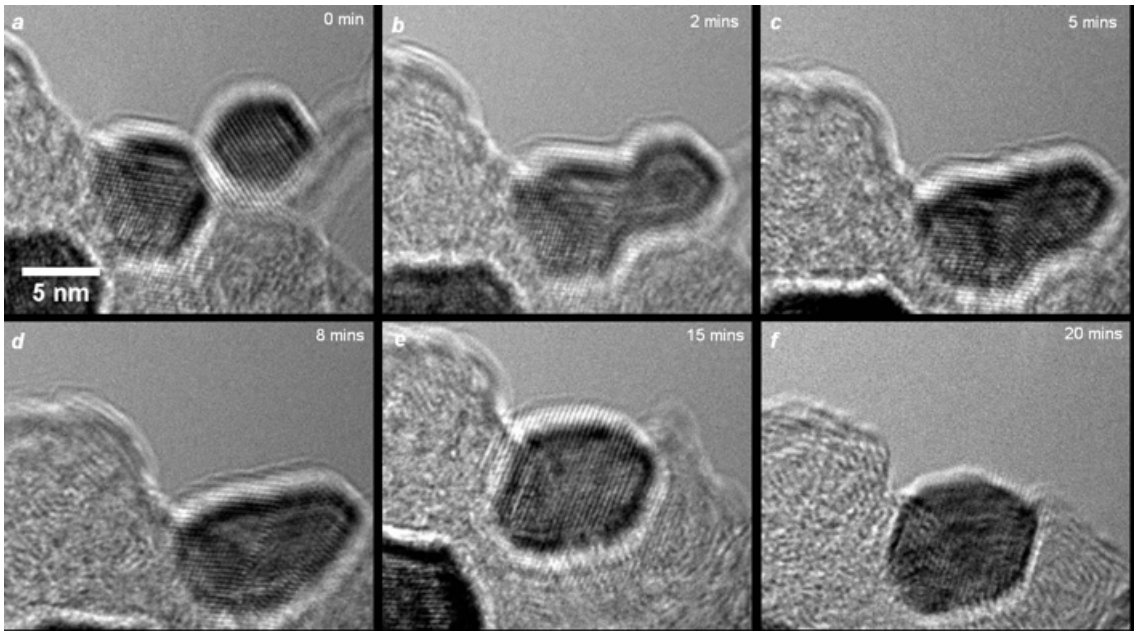


**Figure 4.3.** The aggregation of two particles, observed under a strong electron beam; **(a)** the two initial cuboctahedral particles; **(b)** after around 2 minutes, the two particles started to aggregate with each other to form a twin particle; **(c-d)** the structural evolution of the particle was monitored and recorded at the 5$^{th}$ minute and the 8$^{th}$ minute; **(e-f)** from the 15th minute to the 20th minute, the particle was observed with a new stable single-crystal cuboctahedral structure.

## 4.3.2. Atomic-resolution HAADF-STEM imaging

For the Cu-Au system, $(Z_{Au}/Z_{Cu})^{\alpha} \approx 5.49$ (if $\alpha$ is assumed to be ~ 1.7), so the distribution of Au and Cu in Cu-Au particles can be detected in terms of Z-contrast if there is some segregation between these two elements. However, if Cu and Au are randomly mixed, no clear Z-contrast can be detected for the Cu-Au particle, only thickness contrast is exhibited in HAADF-STEM imaging, similar to a monometallic particle.

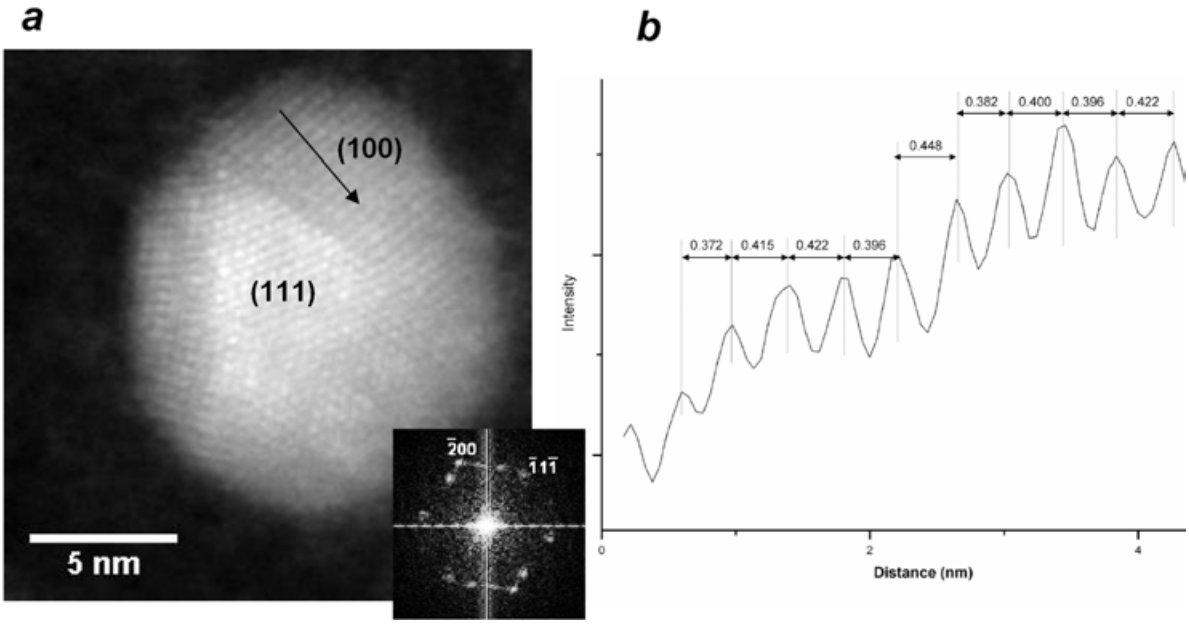


**Figure 4.4. (a)** Atomic resolution HAADF-STEM image of a particle using the VG HB601UX FEG-STEM microscope at Daresbury laboratory, a triangular facet and a square facet can be seen, which may be the (111) and (100) facets, respectively, of a cuboctahedron, the FFT (inset) indicates that the particle is not single-crystal although some lattice planes are indicated; **(b)** an intensity profile along the indicative arrow marked in (a), with lattice parameters estimated in nm. (Dr Quentin Ramasse is acknowledged for taking this HAADF-STEM image).

Figure 4.4a shows an atomic-resolution HAADF image of a Cu-Au particle. While thickness contrast reveals a triangular facet and a square facet which may be the (111) and (100) facets of a cuboctahedron, no Z-contrast can be clearly recognized. The HAADF intensity profile along a line scan (the indicative arrow) on the (100) facet is plotted in Figure

4.4b. The lattice parameters estimated from the intensity profile are quite diverse: 0.372 nm, 0.415 nm, 0.422 nm, 0.396 nm, 0.448 nm, 0.382 nm, 0.400 nm, 0.396 nm, and 0.422 nm. It can be noted as a reference that, the lattice parameter for pure Au and the three stoichiometric $(Au_3Cu)_M$, $(CuAu)_M$, $(Cu_3Au)_M$ particles produced by laser vaporization are 0.407 nm and 0.387 nm, 0.382 nm, and 0.376 nm, respectively [199]. The diversity of the estimated lattice parameters, together with the unrecognizable Z-contrast, supports the idea that the cuboctahedral particles in this work are Cu-Au randomly mixed.

### 4.3.3. SDD-EDX mapping

High resolution X-ray elemental mapping in STEM mode has been proved to be effective for determination chemical orderings of bimetallic nanoparticles, as a core-shell configuration has been demonstrated for Au-Ag nanoparticles which are around 30 nm in size [215]. In STEM mode, the electron probe can be small enough (< 1 nm) to provide an adequate spatial resolution for mapping nanostructures. SDDs with large active areas, which has improved energy resolution and high count-rates, can make elemental mapping for smaller nanoparticles (i.e., around 10 nm) feasible.

The elemental mapping of a Cu-Au particle is presented in Figure 4.5. The HAADF-STEM image (Figure 4.5a) shows a particle of around 9 nm (resulting from aggregation under electron beam) and some small original particles. The distribution map of Cu (Figure 4.5b) is collected using $K_\alpha$ X-rays. Figure 4.5c is the distribution map of Au, using $L_\alpha$ X-rays. The O map in Figure 4.5d is $K_\alpha$ X-rays.

A background Cu signal can be seen in the Cu map, because of the copper TEM grid. However, this background noise is not too high, compared to the signals from the particles, so the correlation between the HAADF image, the Cu and Au maps can be observed even for

some small particles. It is clear that, for the particle shown here, the Au signals are distributed in the same region as the Cu signals, indicating that Au is mixed with Cu inside the particle. It is evident that, there is only a small amount of oxygen contained in the particle, as indicated by the very low level of signal for the O map.

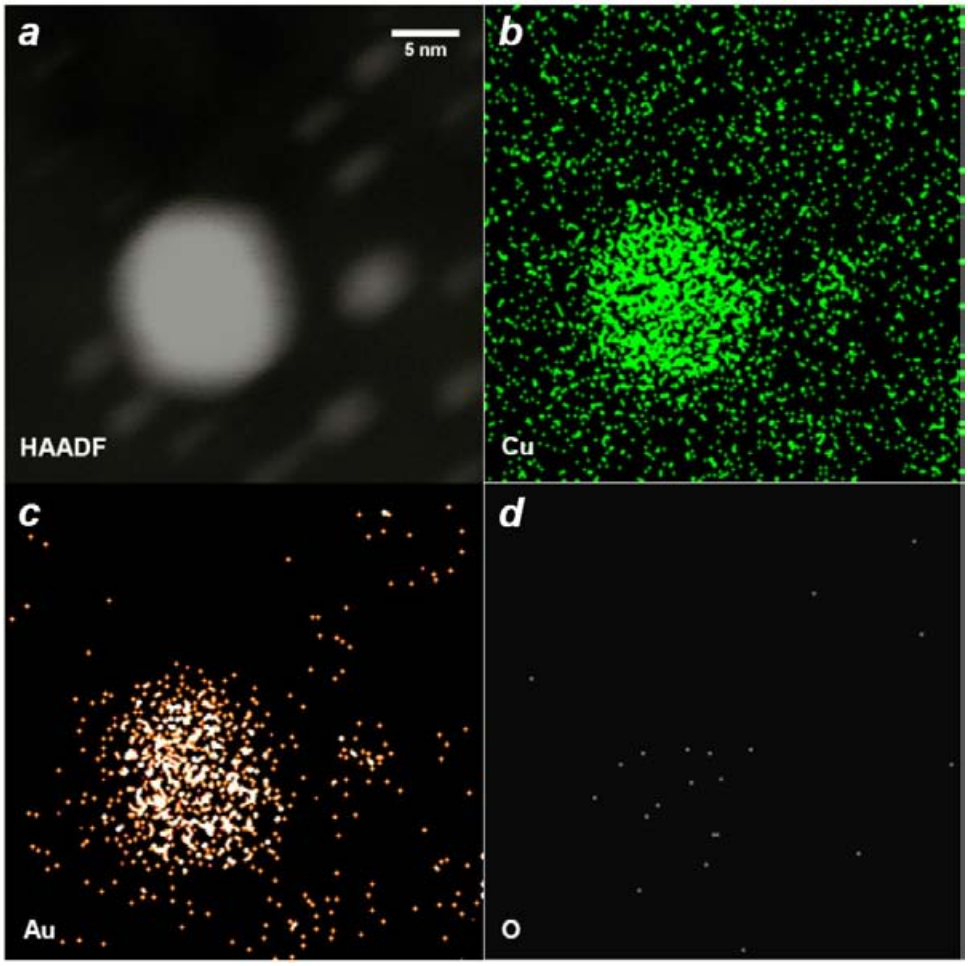


**Figure 4.5.** SDD-EDX elemental mapping for a Cu-Au particle; **(a)** HAADF-STEM image; **(b)** signal intensity from X-ray characteristic $K\alpha_1$ transitions for Cu; **(c)** signal intensity from $L\alpha_1$ transitions for Au; **(d)** signal intensity from $K\alpha_1$ transitions for O.

Although the GE reaction can initially produce Au on the surface of Cu seeds [14], both spontaneous dissolution at room temperature [192-195] and the "metallurgical" dissolution induced by the electron beam occurred. It is interesting that, the Cu-Au particles are

chemically stable in ambient air, as no significant oxidation of Cu can be observed in the element maps. This suggests that our synthesis procedure using nitrogen to prevent Cu oxidation has been successful, and the presence of Au, as well as the thiol-capping ligand, has some roles to make the Cu-Au particles nearly inert to oxygen in ambient air. It is noted that the Xmax SDD detector we used is capable of detecting oxygen (see Chapter 2: 2.3.4).

According to an investigation of the oxidation resistance due to capping ligands [216], alkane-thiols were found to decrease the oxidation rate of Cu particles. The tests performed for different chain-length thiols (C6SH, C12SH, and C18SH) with different thiol:copper molar ratios (1:1, 10:1, and 20:1) showed that the longer chain-lengths and the higher thiol excess ratios improve better the oxidation resistance, although C6SH could decrease the oxidation rate already at the 1:1 ratio. We used dodecanethiol (C12SH) with an excess ratio of 2:1 in our work.

### 4.3.4. Surface plasmon EELS

Figure 4.6 shows an HAADF-STEM image for the Cu-Au nanoparticles at the edge of a hole on the carbon film. It can be seen that, some particles are partially detached from the carbon film so that the electron beam can be positioned on some parts of them without encountering carbon interference.

Four beam positions P1, P2, P3, and P4 are marked on two such particles, as shown in Figure 4.7a, in which P1/P2 and P3/P4 are for the middle/edge of the larger and smaller particles, respectively. The four corresponding low-loss EELS spectra, which have been deconvoluted from a vacuum pre-measured zero loss peak [249], are shown in Figure 4.7b. The energy resolution for these spectra is approximately 0.8 eV. The dependence of SPR on local structure is observed here. A SPR peaking at 2.25 ± 0.05 eV, equivalent to a

wavelength of around 552 nm, is observed for the spectrum corresponding to the P1 beam position at the middle of the larger particle. At the edge of this particle, P2 gives an expanded spectrum, with a SPR peak of 2.90 ± 0.05 eV (428 nm). For the smaller particle, the middle (P3) gives a SPR peak of 2.45 ± 0.05 eV (507 nm), and the edge (P4) gives two SPR peaks at 2.95 ± 0.05 eV (421 nm) and 5.80 ± 0.05 eV (214 nm).

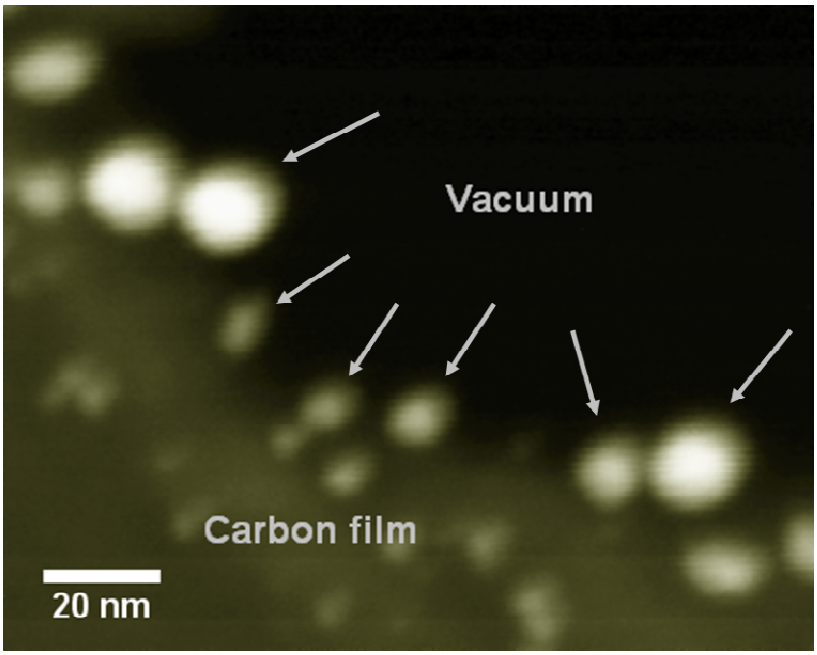


**Figure 4.6.** An HAADF-STEM image for Cu-Au nanoparticles at the edge of a hole on the carbon film; some particles are partially detached from the carbon film (indicated by the arrows) so that the electron beam can be positioned on some parts of them without encountering carbon interference.

According to UV-Vis studies [201, 217], the SPR peaks for Cu-Au particles vary between around 530 nm and 570 nm, which are approximately the SPR values for pure Au and pure Cu particles, respectively. For example, the UV-Vis SPR peaks for the three Au:Cu alloy ratios 3:1, 1:1, and 1:3 nanoparticles are 532 nm, 548 nm, and 562 nm, respectively. Actually, SPR does not only depend on particle size [19] but also on the interaction between metallic surfaces and capping ligands [218]. Besides, there may be some subtle differences

in the excitation process between UV-Vis and EELS experiments, so an exact agreement between these two methods is not necessarily expected [152].

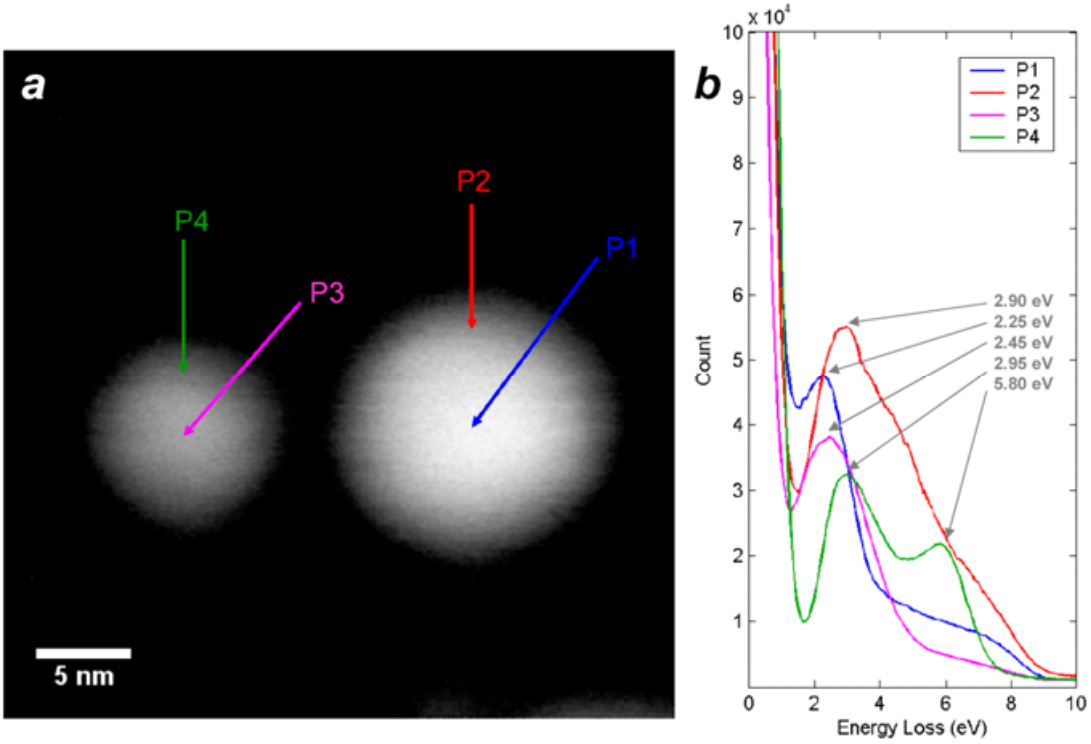


**Figure 4.7.** Localized SPRs from the Cu-Au particles studied by positioning the electron beam in STEM mode; **(a)** HAADF image of two particles having different sizes, four beam positions at their middles and edges are indicated; **(b)** the corresponding SPR spectra for the four beam positions, with the different plasmon energies found.

Previously, plasmon EELS mapping of monometallic Ag and Au nanoparticles has found different SPR modes for different local morphologies [152,153]. In another work on Ag nanoparticles, SPR is reported to be dependent on beam position (that is, dependent on local structure) and on beam damage, which changes the nanostructure [154]. For the Cu-Au particles in our work, we mention here three possible reasons for the different SPRs found at the middle and the edge of two different particles. The first reason is composition varying from the middle to the edge and from one particle to another. One would expect a higher SPR energy (shorter wavelength) at the edge if the particle surface is richer in Au, compared

with the middle. However, a change in SPR energy due to varying composition should not be as much as the values found here, and because of the strong mixing tendency, the change in composition is expected to be small. The second possible reason is that beam damage may change the nanostructure during the signal acquisition, as the Cu-Au particles here are observed to be sensitive to the electron beam. Actually, we set a short acquisition time and a low electron dose to reduce this possibility. The third reason, which we believe to be the main reason for the different SPR energies found, is the strong dependence on local structure of SPR. Because, according to the size-dependence of SPR [19], the smaller particle is expected to have a slightly lower SPR energy (longer wavelength), the higher energy for P3 (2.45 eV), compared with P1 (2.25 eV), can only be explained in terms of differences in structure.

## 4.4. Conclusions

We have reported characterization of dodecanethiol-stabilized Cu-Au nanoparticles using (HR)TEM imaging and STEM-based techniques. The investigation of the morphological evolution under the high-density electron beam of HRTEM has found that cuboctahedron is favoured as the thermodynamically stable morphology for the Cu-Au particles. The observed aggregation of two cuboctahedral particles, forming a larger cuboctahedron, confirms that this morphology predominates over a large range of particle sizes. The atomic-resolution HAADF-STEM imaging for a particle of around 9 nm supports a mixed Cu-Au configuration. This Cu-Au mixing has been clearly confirmed by SDD-EDX elemental mapping, which has also found that the Cu-Au particles were not significantly oxidized when exposed to ambient air, perhaps due to the presences of Au and the capping dodecanethiol.

Finally, the study of localized SPRs, using STEM low-loss EELS, has demonstrated that the SPRs are strongly dependent on the local structures of the Cu-Au nanoparticles.

# CHAPTER 5. MICROBIALLY SYNTHESIZED PALLADIUM-GOLD NANOPARTICES

**Abstract.** Bimetallic Pd-Au particles synthesized via microbial media of *Desulfovibrio desulfuricans* bacteria are characterized using HAADF-STEM combined with SDD-EDX elemental mapping and surface plasmon EELS. When combined with EDX, or theoretical considerations, or EELS, the Z-contrast provided by HAADF-STEM is effective in characterizing the compositional configurations of the bimetallic nanoparticles. Homogeneous mixing and various complex segregations have been found for different particles in this work. The EELS study has also found different behaviours corresponding to surface plasmon resonances in different regions of a single particle, because of its heterogeneity and anisotropy. HAADF-STEM tomography has been performed to obtain three-dimensional (3D) visualization of the nanoparticles.

## 5.1. Literature review

Bimetallic Pd-Au nanoparticles, which have been synthesized and characterized by various methods, are found to be very good catalysts for reactions involving hydrogen [219-222]. It has been seen that the heterogeneity due to the presence of two different metals can make Pd-Au particles have better catalytic performance, compared with monometallic Au or Pd particles [223,224]. In order to understand further the heterogeneity of Pd-Au particles, it is important to investigate the details of their configurations (or chemical ordering). In previous studies, sonochemically synthesized Pd-Au particles were found to have a $Au_{core}Pd_{shell}$ configuration [225, 226], by using the HAADF-STEM technique which produce image

contrast which depends on Z-contrast ($Z_{Pd}$ = 46 and $Z_{Au}$ = 79). However, it is well known that the initial metastable configuration of bimetallic particles actually depends on which method is used to synthesize them. While pre-formed Pd particles were coated with gold layers in early experiments by Turkevich and Kim [227], PVP-stabilized Pd-Au particles made by a successive reduction procedure [228] did not have core-shell configurations, regardless of whether Au or Pd was reduced first. Later synthesis of Pd-Au core-shell particles using successive reduction were carried out by Schmid et al. [229], and both $Au_{core}Pd_{shell}$ and $Pd_{core}Au_{shell}$ were reported. However, it has been argued that, with successive reduction methods, due to the interactions caused by the difference in redox potentials of Au and Pd ions [95], various configurations may be formed. Actually, it has been reported in different experimental studies all of that $Au_{core}Pd_{shell}$, $Pd_{core}Au_{shell}$, multiple-shell, and mixed configurations can be formed [230-234]. According to theoretical studies [180,235,236], the $Pd_{core}Au_{shell}$ configuration is energetically favored, due to the slightly higher cohesive energy of Pd and the lower surface energy of Au. On the other hand, the electron transfer from Pd to Au, as reported in a theoretical study [237], suggests that Pd and Au may have a tendency to form a mixing configuration.

While many synthetic studies of bimetallic Pd-Au particles has been performed, characterization of these particles has been performed commonly by the traditional UV-Vis spectroscopy [219-234] which only provides indirect information on sizes and compositions in terms of surface plasmon absorbance. (S)TEM and (S)TEM-based techniques, which are known to be particularly powerful for nanoparticle studies, have also been widely used, including HAADF-STEM Z-contrast imaging and compositional determination using EDX spectroscopy [223,224,238]. However, experimental studies using the most sophisticated STEM-based techniques such as elemental mapping, STEM-tomography, and STEM low-

loss EELS have not been reported for bimetallic Pd-Au nanoparticles, although such studies have been reported for some monometallic particles, including Au and Pd particles [152,239-242].

In this chapter, we report our characterization and analysis of the configurations, morphologies and plasmonic properties of microbially synthesized Pd-Au nanoparticles, using STEM-based techniques. We present here: (1) HAADF-STEM imaging combined with SDD-EDX elemental mapping and theoretical analysis; (2) HAADF-STEM tomography which gives a 3-D visualization of a single Pd-Au particle; (3) surface plasmon EELS which investigates the SPRs of a single particle.

## 5.2. Experimental and computational details

### 5.2.1. Experimental details

The bimetallic Pd-Au nanoparticles were synthesized by Deplanche and Mascakie (School of Biosciences, University of Birmingham) [143] using a microbial method combined with successive reduction procedure. In brief, cells of *Desulfovibrio desulfuricans* were grown and palladized as described previously [117,120,121] to a loading of 5% Pd by weight. The bio-$Pd^0$ suspension was harvested by centrifugation (4000 rpm, 10 min, 15°C), washed twice in distilled water and resuspended in degassed water ($dH_2O$) so that the final ratio of 1 mM $Au^{3+}$:bio-$Pd^0$ suspension was 4:3 (v:v). The degassed resuspended bio-$Pd^0$ was transferred anaerobically into a bottle containing an appropriate amount of 1 mM Au(III) solution (from $HAuCl_4$. nH2O, pH 2.3) saturated with $H_2$ by bubbling gas (200 ml/min, 1 hour). The bio-$Pd^0$/$Au^{3+}$ mixture was left to react 3 hours on a rotary shaker (150 rpm, 30°C ) during which the suspension developed an intense purple colour. The final ratio of Pd:Au was 1:1 by mass

(10% total metal loading on bacterial cells by weight). The bio-Pd/Au precipitate was harvested and dried as described previously [117,120,121].

The bacteria which contain the particles were dispersed in water and then deposited on a carbon thin film coating copper TEM grids (*Agar Scientific*). The thickness of the carbon film is approximately 20-30 nm.

A field emission gun Tecnai F20 microscope operating at 200 kV was used for high resolution (HR)TEM and HAADF-STEM imaging. In the HAADF-STEM mode: the smallest condenser aperture C2 = 30 μm (which lowers the electron dose as well as reducing the beam damage) was used; the C1 lens was set to spot size 8; the electron probe size is smaller than 1 nm; the camera length was 150 mm so that the inner semi-collection angle for the HAADF detector was 40 mrad. The short camera length was chosen to minimize noise and artefacts caused by diffraction contrast and bright- field electrons.

An *Oxford Instruments* X-Max SDD (see Chapter 2: 2.3.4) was attached to the microscope to perform EDX elemental mapping in HAADF-STEM mode. The collection solid angle is approximately 1.3 srad. The specimen was tilted to 18 degrees. Detector control, analyzing and processing were performed using INCA software which also provides the *SiteLock*$^{TM}$ function to correct automatically the drift of the particles.

The EELS study was performed using a Gatan 666 PEELS system controlled by Gatan EL/P 3.0 software. Low-loss EELS studies on carbon-supported nanoparticles are affected by the strong signal from the bulk plasmon peak (at around 23 eV) of the carbon film which overwhelms the low-loss region. To tackle this problem, some holes in the film were exploited to avoid the carbon interference. An area where there were some bacteria suspending particles in the middle of a hole was chosen. The electron probe was positioned at some interesting particles suspended by the bacteria, without the carbon superimposition.

A semi-acceptance angle of approximately 4 mrad and an energy dispersion of 0.05 eV were used for the low-loss EELS. For each acquisition, 10 accumulations with an accumulation time of 1 second were set to obtain an adequate signal and an acceptable degree of degradation in spatial resolution due to particle drift.

A tilt series of 19 HAADF images of a single particle was taken for a tomographic reconstruction. The tilt range is 90 degrees (from -45 to +45 degrees), with a tilt step of 5 degrees. Previous reports have suggested that a tilt range of 75 – 80 degrees should be sufficient to minimize artefacts and the reconstruction based on this range should not cause serious errors when determining the 3D object shapes and measuring the 3D object sizes [139, 244]. The large tilt step used in this work, and thus the small number of images in the tilt series could lower signal/noise ratio for reconstruction. However, the large tilt step reduces the probability of encountering major zone axes where extraordinary high-angle scattering, due to strong Bloch wave channelling, arises [139,140].

## 5.2.2. Computational details

An HAADF image of a spherical particle which is homogeneously Pd-Au mixed is simulated by using Matlab program (see Appendix 5A, page 117, for the simulation code). For this homogeneous particle, the HAADF intensity can be simply formulated as:

$$I_{HAADF}(x,y) = CZ^{\alpha}\sqrt{R^2 - x^2 - y^2} \quad . \tag{5.1}$$

where $C$ is a normalization constant, $R$ is the radius of the spherical particle, $x$ and $y$ are the electron probe coordinates in a 2D projection of the particle, $Z^{\alpha}$ is a constant for a given homogeneously mixed particle. It is noted that due to the geometrical symmetry of a sphere, spherical and semi-spherical shapes can not be distinguished in this simulation).

54-atom Pd-Au clusters were modelled using the BCGA and the Gupta potential (see Chapter 2: 2.1.2) fitted to DFT-calculated energies of Pd, Au and Pd-Au solids [236]. The Gupta parameters are listed in Table 5.1.

**Table 5.1.** Gupta potential parameters for Pd-Au nanoclusters [236].

| Parameter | Pd-Pd | Pd-Au | Au-Au |
|---|---|---|---|
| A(eV) | 0.1653 | 0.1843 | 0.2091 |
| p | 10.8535 | 10.5420 | 10.2437 |
| $r_0$ (Å) | 2.7485 | 2.8160 | 2.8840 |
| $\zeta$ (eV) | 1.6805 | 1.7867 | 1.8097 |
| q | 3.7516 | 3.8826 | 4.0445 |

The tomographic reconstruction was performed using TomoJ [245], a plug-in code of the software ImageJ [207]. The Algebraic Reconstruction Technique (ART) [246,247] was selected for the running of TomoJ with 10 iterations per reconstruction. The final tomogram was rendered using the UCSF Chimera visualization software [248]. In order to intensify signals and lower random noise from the aligning and calculating procedures, two different reconstructions were overlapped to render a single 3D tomogram.

## 5.3. Results and discussion

### 5.3.1. Nanoparticle formation by cells of *D. desulfuricans*

Figure 5.1 shows an HAADF image of Pd-Au particles accommodated in the intracellular space, periplasmic space and at the cell surface of a *Desulfovibrio desulfuricans* bacterium. According to the histogram (inset), particles of various sizes can be found, ranging from around 4 nm to around 40 nm in diameter. Particles of approximately 15-20 nm which are typical for the microbial reduction are of interest in this study.

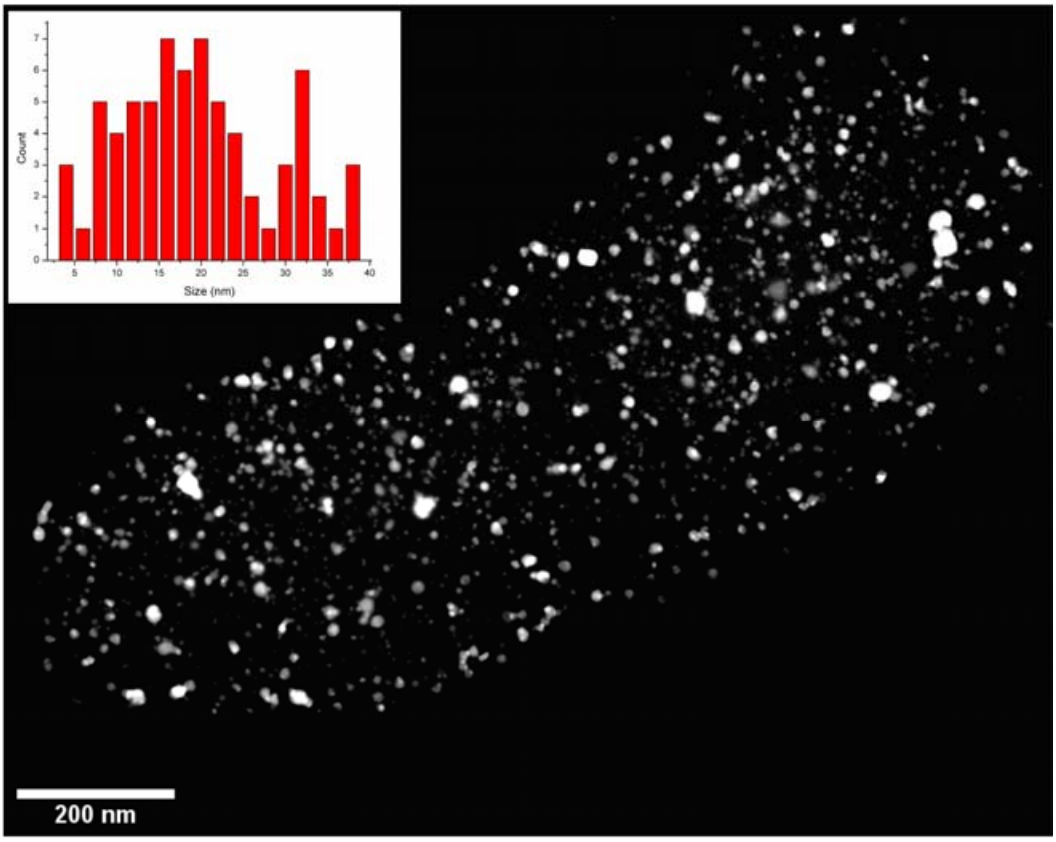


**Figure 5.1.** HAADF image of Pd-Au particles created on the body of a bacterium. The inset is the size-distribution histogram. Various sizes and morphologies are observed.

Although some particles are close to icosahedral, decahedral and truncated-tetrahedral geometries, their shapes are generally not well-defined polyhedra. One of possible reasons could be that the initial reduction of palladium nanoparticles is enzymatic-driven and that might not lead to structures observed traditionally during chemical reduction. Figure 5.2 shows the HRTEM image (Figure 5.2a) of a particle along the <-111> orientation and its corresponding FFT (Figure 5.2b).

Figure 5.3 is an HAADF image of some particles which may have complex compositional configurations. Here, the HAADF intensity is insufficient to distinguish the thickness contrast and the Z-contrast. However, these two types of contrast can be distinguished with the help of elemental mapping and theoretical calculations.

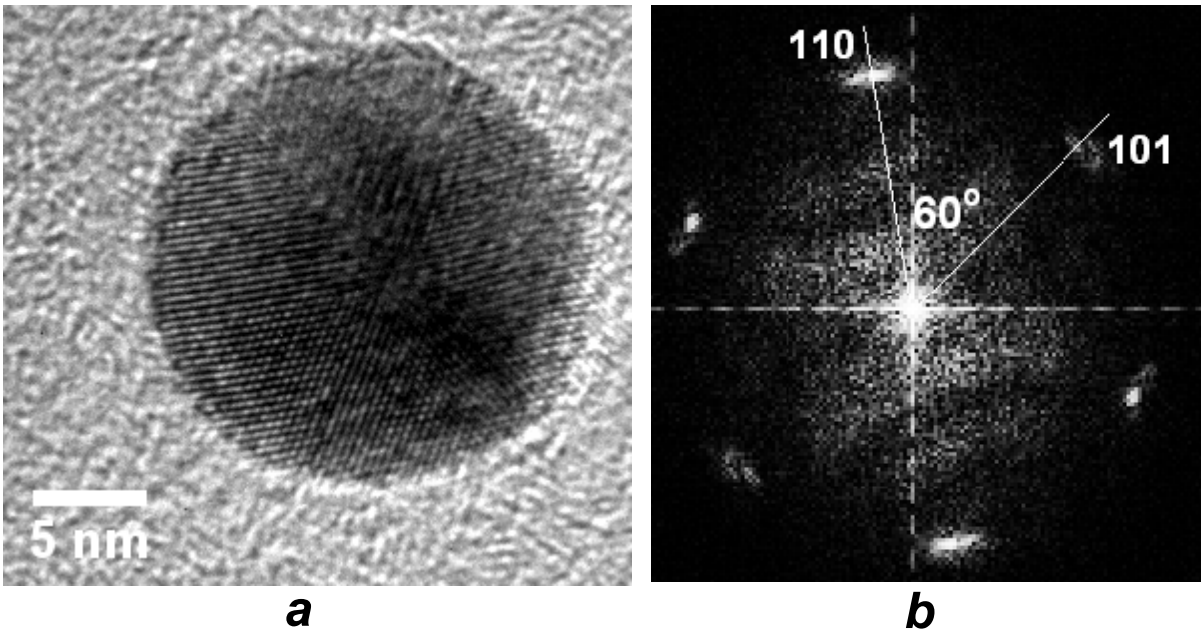


**Figure 5.2. (a)** HRTEM image of a particle along the <-111> orientation and **(b)** the corresponding FFT.

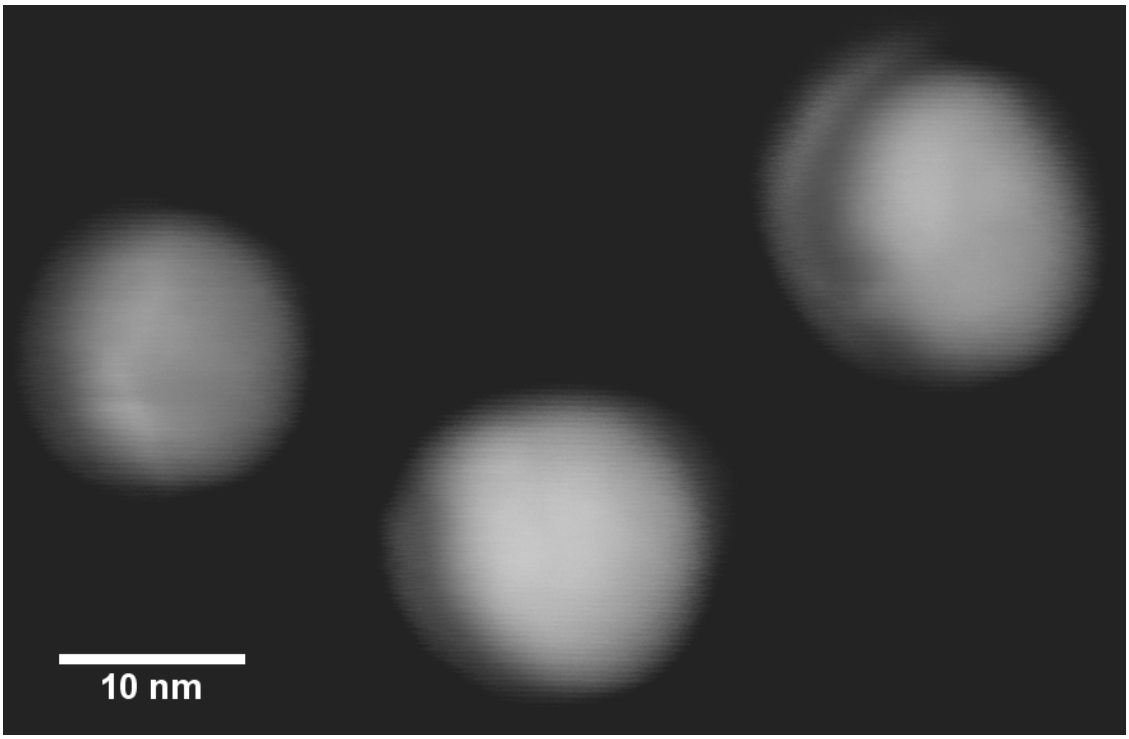


**Figure 5.3**. HAADF image of some Pd-Au particles; here Z-contrast and thickness contrast can not be unambiguously distinguished.

## 5.3.2. SDD-EDX mapping

Two bimetallic Pd-Au particles of around 16 nm were found to have different compositional configurations by elemental mapping, as shown in Figure 5.4. The HAADF intensity (Figure 5.4a) suggests that there may be Pd-Au segregation for the particle on the left side due to the Z-contrast, while only thickness contrast can be seen for the particle on the right side, which is believed to be chemically homogeneous. This suggestion is confirmed by the Au and Pd distributions (see Figure 5.4b and 5.4c, respectively) featuring the characteristic X-ray signals from $L_{\alpha 1}$ transitions (between $M_5$ and $L_3$ energy levels) for the Au and Pd atoms. The left particle has a Pd-rich region which correlates with the Au-poor region and the lower HAADF intensity.

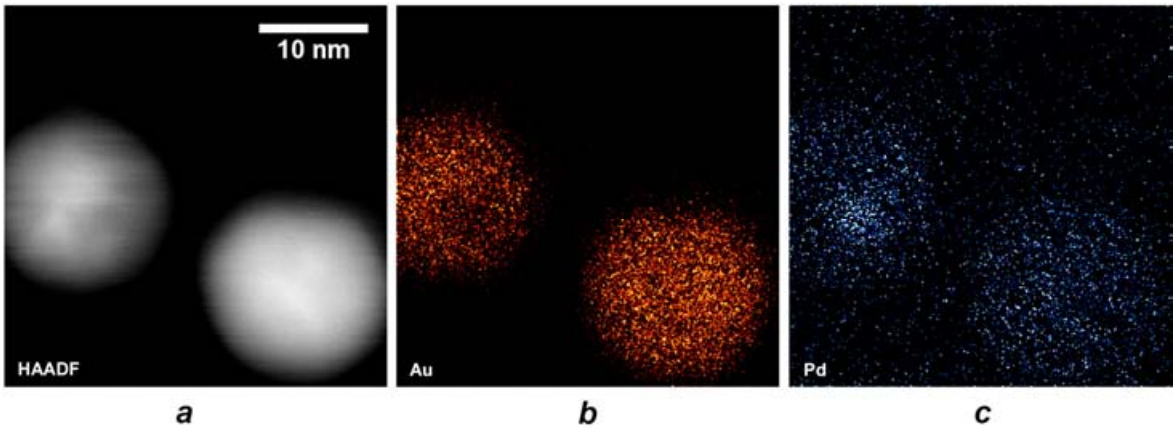


**Figure 5.4.** EDX mapping of two Pd-Au particles shows the Au and Pd distributions: **(a)** HAADF image; **(b)** X-ray signal intensity from the characteristic $L_{\alpha 1}$ transitions of Au; **(c)** the characteristic $L_{\alpha 1}$ transitions of Pd. The particle on the left side has segregation between Pd and Au with a clearly observed Pd-rich region, which is consistent with the HAADF Z-contrast, the particle on the right side has homogeneous mixing between Pd and Au.

To analyze further the homogeneous mixing of the particle on the right (in Figure 5.4a and presented again in Figure 5.5a), a theoretical HAADF image was simulated for a spherical homogeneous particle. Figure 5.5b shows the simulated image where only

thickness contrast is considered. The line-scan intensity profiles (Fig. 5.5c) show an agreement between the theoretical and experimental images (Fig. 5.5a), where the theoretical maximum intensity value is fitted to the experimental one. This agreement confirms the homogeneous mixing of the experimental particle and confirms that it is close to either spherical or semi-spherical.

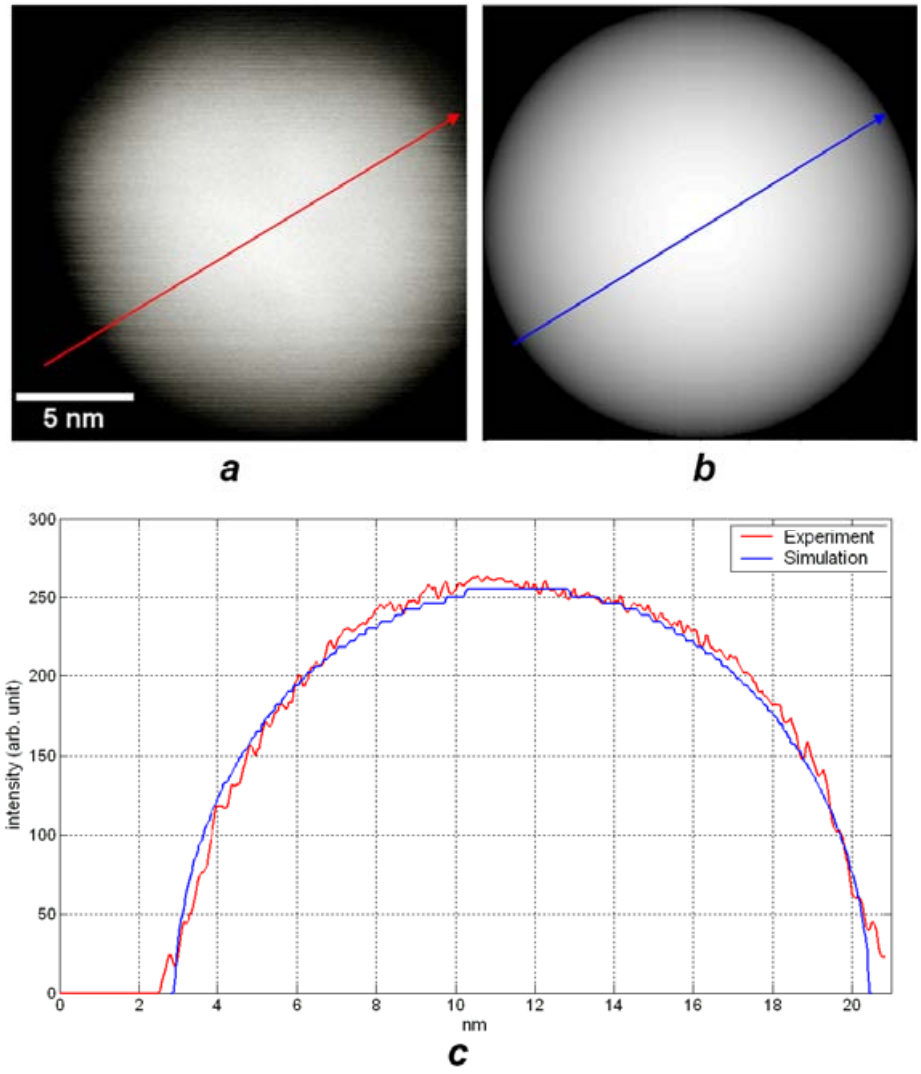


**Figure 5.5.** HAADF thickness contrast: simulation compared with experiment; **(a)** the experimental HAADF image of the Pd-Au mixed particle; **(b)** the simulated HAADF image for a spherical mixed Pd-Au particle; **(c)** the line-scan intensity profiles of the experimental and simulated HAADF images.

Different compositional configurations found for the bimetallic Pd-Au particles may result from the complicated reactions between Pd and Au in a reducing medium [95]. When an aqueous solution $HAuCl_4$ is introduced after the formation of metallic Pd particles, the surface $Pd^0$ atoms can be oxidized, resulting in Pd ions and metallic $Au^0$ atoms which may be deposited on to the Pd seeds. The resulting Pd ions may also be partially reduced back to metallic Pd in the reducing medium (i.e. the microbial medium). Although this mechanism is affected by many factors present in the medium as well as the experimental conditions, there may be some possibility for particles having Pd cores and complex shells to be formed.

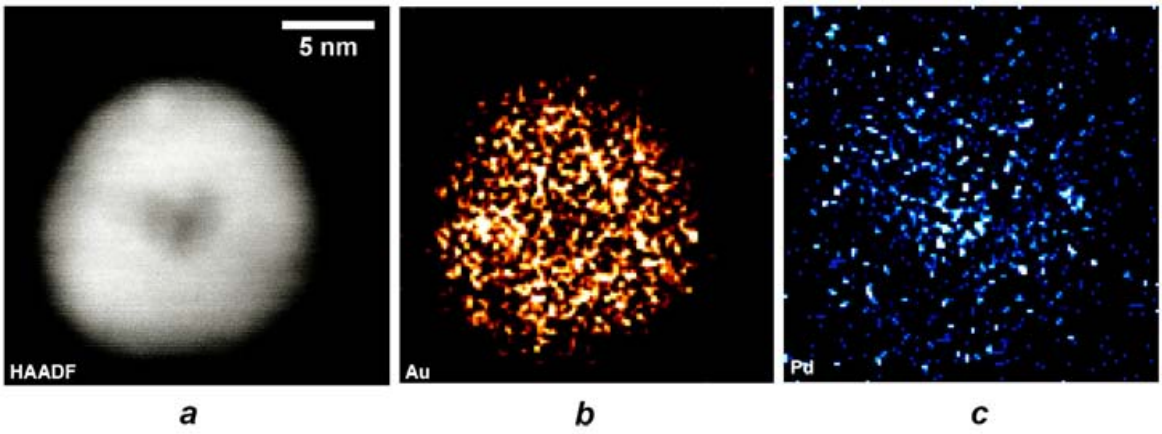


**Figure 5.6.** SDD-EDX mapping of a Pd-Au particle: **(a)** HAADF image; **(b)** $L_{\alpha 1}$ Au signal; **(c)** $L_{\alpha 1}$ Pd signal. The darker centre observed in the HAADF image correlates with the high signal intensity of Pd and the low signal intensity of Au in the centre of the particle. The Z contrast, combined with the element distributions, supports the idea that the particle has a Pd-core, an intermediate Au-shell and an outermost mixed Pd-Au shell.

Figure 5.6 shows elemental mapping for a Pd-Au particle. The HAADF image (Figure 5.6a) exhibits a darker region in the middle of the particle, which correlates with the Au-poor and Pd-rich region shown in the X-ray intensity images, and can be clearly attributed to the lower HAADF intensity of Pd. This particle has a small Pd core, a thick Au-rich intermediate shell and a thin Pd-Au mixed surface shell.

From the modeling of 54-atom Pd-Au clusters using the Gupta-BCGA, the $Pd_{core}(Pd\text{-}Au)_{shell}$ configuration is found to be energetically favored. Figure 5.7 shows the lowest-energy structures for two compositions, $Pd_{24}Au_{30}$ and $Pd_{30}Au_{24}$, which have icosahedral geometries. Although the sizes of these structures obviously do not match the sizes of the experimental particles, the tendencies for Pd atoms to occupy the core and to mix with Au atoms on the surface can be interpreted as an energetic stabilization.

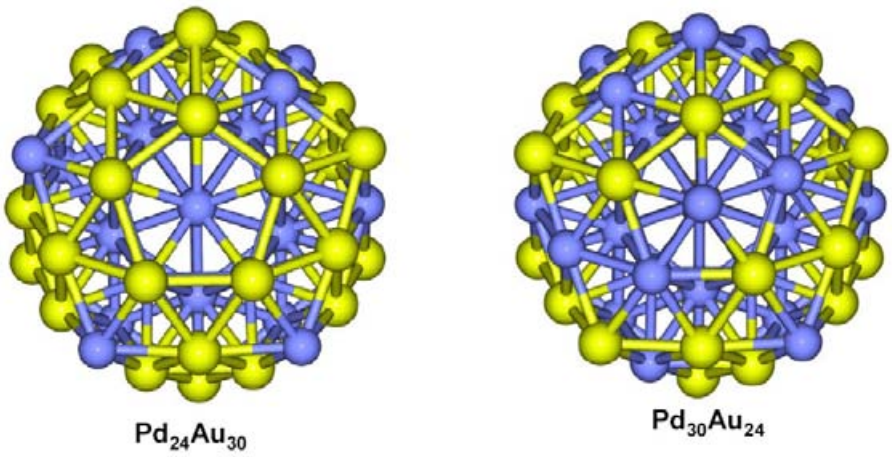


**Figure 5.7.** Models of 54-atom Pd-Au clusters simulated using the Gupta-BCGA. The two compositions $Pd_{24}Au_{30}$ and $Pd_{30}Au_{24}$ presented here have icosahedral geometries and exhibit $Pd_{core}(Pd\text{-}Au)_{shell}$ configurations.

## 5.3.3. Surface plasmon EELS

Figure 5.8a shows an HAADF image of a Pd-Au particle lying on the edge of a bacterium (not visible). In this condition, the particle is suspended in the middle of a film hole so there is no carbon interference. Three different beam positions for acquiring low-loss EELS spectra are marked as P1, P2, and P3. Figure 5.8b shows the spectra corresponding to the three beam positions after deconvolution with a vacuum pre-measured zero loss peak [249]. The energy resolution for these spectra from the particles is approximately 0.8 eV. Beam position P1 gives a clear SPR peak at 2.35 ± 0.05 eV. This corresponds to a wavelength of

around 528 nm, which is typical for SPRs for Au nanoparticles studied using UV-Vis spectroscopy, noting that the surface plasmon wavelength decreases (energy increases) with increasing particle size [19,250]. Previous EELS mapping found a surface plasmon energy of 2.45 ± 0.05 eV for a 35 nm spherical Au particle and a value of 2.40 ± 0.05 eV for the transverse resonance of an Au nanorod having a diameter of around 18 nm [152]. The spectra for P2 and P3 are weaker and broaden toward higher energies. The SPRs for P2 and P3 have peaks at 2.95 ± 0.05 eV (~ 421 nm) and 3.00 ± 0.05 eV (~ 414 nm), respectively.

It has been reported after UV-Vis studies that there is no clear SPR observed for monometallic Pd particles [251-254] and the presence of Pd in Pd-Au particles causes spread and attenuation of the SPRs [225,255-257]. In this work, the beam position P1 belongs to the brighter region of the HAADF image (Figure 5.8a) while P2 and P3 lie in the darker region. Together with the plasmon spectra (Figure 5.8b), the HAADF contrast here can be mainly attributed to the Pd-Au Z-contrast and it is consistent with a description of the particle having some degree of both Pd-Au segregation and Pd-Au mixing, in which the bottom-left region is Au-rich, the top-right region is Pd-rich and the middle region is a Pd-Au mixture.

Changes in surface plasmon energies with beam position have been reported in a previous EELS study of Ag nanoparticles [154]. These changes are sensitive to local nanostructure and geometry, which may not only change when the position changes but may also change due to electron beam damage. In our work, we are confident that the electron beam damage is negligible because the Pd-Au particles are quite stable (no significant change in structure was observed during the HRTEM investigation), the total acquisition time for each spectrum is short (10 seconds) and a low electron dose was set in STEM mode (the smallest C2 aperture was used). In fact, two different acquisitions performed with the same beam position gave the same plasmon energy. Hence, the shifts of plasmon peaks

shown in Figure 5.8b can be explained in terms of the three positions P1 P2 and P3 having different local compositions.

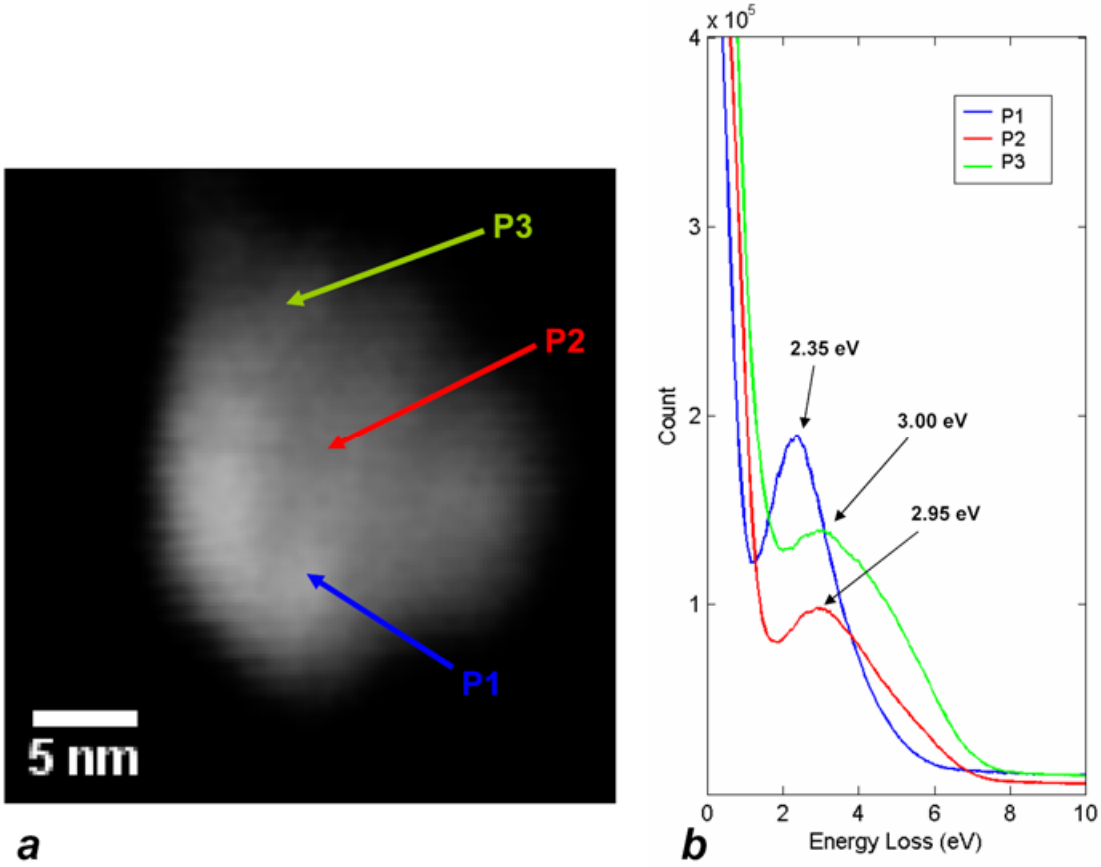


**Figure 5.8.** STEM-EELS spectra in the low-loss region for a Pd-Au particle, which shows the dependence of plasmon resonances on local structure and composition: **(a)** HAADF image of the particle and indication of the three different beam positions P1, P2, P3 at which the EELS spectra were acquired; **(b)** EELS spectra corresponding to the three beam position P1, P2, P3. The position P1 gives a clear plasmon peak at 2.35 ± 0.05 eV while for the positions P2 and P3, the corresponding plasmon peaks (at 2.95 ± 0.05 and 3.00 ± 0.05 eV, respectively) become weaker and spread, and shift to higher energy-loss values. It can be noted that, in agreement with the HAADF contrast, position P1 is brighter, which can be attributed to an Au-rich area in comparison with the darker positions P2 and P3.

### 5.3.4. HAADF-STEM tomography

Some images from the tomographic tilt series are shown in Figure 5.9, where the changes in 2D projections can be observed. The dark backgrounds of these images indicate that the noise from the carbon film is low due to its thinness and low atomic number ($Z_C = 6$).

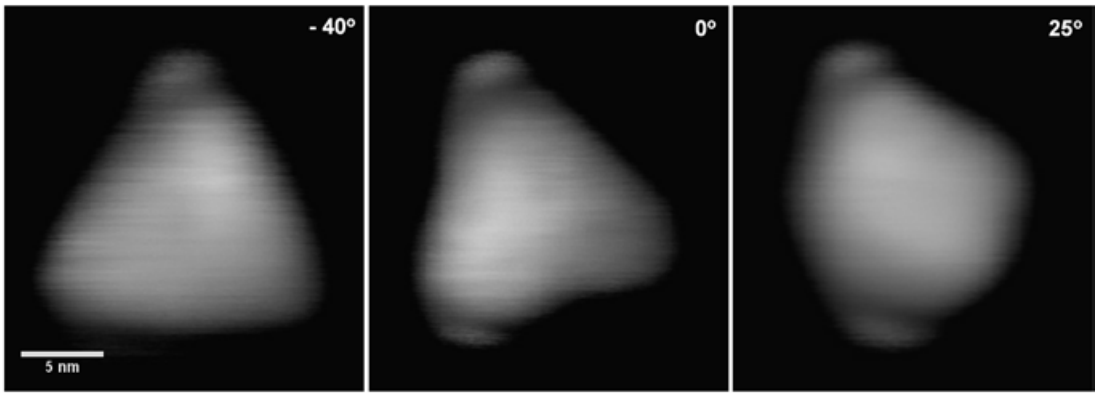


**Figure 5.9.** Some HAADF images from the tilt series for a Pd-Au particle: **(a)** tilting angle of -40 degrees; **(b)** tilting angle of 0 degree (no tilting); **(c)** tilting angle of 25 degrees.

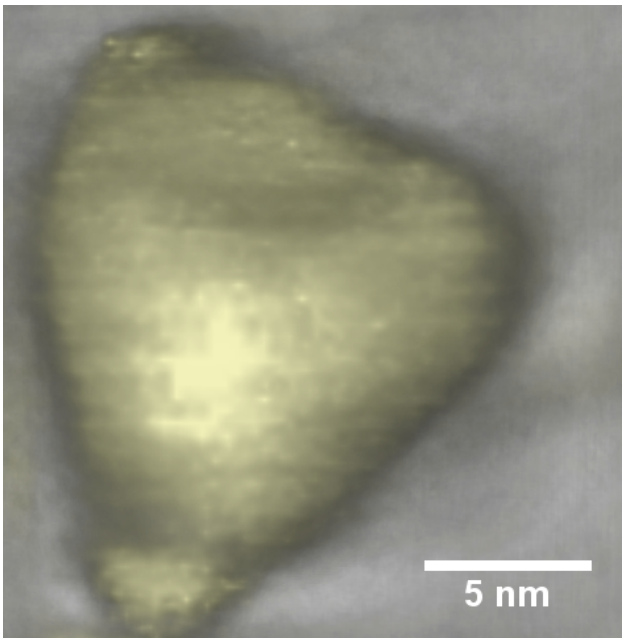


**Figure 5.10.** A view of the 3D tomogram for a Pd-Au particle, which was reconstructed from a tilt series of 19 HAADF images. The tilt series was performed by tilting the specimen through a range of angles from -45$^{o}$ to +45$^{o}$, with a tilt step of 5$^{o}$.

Figure 5.10 shows a view of the reconstructed tomogram where a complicated 3D morphology can be observed from the result. The particle geometry is not well-defined, although it can be described as a triangular prism with considerable random deformation. Due to the deformed geometry, it is not feasible to determine the dimensions of the

tomogram. However, if an "effective diameter" of around 15 nm is assumed, the resolution for the tomogram is estimated of around 2.5 nm (using Equation 2.47).

## 5.4. Conclusions

We have reported in this chapter the characterization of microbially synthesized Pd-Au nanoparticles using SDD-EDX mapping, surface plasmon EELS, and tomography via STEM. We have shown the reliable determination of compositional configurations for bimetallic Pd-Au particles by utilizing HAADF contrast (Z-contrast and thickness contrast) along with EDX elemental mapping and plasmon-EELS beam-positioning. The bimetallic particles presented in this study have various possible configurations, including asymmetric segregation, homogenous mixing, $Pd_{core}Au_{shell}(Pd\text{-}Au)_{shell}$, and left-right phase-segregation with a mixed interface. Different surface plasmon energies found for different electron beam positions on a single particle confirm that the plasmon resonance is sensitive to local structure. Finally, 3D visualization of a particle has been achieved using HAADF-STEM tomography.

**Appendix 5A.** Matlab code for a simulated HAADF image of a spherical particle

```
%----------------------COORDINATION----------------------
x1 = -R:0.05:R;
x2 = fliplr(x1);
x = [x1 x2];

lex = length(x);

y1 = sqrt(R^2 - x1.^2);
y2 = -sqrt(R^2 - x2.^2);
y = [y1 y2];

%-----------------------CALCULATION-----------------------
HAADF = ones(lex);

for j = 1:lex
   for k = 1:lex
    h = sqrt(R^2 - x(j)^2 - y(k)^2);
    HAADF(j,k) = h;

 end
end

%-----------------------------IMAGE-------------------------------
size(x)
contour(y,x,HAADF,50);
HAADF = real(HAADF);
pcolor(y,x,HAADF)
axis ij square

colormap(gray)
shading flat
```

# CHAPTER 6. THEORETICAL STUDY OF 40-ATOM PLATINUM-GOLD CLUSTERS

**Abstract.** This chapter is dedicated to a theoretical study of 40-atom Pt-Au clusters which are of interest due to the electronic shell closure of 40-atom noble metal clusters (in the jellium model). Structures based on truncated-octahedral, icosahedral, decahedral and 5-fold pancake geometries are found to be energetically favoured for different composition regions at the EP level and this is partially confirmed at the DFT level. The large HOMO-LUMO gaps found for the icosahedral and 5-fold pancake structures indicate electronic shell closure effects, while the truncated-octahedral and decahedral structures have small gaps. The DFT calculations confirm that, for $Pt_{20}Au_{20}$ truncated-octahedral structures, the $Pt_{core}Au_{shell}$ configuration which has two Au atoms capping the (100) facets is most energetically favoured, and the layered (phase segregated) configuration also has lower energy compared with the $Au_{core}Pt_{shell}$ and mixed configurations. A Mulliken population analysis was also carried out for different configurations of the $Pt_{20}Au_{20}$ truncated-octahedral structures and the charge transfer phenomena in these cluster structures are described.

## 6.1. Literature review

In the bulk Pt/Au system, there is a miscibility gap at low temperature where Pt and Au are immiscible and Au prefers to segregate to the surface because of its lower surface energy [258]. However, at high temperatures, a continuous Pt-Au solid solution can be formed [29]. In the nano-scale regime, the matter of the most stable configurations for Pt-Au clusters is complicated. Different configurations have been reported experimentally, though some may

be meta-stable. Mixed [259,260], $Pt_{core}Au_{shell}$ [261,262], and $Au_{core}Pt_{shell}$ [30,263] configurations have been reported by different groups. In a remarkable experiment [30], the $Au_{core}Pt_{shell}$ configuration was maintained when the bimetallic nanoparticle was thermally annealed at 300$^{o}$C for 24 hrs but changed to a layered segregation after annealing at 600$^{o}$C.

There have been few theoretical studies of Pt-Au clusters. The electronic properties and structures of very small clusters PtAu, $Pt_3Au$, and $PtAu_6$ have been studied using DFT [264,265]. In another DFT study of 13-atom clusters [266], icosahedral $Pt_{core}Au_{shell}$ configurations were found, where the Pt atom of $PtAu_{12}$ favours being in the core and the Au atom of $P_{12}Au$ preferentially occupies a surface vertex site. Recently, a theoretical study of $Pt_mAu_m$ (m = 1-50) clusters, using the empirical Gupta many body potential – genetic algorithm searches and DFT calculations for m = 1-10, has been conducted by Logsdail et al. [267]. The $Pt_{core}Au_{shell}$ configuration was found to be energetically favoured in this study. DFT local geometry optimizations confirmed this for small clusters (up to 20 atoms). Although the structures and stabilities of Pt-Au clusters, up to 100 atoms, have been described at the empirical potential level of accuracy, ab initio treatments (e.g., at the DFT level of accuracy) for Pt-Au clusters larger than 20 atoms have not been reported. Beside cohesive energy and surface energy, lattice-mismatch strain and geometry-induced charge transfer [186,268] may also affect the configurations of larger clusters.

In this chapter, we report a theoretical study of 40-atom Pt-Au clusters performed using the combined EP-DFT approach (see Chapter 2: 2.1.7). The size of 40 atoms corresponds to an electron magic number for one-valence-electron metallic clusters in the jellium model [71,72], which may make the clusters exhibit electronic and structural shell closure effects as found in a theoretical study of 40-atom Cu-Ag and Cu-Au clusters conducted by Barcaro et al. [163].

## 6.2. Computational details

In this work, the searches for lowest-lying energy structures for all the compositions of $Pt_nAu_{40-n}$ clusters are performed using the Gupta-BCGA (see Chapter 2: 2.1.2 for the program inputs). The Gupta Pt-Pt and Au-Au parameters were derived by Cleri and Rosato [69] and the heteronuclear Pt-Au parameters are those derived by Logsdail et al. as averages of the Pt and Au parameters [267]. These parameters are listed in Table 6.1.

**Table 6.1.** Gupta parameters for the Pt-Au clusters.

| Parameter | Pt-Pt [69] | Au-Au [69] | Pt-Au [267] |
|---|---|---|---|
| *A (eV)* | 0.2795 | 0.2061 | 0.25 |
| *ζ (eV)* | 2.6950 | 1.7900 | 2.2 |
| *p* | 10.6120 | 10.2290 | 10.42 |
| *q* | 4.0040 | 4.0360 | 4.02 |
| $r_o$ *(Å)* | 2.7747 | 2.8840 | 2.83 |

The lowest-lying energy structures found at the empirical level are then recalculated at the ab-initio DFT level (local geometry optimizations). The NWCHEM 5.1 quantum chemistry package [166] has been used to perform DFT calculations, with the Perdew-Wang PW91 exchange-correlation functional [167]. Spherical Gaussian-type-orbital basis sets of double-zeta valence quality for both Pt and Au [168] (7s5p5d)/[6s3p2d] with effective core potentials [169] have been used (each effective core covers 60 inner electrons, leaving 18 and 19 outer electrons for Pt and Au, respectively). Charge density fitting was adopted for calculation of the Coulomb potential [170] for Pt (9s4p3d3f4g)/[9s4p3d3f2g] and for Au (9s4p4d3f4g)/[8s4p3d3f2g]. A Gaussian-smearing technique for the fractional occupation of the energy levels (with a broadening factor of 0.82 eV) is applied. The calculations were performed on the University of Birmingham's BlueBEAR high performance computer [179].

Different configurations ($Pt_{core}Au_{shell}$, $Au_{core}Pt_{shell}$, mixed, and layered segregation) of the $Pt_{20}Au_{20}$ cluster are also energetically compared at the DFT level. Energetic and stability analysis, structural distribution, structural competition, calculation HOMO-LUMO energy gaps, and Mulliken population analysis (MPA) are carried out.

## 6.3. Results and discussion

### 6.3.1. Structural distribution at the empirical level

Stable structures for all the compositions of $Pt_nAu_{40-n}$ clusters were found by using BCGA to perform global minimum (GM) searches for the Gupta potential. Figure 6.1a shows the structural distribution along variation in excess energies. Figure 6.1b is a plot of the second difference in energy for the $Pt_nAu_{40-n}$ clusters, measuring the relative stability of each composition with respect to its neighbours. Some compositions are marked out as having high relative stabilities (n = 7, 13, 22, 38). There are 5 structural motifs which occur as the most stable structures for certain compositions. The bi-capped truncated-octahedral (bi-capped-TO) motif is found for n = 0, n = 21-24, and n = 36-40 (blue regions). The bi-capped-TO structure is described here as either a distorted or regular 38-atom truncated-octahedron (TO) capped with two extra atoms on the surface. TO-based structures with fcc-packing were frequently found in previous theoretical studies of 38-atom and 40-atom clusters [163,180,268]. The incomplete-icosahedral-Mackay (inc-Ih-Mackay) motif ($C_s$ symmetry), which was described previously for 38-atom clusters [180] as a fraction of a 55-atom Mackay icosahedron, is found for n = 1, 2, and n = 6-10 (green regions).

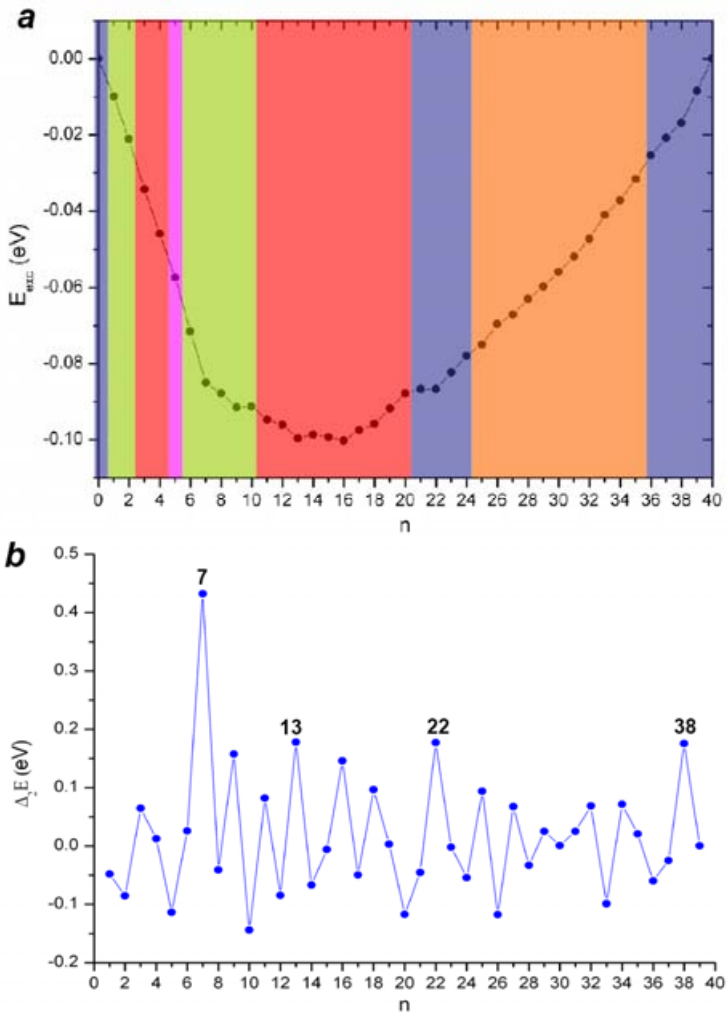


**Figure 6.1. (a)** Structural distribution coupled with excess energies for $Pt_nAu_{40-n}$ clusters at the empirical-potential level: bi-capped-TO motif (blue regions), inc-Ih-Mackay motif (green regions), c-pIh6 motif (magenta region), inc-dou-pc5 motif (red regions), c-Dh motif (orange region); **(b)** second differences in energy for $Pt_nAu_{40-n}$ clusters at the empirical-potential level.

The compositions n = 3, 4, and n = 11-20 (red regions) adopt the incomplete-double-5-fold-pancake motif (inc-dou-pc5) which is described here as a fraction of a wheel-like structure formed by the sticking of two 34-atom 5-fold pancakes (pc5) [159, 163]. The 34-atom 5-fold pancake is actually the (27,7) polyicosahedral structure which has a decahedral core of 7 atoms and the 27 surface atoms are placed in an anti-Mackay overlayer [159]. In previous work by Barcaro et al. [163] on 40-atom Cu-Ag and Cu-Au clusters, pc5-based

structures (capped-pc5) were found by performing Gupta – basin hoping Monte-Carlo (MC) GM searches but the inc-dou-pc5 structures were not reported. The inc-dou-pc5 structure for $Pt_{20}Au_{20}$ agrees with previous Gupta-BCGA searches performed by Logsdail et al. [267]. The capped-6-fold-pancake-polyicosahedral (c-pIh6) motif can only be found for n = 5 (magenta region). The structure for the $Pt_5Au_{35}$ cluster here is based on a 6-fold pancake (pc6) [159], having $C_s$ symmetry. Structures based on pc6 are rare in this work but more frequently found in works on 38-atom (Cu-Au) [268] (see Chapter 3) and 40-atom (Cu-Ag and Cu-Au) [163] clusters. For n = 25-35 (orange region), the capped-decahedral (c-Dh) motif is found. The c-Dh motif here is based on the geometry of a 39-atom Ino-decahedron having 10 rectangular (100) facets [180]. Generally, the c-Dh structures found in this study have $C_s$ symmetry; they are either a complete Ino-decahedron capped by a single atom or an incomplete decahedron capped by several atoms. It is noted that the c-Dh motif described by Barcaro et al. is based on the 23-atom decahedron [163].

The various structural motifs are presented in Figure 6.2 where the Gupta-GA GMs of $Au_{40}$, $Pt_4Au_{36}$, $Pt_5Au_{35}$, $Pt_7Au_{33}$, $Pt_{13}Au_{27}$, $Pt_{22}Au_{18}$, $Pt_{30}Au_{10}$, and $Pt_{40}$ are shown. $Au_{40}$ and $Pt_{40}$ adopt the distorted bi-capped-TO motif which still has a 6-atom octahedral core. These distorted structures are consistent with the tendency to amorphization observed in the previously studied Au and Pt clusters in which short ranged sticky interatomic potentials were used [181,182]. In contrast to the pure clusters, the bimetallic bi-capped TO clusters are not distorted. For example, $Pt_{22}Au_{18}$ has two capping Au atoms on two opposite (100) facets of an undistorted TO. For all bimetallic compositions, it is observed that Pt atoms occupy the cluster core and Au segregates to the cluster surface. This $Pt_{core}Au_{shell}$ tendency agrees with previous ab- initio studies of small Pt clusters [266] and (Gupta) empirical-potential Pt-Au clusters with up to 100 atoms [267]. There are some differences between the characteristics

of Au and Pt which favour the $Pt_{core}Au_{shell}$ configuration. The bulk cohesive energy of Pt (5.84 eV) is larger than that of Au (3.81 eV) [269], so the number of Pt-Pt bonds can be expected to be larger than the number of Au-Au bonds [9]. The surface occupation of Au is also expected to be energetically favoured because Au has a lower surface energy than Pt (96.8 meVÅ$^{-2}$ compared with 159 meVÅ$^{-2}$) [9]. The slightly smaller atomic radius of Pt (1.39 Å) compared with Au (1.44 Å) [9] may also favour the core location of Pt atoms.

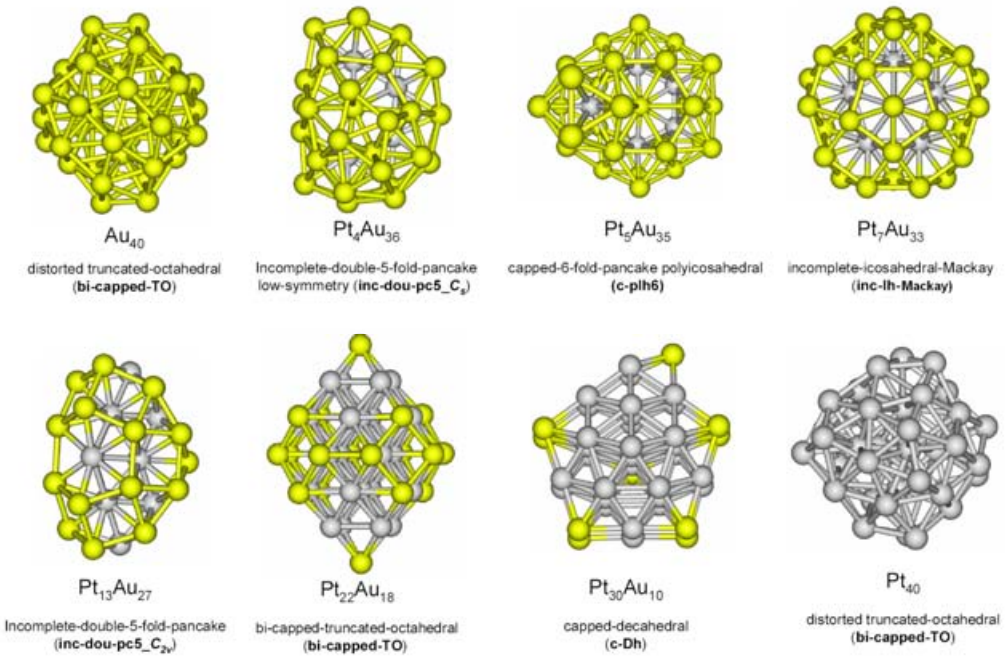


**Figure 6.2.** Different structural motifs found for $Pt_nAu_{40-n}$ clusters from the Gupta-BCGA searches.

## 6.3.2. Structural competition at the DFT level

For each composition of $Pt_nAu_{40-n}$, the DFT reoptimisation procedure was performed for different structural motifs found by using the Gupta-BCGA searches, including the GM motifs and other low energy motifs. The energy comparisons between different structural motifs after the DFT reoptimisation are shown in Figure 6.3. The predominance of the inc-

Ih-Mackay structures (green squares) in the Au-rich region (n = 1-10), which is predicted by the Gupta-BCGA searches, is confirmed at the DFT level. The c-pIh6 structures, which appear at n = 4-6 (magenta squares) are not found to be energetically favoured at the DFT level. For $Pt_5Au_{25}$, the c-pIh6 motif is much higher in energy than inc-Ih-Mackay, with an energy separation of 2.708 eV. This is consistent with the previous finding that c-pIh6 structures are energetically unfavourable at the DFT level for 40-atom Cu-Ag and Cu-Au clusters [163].

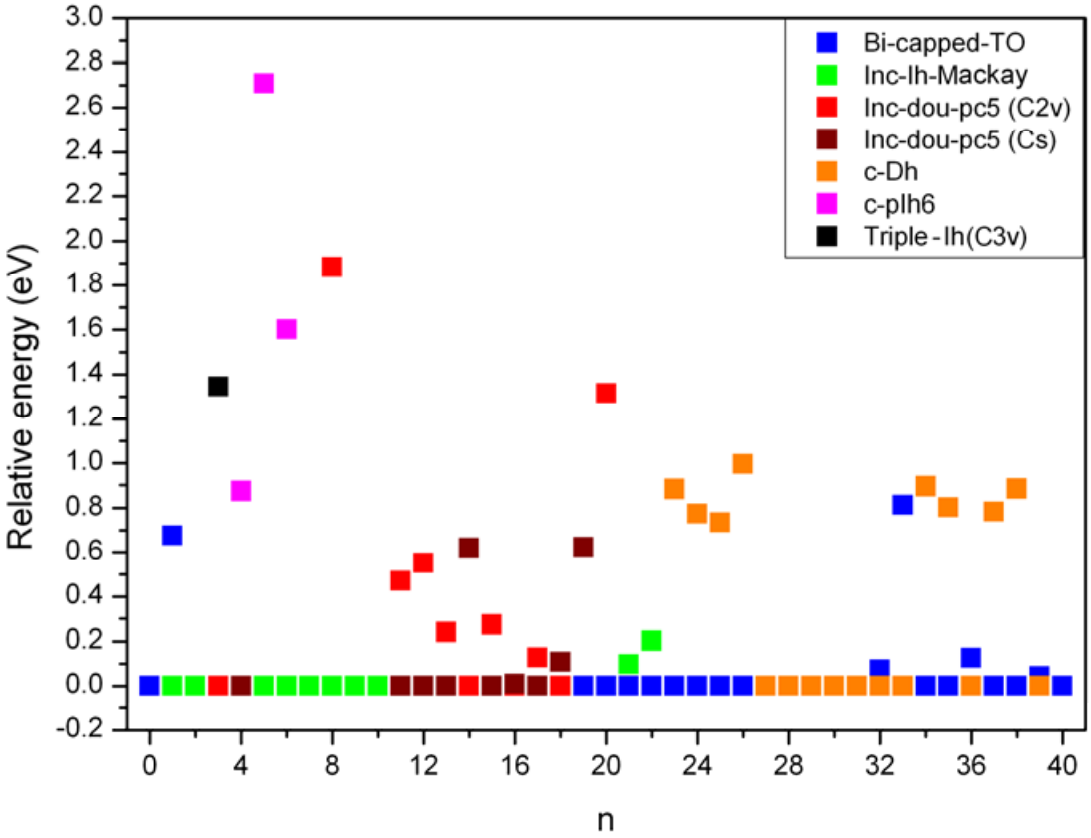


**Figure 6.3.** Comparisons in energy between different structures of $Pt_nAu_{40-n}$ clusters at the DFT reoptimisation level; the relative energy is the energy difference between each structure and the lowest-energy structure.

In the composition range n = 11-18, there is a competition between the two types of inc-dou-pc5 motif: with $C_{2v}$ symmetry (red squares) and with $C_s$ symmetry (brown squares). The energy separation between these types is generally small, especially in the case of $Pt_{16}Au_{24}$

where the $C_{2v}$ structure is only 0.009 eV lower than the $C_s$. The quasi-degeneracy in energy may be due to the weak amorphous tendency observed for Au-rich compositions [181,182,268]. The bi-capped-TO motif (blue squares) is favoured in the region n = 19-26 where the Pt:Au ratio is close to 1:1. In this region fcc-packing dominates, overcoming the amorphous tendency. The c-Dh motif (orange squares) was the only motif found from the Gupta-BCGA searches in the region n = 27-31 where there is no competition. For Pt-rich compositions n = 23-26 and n = 32-39, the bi-capped-TO and the c-Dh motifs compete. While the bi-capped-TO motif is favoured in the region n = 23-26, the competition between these two motifs causes some fluctuations in structural distribution in the range n = 32-39. A low energy separation (0.044 eV) between the bi-capped-TO and the c-Dh structures is observed for $Pt_{39}Au_1$.

There is a new polyicosahedral motif involved in the structural competition at n = 3. This motif is a triple icosahedron (triple-Ih) with $C_{3v}$ symmetry, constructed from three 13-atom icosahedra each having a Pt atom at its centre (see Figure 6.4). Although having a large HOMO-LUMO gap (0.489 eV), this polyicosahedral structure is 1.345 eV higher in energy than the inc-dou-pc5_$C_{2v}$ structure which has a smaller gap (0.218 eV).

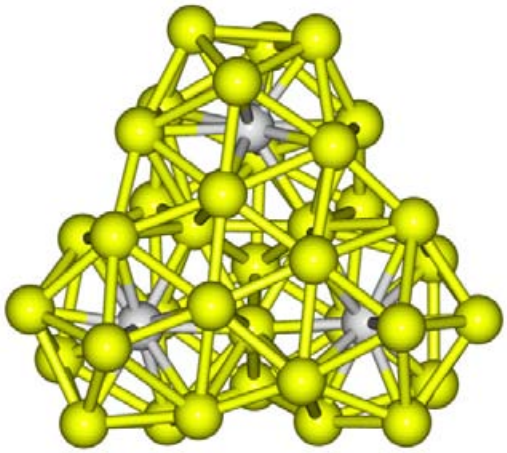

**Figure 6.4.** DFT-reoptimized triple-Ih structure of $Pt_3Au_{37}$ having a HOMO-LUMO gap of 0.489 eV.

### 6.3.3. Structural distribution and HOMO-LUMO gaps

The distribution of the lowest DFT energy structures coupled with the HOMO-LUMO gaps and the second differences in energy for all the compositions of $Pt_nAu_{40-n}$ clusters are shown in Figure 6.5a and Figure 6.5b, respectively. The structural distribution after the DFT reoptimisation includes four motifs: bi-capped-TO for n = 0, n = 19-26, and n = 34, 35, 37, 38, and 40 (blue regions); inc-Ih-Mackay for n = 1, 2 and n = 5-10 (green regions); inc-dou-pc5 for n = 3, 4 and n = 11-18; c-Dh for n = 27-33 and n = 36, 39 (orange regions).

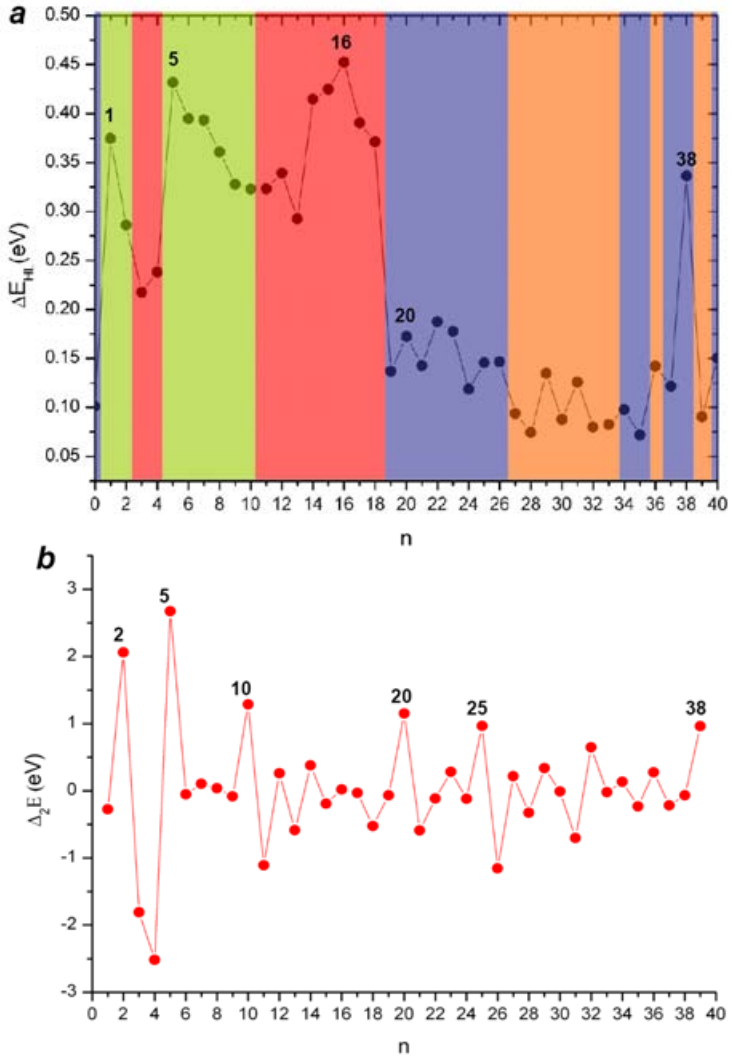


**Figure 6.5. (a)** Structural distribution coupled with HOMO-LUMO gaps for $Pt_nAu_{40-n}$ clusters at the DFT reoptimisation level: bi-capped-TO motif (blue regions), inc-Ih-Mackay motif (green regions), inc-dou-pc5 motif (red regions), c-Dh motif (orange region); **(b)** second differences in energy for $Pt_nAu_{40-n}$ clusters at the at the DFT reoptimisation level.

The HOMO-LUMO gaps are observed to be sensitive to structural motifs. While the bi-capped-TO and c-Dh structures generally have small gaps, the inc-dou-pc5 and inc-Ih-Mackay structures have large gaps. This is consistent with the calculations of HOMO-LUMO gaps in the work of Barcaro et al. [163] where pc5-based structures present large gaps while TO-based and Dh-based structures present small gaps. According to Barcaro et al., the large gaps of pc5-based structures indicate that electronic shell closure occurs for these structures and the small gaps of TO-based, pc6-based and Dh-based correspond to open electronic shells.

It was also shown that there is a complex interplay of geometric and electronic shell closure effects which cause some specific polyicosahedral structures (i.e., capped-pc5) to have high energetic stabilities and large HOMO-LUMO gaps. In our work, however, there is no pc5-based polyicosahedral structure having both geometric and electronic shell closures so the coexistence of a high energetic stability and large HOMO-LUMO gap is generally not expected. For example, some inc-dou-pc5 structures exhibit the electronic shell closure effect but they are incomplete structures having no geometric shell closure.

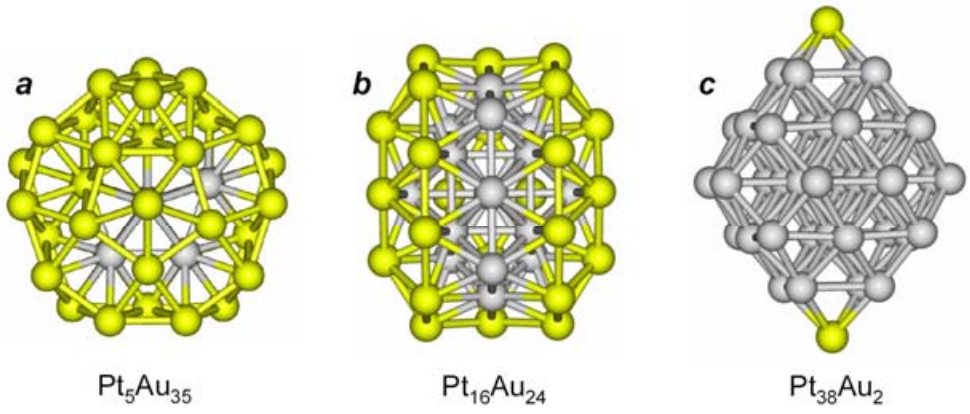


**Figure 6.6. (a)** inc-Ih-Mackay $Pt_5Au_{35}$ cluster having a HOMO-LUMO gap of 0.432 eV; **(b)** inc-dou-pc5 $Pt_{16}Au_4$ cluster having a HOMO-LUMO gap of 0.452 eV; **(c)** bi-capped-TO $Pt_{38}Au_2$ cluster having a HOMO-LUMO gap of 0.336 eV.

The high relative stabilities indicated by the energy differences (Figure 6.5b) generally do not correspond with high HOMO-LUMO gaps (Figure 6.5a), except for inc-Ih-Mackay $Pt_5Au_{35}$ and bi-capped-TO $Pt_{38}Au_2$ which have high relative stabilities and large gaps. The structures for $Pt_5Au_{35}$, $Pt_{16}Au_{24}$, and $Pt_{38}Au_2$ are presented in Figure 6.6a-6.6c. HOMO-LUMO gaps do not only depend on geometry but also on the relative arrangements of atoms [268], that is, high-symmetry homotops are expected to have higher gaps. This explains the particularly high gap of the inc-dou-pc5 $Pt_{16}Au_{24}$ (0.452 eV) and the abnormally high gap of the bi-capped-TO $Pt_{38}Au_2$ (0.336 eV). $Pt_{16}Au_{24}$ has a symmetrical arrangement of 16 Pt atoms forming the core and 24 Au atoms forming the shell (Figure 6.6b). The bi-capped-TO $Pt_{38}Au_2$ is a complete truncated octahedron of 38 Pt atoms with two Au atoms capping two opposite (100) facets (Figure 6.6c).

### 6.3.4. Configurations of $Pt_{20}Au_{20}$ at the DFT level

As mentioned above, the $Pt_{core}Au_{shell}$ configuration is found from the Gupta-BCGA searches as the energetically favoured configuration for $Pt_nAu_{40-n}$ clusters. However, the chemical ordering of these clusters must be tested again at the higher level of theory (i.e., DFT reoptimisation), because the Gupta potentials used in the BCGA are empirical [69] and the Pt-Au parameters are assumed to be averaged [267]. Although a previous DFT study performed on 13-atom clusters found a preference for surface Au atoms [266], the $Pt_{core}$-$Au_{shell}$ configuration has not been proven for every cluster size and structural motif. Logsdail et al. compared the binding energies calculated at the DFT level of the $Pt_{core}Au_{shell}$ and the (inverse) $Au_{core}Pt_{shell}$ configurations for $Pt_mAu_m$ (m = 1-10) and found that the $Pt_{core}Au_{shell}$ -configuration is more stable than the $Au_{core}Pt_{shell}$ for m = 6-10 [267]. The fluctuations of the

binding energy curves in Logsdail et al.'s work suggest that the favoured configuration might be altered for different cluster sizes and structural motifs.

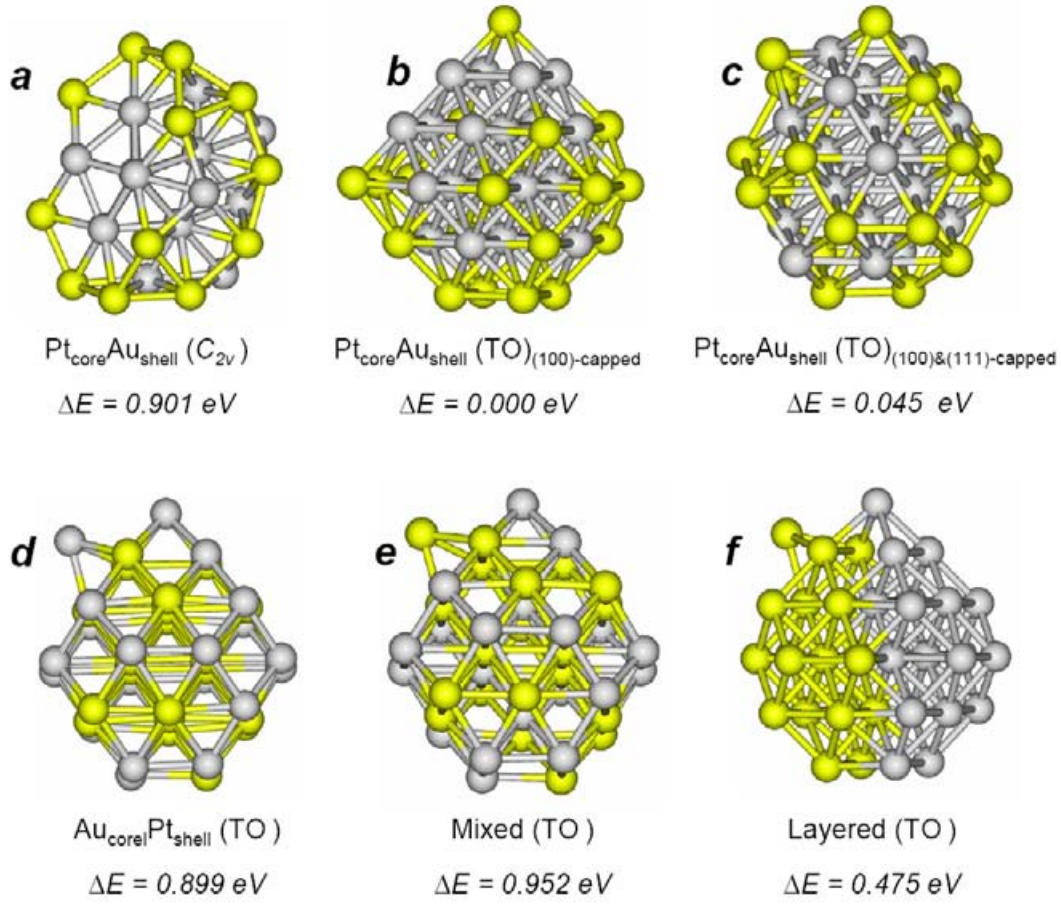


**Figure 6.7.** Energy comparisons between different DFT-optimized structures of $Pt_{20}Au_{20}$; $\Delta E$ is the energy difference from the lowest energy structure.

To investigate the configuration stability of our 40-atom Pt-Au clusters, we performed a case study of $Pt_{20}Au_{20}$ in which the energies of different configurations are compared after DFT reoptimisation. Six DFT-reoptimized structures for $Pt_{20}Au_{20}$ are shown in Figure 6.7: $Pt_{core}Au_{shell}$ configurations having the inc-dou-pc5_$C_{2v}$, and two different bi-capped-TO structures found from the Gupta-BCGA searches (Figures 6.7a, 6.7b, and 6.7c, respectively); Figure 6.7d, 6.7e, and 6.7f show three different homotops of the structure in Figure 6.7c, corresponding to three different configurations: $Au_{core}Pt_{shell}$, random mixed, and layered,

respectively. The DFT energies calculated for these six structures confirm that the bi-capped-TO $Pt_{core}Au_{shell}$ configuration which has two Au atoms capping on two (100) facets (Figure 6.7b) is the most energetically favoured. The energy separation between this (100)-capped $Pt_{core}Au_{shell}$ configuration and the others are listed in Table 6.2. It can be noted that, this configuration is slightly lower in energy (0.045 eV) than the other one which has both (100) and (111) facets as the capped sites (Figure 6.7c). This indicates the preference for Au capping on (100) facets in TO-based structures. The inc-dou-pc5_$C_{2v}$ $Pt_{core}Au_{shell}$ structure, with an energy separation of 0.901 eV, becomes unfavoured at the DFT level. The layered structure (Figure 6.7f), with an energy separation of 0.475 eV, turns out to be lower in energy than the $Au_{core}Pt_{shell}$ ($\Delta E$ = 0.899 eV), and mixed ($\Delta E$ = 0.952 eV) configurations, which is consistent with an experiment on Pt-Au clusters [30] and the low temperature phase segregation of Pt/Au in the bulk [258]. It can also be seen that the $Au_{core}Pt_{shell}$ configuration is slightly more favoured than the mixed configuration, suggesting that the segregation is stronger than the mixing.

**Table 6.2.** Relative energies, HOMO-LUMO gaps, and MPA charge sums of different structures of $Pt_{20}Au_{20}$.

| Structures of $Pt_{20}Au_{20}$ | DFT-optimized relative energy (eV) | HOMO-LUMO gap (eV) | Sum of Au atomic charges (\|e\|) | Total charge transfer (e) |
|---|---|---|---|---|
| $Pt_{core}Au_{shell}$ ($C_{2v}$) | 0.901 | 0.364 | 18.8 | 22.96 |
| $Pt_{core}Au_{shell}$ $(TO)_{(100)\text{-capped}}$ | 0.000 | 0.229 | 17.80 | 19.46 |
| $Pt_{core}Au_{shell}$ $(TO)_{(100)\&(111)\text{-capped}}$ | 0.045 | 0.180 | 19.09 | 20.89 |
| Mixed (TO) | 0.952 | 0.050 | 1.41 | 17.80 |
| $Au_{core}Pt_{shell}$ (TO) | 0.899 | 0.150 | -10.43 | 14.18 |
| Layered (TO) | 0.475 | 0.172 | 3.04 | 17.82 |

### 6.3.5. Mulliken population analysis

The DFT-calculated Mulliken charges for the Pt-Au dimer are -0.02 |e| for the Au atom and +0.02 |e| for the Pt atom. These charges, which result from the slight electron transfer from the lower to the higher electronegativity atom, are small as expected because the difference in the Pauling electronegativities between Au (2.4) and Pt (2.2) is small.

Although the polarization induced by the difference in electronegativities of Au and Pt is small, significant charge transfer, induced by geometrical structures [186,268], is also expected for $Pt_nAu_{40-n}$ clusters. We carried out Mulliken population analyses (MPA) for different structures of $Pt_{20}Au_{20}$ to investigate these charge transfers. Figure 6.8 shows plots of the Mulliken charge distributions of the four homotops corresponding to the four configurations of the (100)&(111)-capped TO $Pt_{20}Au_{20}$: $Pt_{core}Au_{shell}$ (Figure 6.8a), $Au_{core}Pt_{shell}$ (Figure 6.8b), mixed (Figure 6.8c), and layered (Figure 6.8d).

For the $Pt_{core}Au_{shell}$ configuration, the six Pt atoms forming the octahedral core are the most negatively charged (larger than -3 |e|) while all of the 20 Au atoms are positively charge and the surface Pt atoms are either nearly neutral or less charged. In the case of the $Au_{core}Pt_{shell}$ configuration, the six Au atoms of the octahedral core become the most negative ones because their charges are built up from most of the Au and Pt atoms on the surface. The mixed configuration has an octahedral core built from three Au atoms and three Pt atoms which are all negative. The three Pt atoms are significantly more negative than the three Au atoms, indicating that Pt is more electron-attractive than Au in this cluster structure.

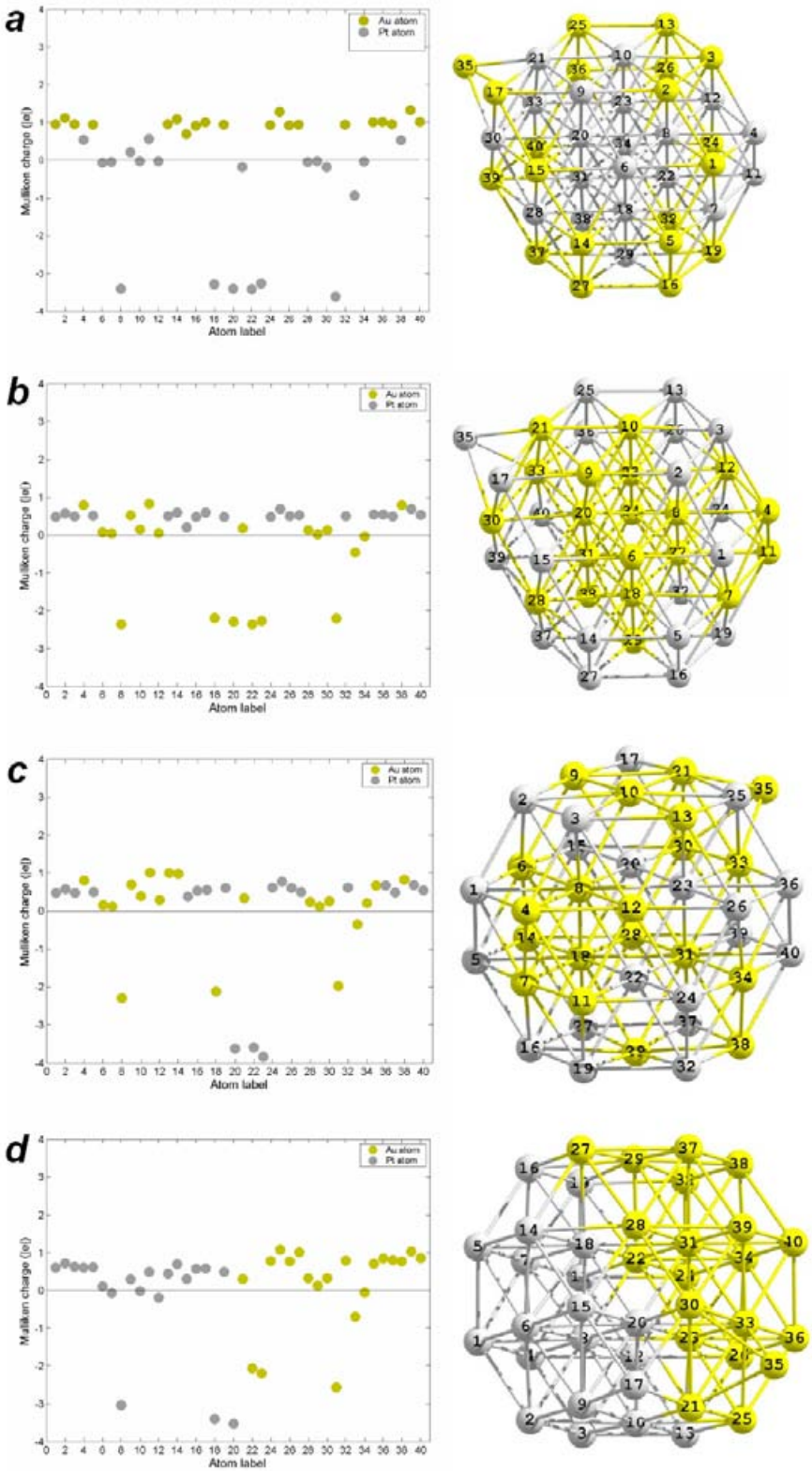


**Figure 6.8.** Mulliken charge distribution charts for different configurations of the $Pt_{20}Au_{20}$ (100)&(111)-capped-TO structures: **(a)** $Pt_{core}Au_{shell}$; **(b)** $Au_{core}Pt_{shell}$; **(c)** Mixing; **(d)** Layered

This is confirmed again in the case of the layered configuration where the three core Au atoms are less negative than the three core Pt atoms and the 17 surface Au atoms are, overall, more positive than the 17 surface Pt atoms. This apparently indicates that there is some amount of electron transfer from the Au layer to the Pt layer, contrasting with the charge transfer expected from the higher electronegativity of Au compared with Pt in the above Pt-Au dimer. We could evaluate the polarization of the layered cluster in which, overall, the Au layer has a charge of +3.04 |e| and the Pt has a charge of -3.04 |e| (see Figure 6.9). The algebraic sum of Au atomic charges and the total charge transfer for all four configurations are listed in Table 6.2.

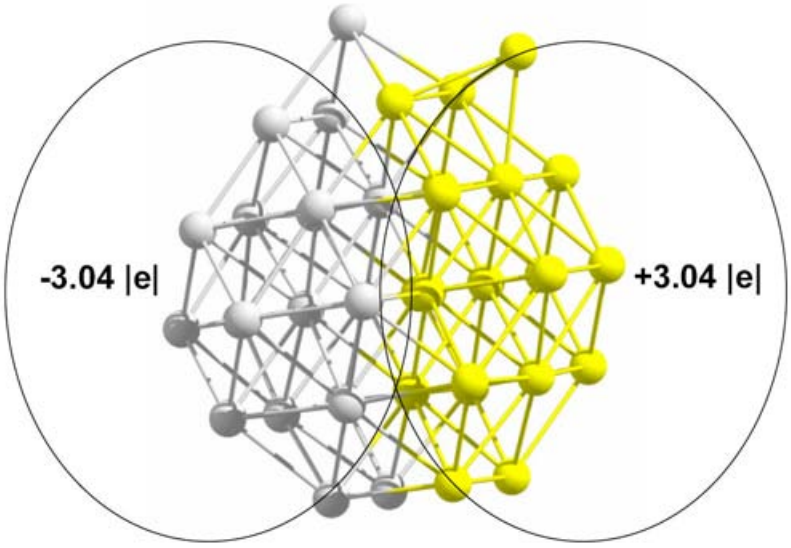


**Figure 6.9.** Polarization of the $Pt_{layer}Au_{layer}$ configuration for the $Pt_{20}Au_{20}$ (100)&(111)-capped-TO cluster; overall, -3.04 |e| is transferred from the Au layer to the Pt layer.

For all the configurations studied, negative charge is transferred from surface atoms to the core atoms. This geometrical charge transfer direction is the opposite of that in previous studies where negative charges were found to be transferred from the core atoms to the surface atoms in the cases of 13-atom icosahedral/cuboctahedral Au-Ag [186] and 38-atom

icosahedral/truncated-octahedral Cu-Au [268] clusters. This suggests that, the geometric charge transfer phenomenon may vary for different bimetallic systems.

It is observed that different surface sites have different charges. The eight centroid atoms on the eight hexagonal (111) facets, which are labeled with the numbers 6, 7, 10, 12, 28, 29, 33, and 34 (see Figure 6.8a-6.8d), are generally less positive than the remaining surface atoms, perhaps because they are compensated by negative charge transferred from the atoms lying at the six surrounding vertices of the hexagonal facets. Atom 33 is significantly negative in all the cases as it binds to the (111)-capping atom (labeled as 35). This agrees with a previous study where the Mulliken charge of each atom is observed to be complexly dependent on its local atomic environment [268]. The two vertex atoms labeled as 21 and 30 are also less positive, because they bind to the two capping 17-labeled and 35-labeled atoms (see Figure 6.8a for a clear view).

## 6.4. Conclusions

We have performed a study of 40-atom Pt-Au clusters using a combined empirical potential DFT approach. In this study, we have investigated the structural distributions coupled with energetic stabilities at both the level of the empirical potential (the Gupta potential – BCGA searches) and the DFT level. We have compared the DFT energies of different configurations ($Pt_{core}Au_{shell}$, $Au_{core}Pt_{shell}$, mixing, and $Pt_{layer}Au_{layer}$) to evaluate their stabilities. We also investigate the electronic shell closure effect of 40-atom clusters in terms of the calculations of HOMO-LUMO gaps for different structures and carried out MPA to study charge transfer phenomena.

At the EP level, we found inc-Ih-Mackay, inc-dou-pc5, bi-capped-TO, and c-Dh structural motifs predominating at different composition regions for $Pt_nAu_{40-n}$ clusters. The

$Pt_{core}Au_{shell}$ configuration was found to be favoured at this level, confirming the results from the previous Gupta-BCGA searches for $Pt_mAu_m$ (m = 1-50) [267].

At the DFT level, the c-pIh6 is confirmed to be less favoured, which is consistent with Barcaro et al.'s study of 40-atom Cu-Ag and Cu-Au clusters [163]. The amorphous tendency was found to be important for Au-rich and Pt-rich compositions while the fcc-packing tendency (TO-based structures) was found to be stronger at compositions close to 1:1 ratio.

Consistent with Barcaro et al.'s work, it is found that the electronic shell closure effects were observed in Inc-Ih-Mackay and inc-dou-pc5 structures which have large HOMO-LUMO gaps while bi-capped-TO and c-Dh structures have small gaps because of electronic shell opening. Large HOMO-LUMO gaps are also likely to be found for structures having highly symmetric atom arrangements, as in the case of inc-dou-pc5 $Pt_{16}Au_{24}$ and bi-capped-TO $Pt_{38}Au_2$.

After the DFT reoptimisations for different configurations of bi-capped-TO $Pt_{20}Au_{20}$ clusters, the $Pt_{core}Au_{shell}$ configuration is confirmed to be energetically favoured, compared with the $Au_{core}Pt_{shell}$ and mixed configurations. This is consistent with previous studies [266,267]. It is found that the two capping Au atoms of $Pt_{core}Au_{shell}$ structures prefer to cap the (100) facets. The layered configuration is found to be more stable than the mixed and $Au_{core}Pt_{shell}$ configurations, which is consistent with experiments [30,258]. Strong geometric charge transfers were observed from the MPA for different configurations of the (100)&(111)-capped-TO $Pt_{20}Au_{20}$ structures. Negative charge was found to be transferred from the surface atoms to the core atoms, contrary to previous studies [186,268]. In contrast to the Pt-Au dimer where there is some electron transfer from the Pt to the Au atom due to the higher electronegativity of Au, in the cluster structures, Pt atoms are more electron-attractive than Au atoms: especially, in the layered bi-capped-TO structure, Au atoms behave

as “electron donors” and Pt atoms as “electron acceptors.” The electron transfer phenomenon presented in this work remains unexplained, suggesting that further study of the charge transfer phenomena occurring in clusters should be carried out.

# CHAPTER 7. CHEMICALLY-SYNTHESIZED PLATINUM-GOLD NANOPARTICLES

**Abstract.** SDD-EDX elemental mapping and line-scanning are used to characterize bimetallic Pt-Au nanoparticles which are synthesized by two different wet-chemical methods. PVP-stabilized Pt-Au nanoparticles are synthesized by the polyol method while citrate-stabilized Pt-Au nanoparticles are synthesized via a citrate route (Frens method) succeeded by a Pt coating procedure (Schmid procedure). For the PVP-stabilized particles, we observe different configuration tendencies (homogeneously mixed, $Au_{core}Pt_{shell}$, and $Pt_{core}Au_{shell}$), Pt-Au interdiffusion, and the size-dependence of the Pt:Au atomic ratio. For the citrate-stabilized particles, we observe an $Au_{core}Pt_{shell}$ configuration and investigate the interdiffusion between the Au core and the Pt shell under the electron beam.

## 7.1. Literature review

In experimental studies of bimetallic nanoparticles, Pt-Au is among the most popular systems due to its promising catalytic capacity [9,30,259-263]. Bimetallic Pt-Au nanoparticles have a wide range of catalytic applications, including oxygen reduction in fuel cells [270], methanol and formic acid oxidations [271,272], and selective oxidation [273].

Bimetallic Pt-Au nanoparticles have been chemically synthesized either by co-reduction or successive reduction procedures (see Chapter 2: 2.2.1). Dodecanthiol-stabilized Pt-Au nanoparticles of around 2.5 ± 0.4 nm were made by reduction of $K_2PtCl_6$ and $HAuCl_4$ solutions [274]. Both $Au_{core}Pt_{shell}$ and $Pt_{core}Au_{shell}$ nanoparticles can be generated by radiolytic reduction of a solution containing Au and Pt salts [275,276]. The $Au_{core}Pt_{shell}$

arrangement resulted from a radiolytic co-reduction is explained by the fact that Au is nobler (easier to reduce) than Pt, and thus Au is likely to be reduced first, although the $Pt_{core}Au_{shell}$ configuration is energetically favoured by surface and cohesive energies [9] (see Chapter 6).

Garcia-Gutierrez et al. have used the polyol method with a successive reduction procedure (see Chapter 2: 2.2.1b) to synthesize PVP-stabilized bimetallic Pt-Au nanoparticles and investigate the effect of temperature on particle formation [110]. In their procedure, $H_2PtCl_6$ was added to a solution of PVP in ethylene glycol (EG) first and after a change in colour of the solution (from yellow to dark brown), $HAuCl_4$ was added. It was reported that both monometallic (Au and Pt) and bimetallic ($Au_{core}Pt_{shell}$ and $Pt_{core}Au_{shell}$) nanoparticles were produced by this method. They have found that at lower temperature (100$^o$C and 110$^o$C) the Au nucleation occurred faster than the Pt nucleation did and the formation of bimetallic structures was prevented by the interaction between Pt and PVP. However, at 120$^o$C, a balance between the reduction and nucleation rates of Au and Pt was observed. A few bimetallic particles were found at 120$^o$C, including both $Au_{core}Pt_{shell}$ (> 10 nm) and $Pt_{core}Au_{shell}$ (< 10 nm). At higher temperatures (130 – 190$^o$C), $Pt_{core}Au_{shell}$ were obtained and the thickness of the Au shell was found to increase with temperature. The same authors also reported that although the Z-contrast can not be exploited for Pt-Au systems ($Z_{Pt}$ = 78 and $Z_{Au}$ = 79), core-shell structures of Pt-Au nanoparticles can be revealed by HAADF-STEM due to the interfacial strain field caused by the mismatch in lattice parameters of Au (0.408 nm) and Pt (0.392 nm) [277].

Schmid et al. used a successive reduction procedure to prepare citrate-stabilized bimetallic Pt-Au particles (of around 18 nm in diameter) which are heterogeneous agglomerates with a large Au core loosely covered by small satellite Pt particles [13]. Braidy et al. followed Schmid's method to synthesize $Au_{core}Pt_{shell}$ particles (of around 20 nm in

diameter) and investigated the structural evolution of these particles by annealing them at different temperatures (300-800$^{o}$C) [30]. At lower temperatures (~300$^{o}$C) the Pt shell attached more firmly to the Au core and interdiffusion between the core and the shell occurred. At higher temperatures (600$^{o}$C and 800$^{o}$C), the core-shell configuration was replaced by a phase-segregated configuration in which Au-rich and Pt-rich layers are separated by an interface. Compared with the bulk Pt-Au system, the Au solubility in the Pt rich-phase at this temperature was found to be 5-10% higher, indicating a weak Pt-Au mixing tendency at the nano-scale. The phase-segregated configuration remained stable after 6 hrs annealing at 600$^{o}$C.

We report in this chapter our synthesis and characterization of bimetallic Pt-Au nanoparticles. We have synthesized bimetallic Pt-Au nanoparticles by two methods: the polyol method (following the procedure by Garcia-Gutierrez et al.) and Turkevich-Frens method (following the procedure by Schmid et al. and Braidy et al.). TEM, HAADF-STEM, and SDD-EDX elemental mapping were used to characterize the particles.

## 7.2. Experimental details

PVP-stabilized bimetallic Pt-Au nanoparticles were synthesized using the polyol method. In our experiment, PVP (0.8 g, molecular weight = 40000) was added to EG (100 ml). The mixture was stirred (with a magnetic stirrer) in a double-necked round-bottom flask until the PVP was completely dissolved. A solution of $H_2PtCl_6.6H_2O$ (0.1036g, 0.05 M) in UHQ (ultra high-purity) water (4 ml) was added to the EG-PVP solution. The mixture was stirred, heated for 30 minutes, until the temperature was 125$^{o}$C and the mixture turned from yellowish to dark brown. The solution of $HAuCl_4.3H_2O$ (0.1 M, 0.0768 g) in UHQ water (2

ml) was then added to the reaction mixture once it had turned dark brown. The newly-obtained mixture was heated to 140$^{o}$C and stirred at a speed of 600 rpm for 3 hrs.

Citrate-stabilized bimetallic Pt-Au nanoparticles were synthesized by Frens method combined with Schmid's successive procedure in which preformed citrate-stabilized Au nanoparticles were prepared first and then coated with Pt in $H_2PtCl_6$ solution. To prepare citrate-stabilized Au nanoparticles via the Frens method, an aqueous solution of $HAuCl_4$ (0.002 M, 50ml) was heated under air reflux for 10 minutes. An aqueous solution of sodium citrate (1ml, 8 wt.%) was then added to the $HAuCl_4$ solution. The newly-obtained solution continued to be heated (around 100$^{o}$C) under reflux for a further 5 minutes. The obtained red mixture was left to cool while being stirred for 1 hr. After that, the mixture was centrifuged at 3500 rpm for 10 minutes and the supernatant liquid was collected as a dispersion of citrate-stabilized Au nanoparticles (Au sol). To coat the Au nanoparticles with Pt, the Au sol (9.6 ml) was mixed with $H_2PtCl_6$ aqueous solution (0.0002 M, 10 ml) and ascorbic acid solution (1.76 wt.%, 1.5 ml). The mixture was stirred for 90 minutes in an ice bath. A dark brown mixture was obtained of a dispersion of bimetallic agglomerates with Au cores surrounded by Pt precipitation.

Both the PVP-stabilized and citrate-stabilized Pt-Au nanoparticles were deposited on amorphous carbon thin film and characterized using TEM, HAADF-STEM, and SDD-EDX techniques which are based on a field emission gun Tecnai F20 microscope operating at 200 kV. In HAADF-STEM mode: C2 = 30 μm; spot size = 8; probe size < 1 nm; inner collection semi-angle = 40 mrad. Elemental mapping and line-scanning were performed in HAADF-STEM mode using an *Oxford Instruments* X-Max SDD (see Chapter 2: 2.3.4) with a collection solid angle of around 1.3 srad. The specimens were tilted to 25 degrees. INCA

software with a drift-correcting function (*SiteLock*$^{TM}$) was used to control and process the mapping and line-scanning.

## 7.3. Results and discussion

### 7.3.1. PVP-stabilized Pt-Au nanoparticles

Two size ranges for the PVP-stabilized Pt-Au nanoparticles synthesized by the polyol method are observed: small particles of around 1-8 nm in size (Figure 7.1a) and large particles having sizes larger than around 15 nm (Figure 7.1b). Figure 7.1a shows a TEM image of the small nanoparticles and the corresponding size histogram (inset). These particles are quite monodisperse with 3-4 nm particles being most frequent, although particles having other sizes can occasionally be found. This size distribution is consistent with the PVP-stabilized Pt-Au nanoparticles previously reported by Garcia-Gutierrez et al. [277].

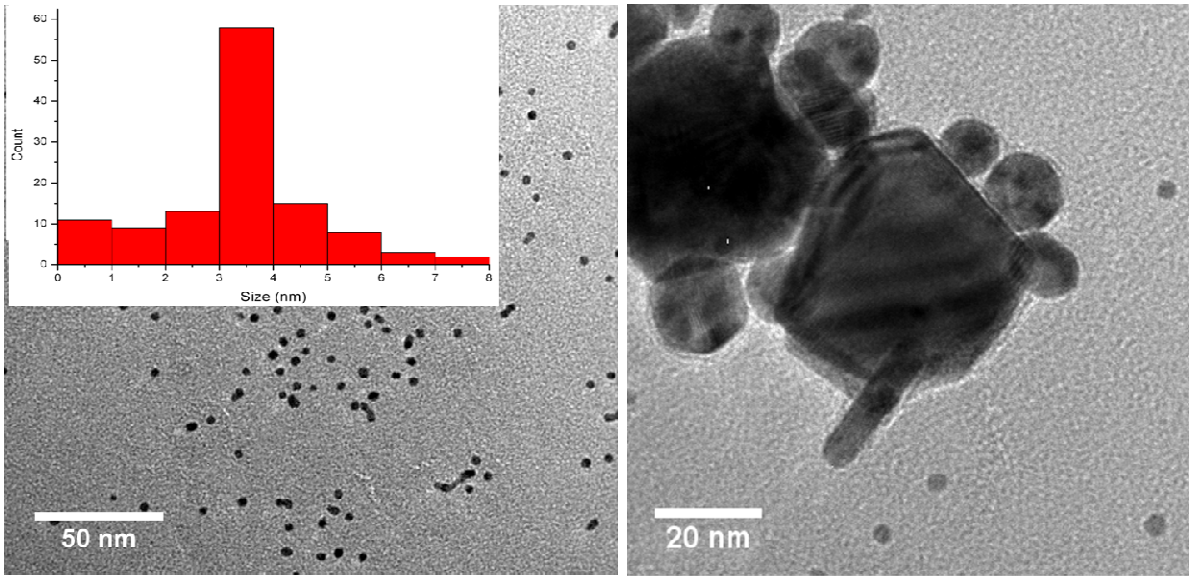


**Figure 7.1.** Two size ranges of PVP-stabilized Pt-Au nanoparticles observed by TEM: **(a)** image of small particles with the corresponding size histogram (inset); **(b)** image of large particles having different shapes (including nanorods).

Various shapes and sizes are observed for the large particles which are shown in Figure 7.1b. These particles often have well-defined shapes, including cuboctahedral, rounded, and rod-like (nanorod) shapes. According to previous study [110], these large particles may be Au-rich. The existence of polyhedral particles and nanorods can be attributed to the interaction between Au and PVP [279].

Although the configurations of Pt-Au nanoparticles can not be revealed via the weak Z-contrast, it was suggested by Garcia-Gutierrez et al. that a strain field in the Pt-Au interface, which is produced by 3.92% lattice mismatch between Au and Pt, can induce a different type of contrast (strain field contrast) in HAADF-STEM. Strain field contrast which depends on particle orientation can be exploited to reveal core-shell structures of Pt-Au nanoparticles [277]. Garcia-Gutierrez et al. reported that brighter cores and darker shells (with a great difference in intensity) were observed via the strain field contrast of core-shell Pt-Au particles. This contrast was also observed to change when the specimen was tilted. However, we did not observe strain field contrast in HAADF-STEM images of our Pt-Au particles (Figure 7.2) even when our specimen was tilted to different angles.

Figure 7.2a shows an HAADF image of small Pt-Au particles. They exhibit bright spots with thin darker edges which did not change significantly when the specimen was tilted to a different angle. The contrast between the bright spots and their darker edges can be attributed to thickness contrast and Z-contrast between the heavy elements (i.e., Au and Pt) and the capping PVP molecules. In the case of a particle of around 12 nm (Figure 7.2b), only weak contrast is observed between the centre part and the outer part of the particle image, which can be attributed to thickness contrast because HAADF intensity depends linearly on thickness.

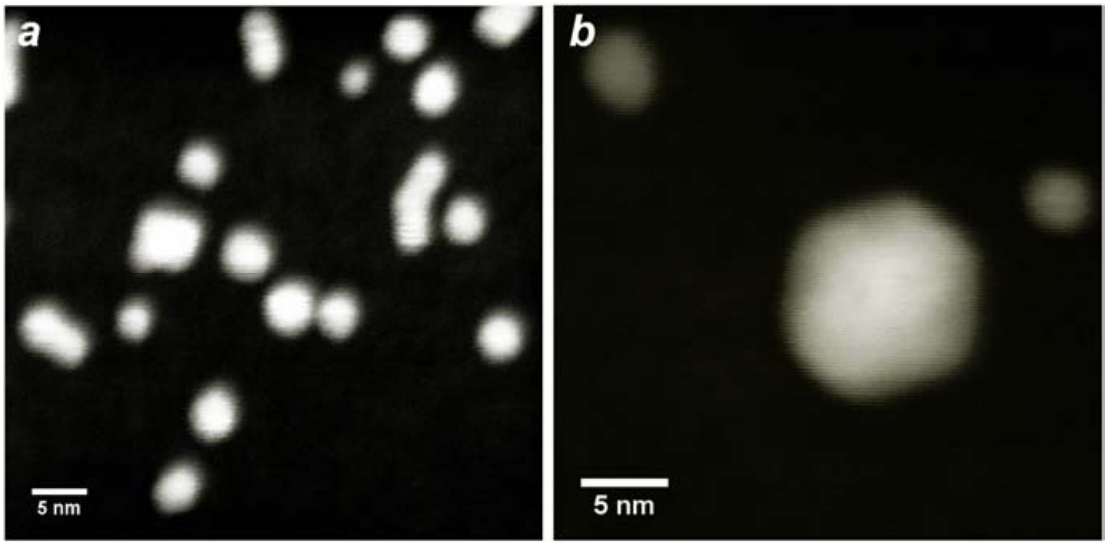


**Figure 7.2**. HAADF-STEM images of Pt-Au nanoparticles: **(a)** small particles which do not exhibit strain field contrast; **(b)** a particle of around 12 nm in size, in which only thickness contrast is observed.

There are two possible reasons explaining the absence of strain field contrast in the present HAADF images (Figure 7.2) of our Pt-Au particles. The first reason is that the particles do not have core-shell configurations or any other kind of segregation between Au and Pt. In other words, the particles are not heterogeneous enough to have Pt/Au interfaces which induce a strain field. Garcia-Gutierrez et al. also reported that some of their particles never showed a core-shell structure even when tilted to different angles. They were believed to be either Pt-Au alloy particles or monometallic particles [277]. The second reason is that electron scattering is sensitive to the orientation of the particle crystal. Strain field contrast only dominates when HAADF images are observed under zone axis orientations (dynamic conditions) [277,279]. If the particles do not have well-established crystalline structures with zone axes, strain field contrast is not expected. Actually, the nature of strain field contrast in HAADF-STEM images of heterogeneous nanoparticles has not been explicitly elucidated because of complicated interfacial structures. Moreover, strain field contrast may interfere in

a complex way with Z-contrast and thickness contrast, causing difficulties in determination of particle configuration.

Ambiguities in HAADF-STEM images of heterogeneous nanoparticles can be resolved by elemental mapping. We show here SDD-EDX elemental mapping of the Pt-Au particles of different sizes. Figure 7.3 shows the elemental mapping of a small particle having a size of around 4 nm. No strain field contrast is observed in the HAADF image (Figure 7.3a) of this particle. The X-ray signals corresponding to the $L_\alpha$ transitions of Pt and Au (Figure 7.3b and 7.3c) suggest that the particle is homogeneously Pt-Au mixed. The Pt:Au atomic ratio estimated by EDX analysis for the particle is approximately 2.45, suggesting that the small particles are Pt-rich. It was reported by Garcia-Gutierrez et al. that particles smaller than 3 nm are often monometallic Pt particles.

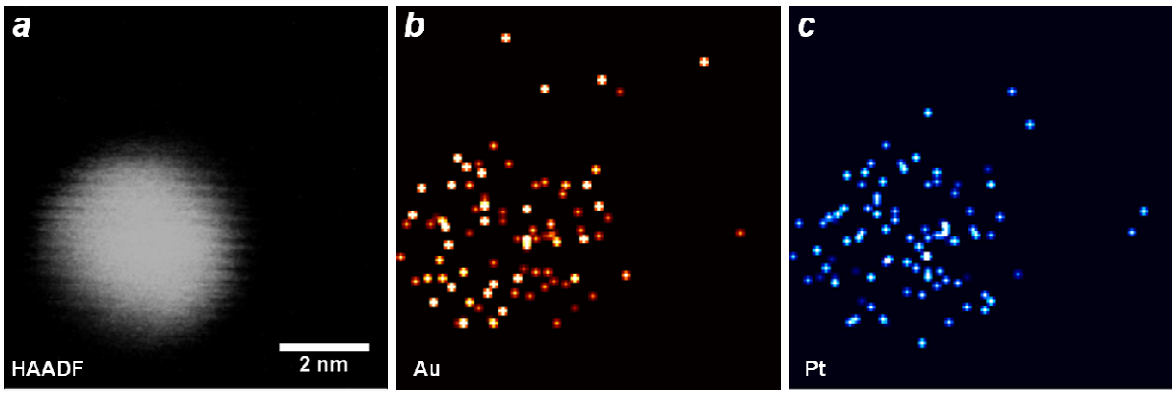


**Figure 7.3.** SSD-EDX mapping of a 4 nm Pt-Au particle: **(a)** HAADF image; **(b)** $L_\alpha$ X-ray signal of Au; **(c)** $L_\alpha$ X-ray signal of Pt; the estimated Pt:Au atomic ratio is approximately 2.45.

The elemental mapping of a larger particle (~ 8 nm) is shown in Figure 7.4. Although the HAADF image (Figure 7.4a) has only thickness contrast, the X-ray signals of Au and Pt (Figure 7.4a and 7.4b) indicate that the particle is heterogeneous. A Pt-rich region is observed at the upper side (Figure 7.4c) while the Au distribution (Figure 7.4b) corresponds

to the middle of the particle. This suggests segregation between Au and Pt in which a Pt-rich layer incompletely covers the particle surface, indicating an $Au_{core}Pt_{shell}$ tendency. Despite that, interdiffusion between Pt and Au is still observed, consistent with the Au solubility in the Pt-rich phase of nanoparticles being higher in comparison with the bulk system [30]. The estimated Pt:Au atomic ratio for this particle is approximately 0.45.

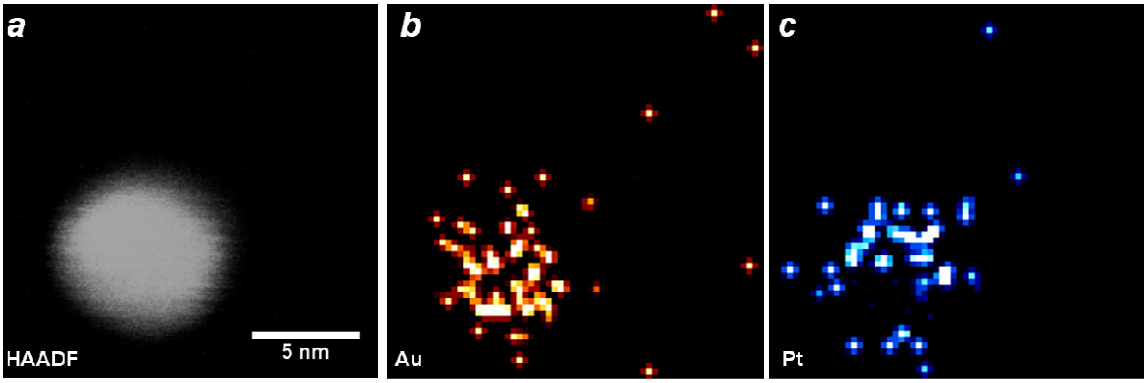


**Figure 7.4.** SDD-EDX mapping of a 8 nm Pt-Au nanoparticle: **(a)** HAADF image; **(b)** $L_\alpha$ X-ray signal of Au; **(c)** $L_\alpha$ X-ray signal of Pt; the estimated Pt:Au atomic ratio is approximately 0.45.

The elemental mapping of a particle of around 12 nm in size is shown in Figure 7.5. There is a small Pt-rich region observed in the Pt map (Figure 7.5c) while the Au signal is observed to be high over the remaining particle area (Figure 7.5b). The high- intensity Pt signal correlates with the low-intensity Au signal, indicating segregation between Au and Pt. The particle is determined to be a heterogeneous particle with a small off-centre Pt-rich core and a thick asymmetric Au-rich shell. However, only thickness contrast is observed in the HAADF image (Figure 7.5a) of the particle because the Z-contrast is negligibly weak and strain field contrast is absent (dynamic conditions are not met in this case). The off-centre behaviour of the Pt-rich core can be attributed to asymmetric capping activity of PVP molecules on the Pt seed, which causes an anisotropic Au deposition. The estimated Pt:Au atomic ratio for this 12 nm particle is approximately 0.10.

It is noted that different particles of around 4 nm and around 8 nm were examined by elemental mapping: the smaller particles are frequently observed to be Pt-Au mixed while the larger particles are frequently observed to be heterogeneous.

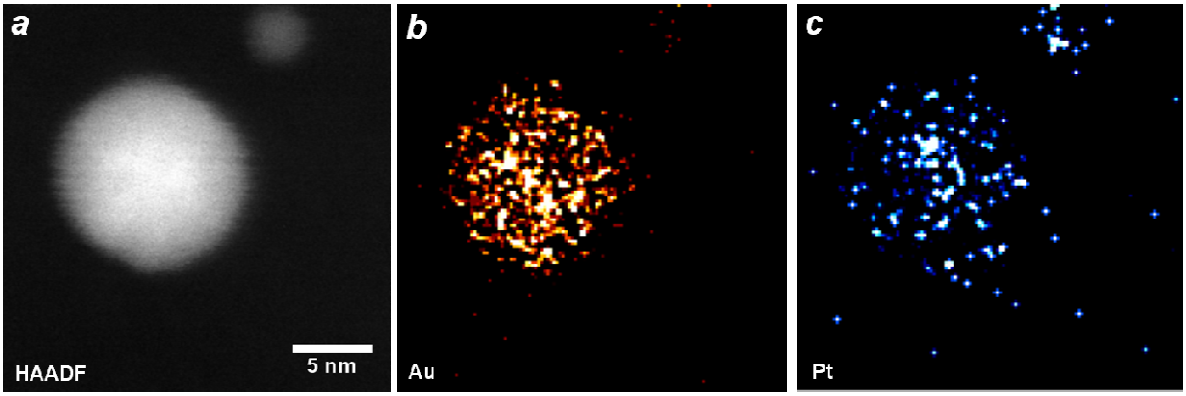


**Figure 7.5.** SDD-EDX mapping of a 12 nm Pt-Au nanoparticle: **(a)** HAADF image; **(b)** $L_\alpha$ X-ray signal of Au; **(c)** $L_\alpha$ X-ray signal of Pt; the estimated Pt:Au atomic ratio is approximately 0.10.

The Pt:Au atomic ratios for the three different particle sizes are listed in Table 7.1. The Pt concentration decreases and the Au concentration increases when the particle size increases. According to Garcia-Gutierrez et al.[110], at low temperatures (< 120$^o$C), although small Pt seeds are reduced first, the Au reduction rate is higher than the Pt reduction rate and the strong interaction between PVP and Pt prevents Au and Pt from forming bimetallic structures. At higher temperatures (> 120$^o$C), the Pt redox potential is close to the EG oxidation potential, making Pt reduction and nucleation rates comparable with Au. The high temperatures also weaken the Pt-PVP interaction and thus allow the coalitions of metallic atoms which induce the formation of bimetallic structures.

The temperature in our experiment was high enough (140$^o$C) for the formation of bimetallic nanoparticles. The Pt-richness of small particles and the Au-richness of large particles can be explained. Because $H_2PtCl_6$ was added to the reducing EG first and the Pt

reduction rate was competitively high (the temperature was sufficiently high), small Pt seeds were nucleated first and stabilized by PVP, lowering the Pt ion and PVP concentrations in the reaction mixture. After adding $HAuCl_4$, the concentration of Au ions is dominantly high while the PVP concentration is low, causing the formation of Au-rich large particles. It is noted that the $H_2PtCl_6$:$HAuCl_4$ molar ratio added to our reaction mixture was 1:1.

**Table 7.1.** Pt:Au atomic ratios for PVP-stabilized Pt-Au nanoparticles of different sizes.

| **Particle size** | 4 nm (Figure 7.3) | 8 nm (Figure 7.4) | 12 nm (Figure 7.5) |
|---|---|---|---|
| **Pt:Au ratio** | 2.45 | 0.45 | 0.10 |

It is observed in our results that the high temperature enhances the Pt-Au interdiffusion in small particles, causing homogeneous mixing as found in the case of the 4 nm particle (Figure 7.3). This is consistent with Pt-Au nanoparticles of 3-6 nm in size synthesized by Miner et al. [113], which were found to be homogeneously mixed. However, the existence of the $Au_{core}Pt_{shell}$ tendency found for the 8 nm particle (Figure 7.4) indicates that, in some cases, the Pt-PVP interaction at 140$^{o}$C (compared with the threshold of 120$^{o}$C) may still be strong enough to drive Pt out to the particle surface. The $Pt_{core}$-$Au_{shell}$ tendency found for the 12 nm particle (Figure 7.5), which is energetically favoured by the higher surface and cohesive energies of Pt (see Chapter 6), is consistent with Garcia-Gutierrez et al.'s experiment [110].

## 7.3.2. Citrate-stabilized Pt-Au nanoparticles

Our citrate-stabilized Pt-Au nanoparticles which are shown in Figure 7.6 are high-monodispersity heterogeneous agglomerates with Au cores of around 20 nm surrounded by

small satellite Pt aggregates of around 3-4 nm. This kind of agglomerate has been reported previously [13,30]. For example, Schmid et al. reported that their Pt-Au agglomerates which were synthesized via the citrate route and stabilized by $H_2NC_6H_4SO_3Na$ have Au cores of around 18 nm and satellite Pt aggregates of around 5 nm.

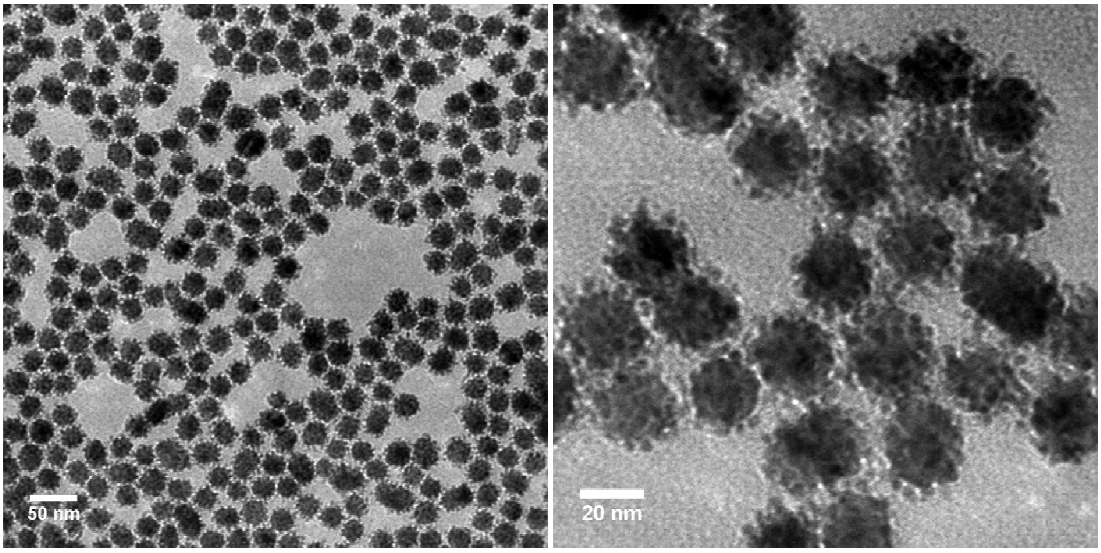


**Figure 7.6.** Citrate-stabilized Pt-Au nanoparticles which have large Au cores surrounded by small satellite Pt aggregates.

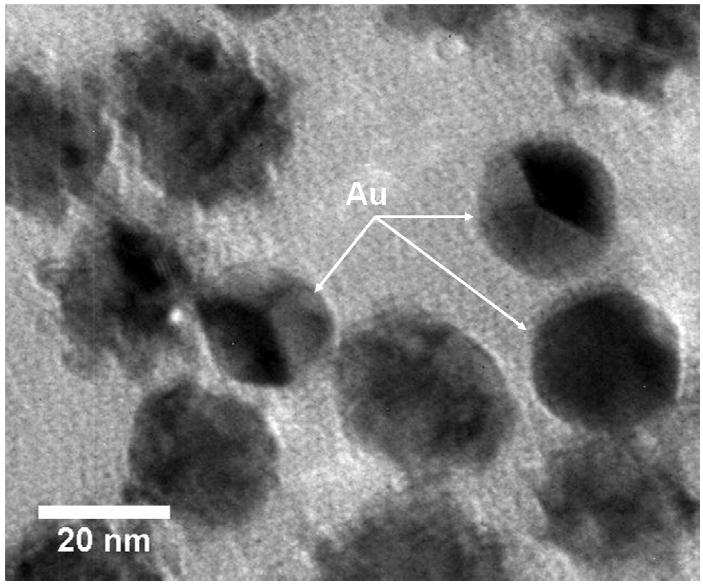


**Figure 7.7.** Citrate-stabilized Pt-Au and Au nanoparticles: the monometallic Au particles can be distinguished from the bimetallic agglomerates.

We observe that not every Au particle was coated with Pt. Figure 7.7 shows some monometallic Au particles without surrounding Pt, which can be distinguished from the bimetallic agglomerates.

The loose Pt attachment to the Au core can be interpreted via the higher cohesive energy of Pt (compared with Au) which favours Pt-Pt binding (see Chapter 6). Moreover, the Pt reduction occurred at low temperature (we carried out the Pt reduction in an ice bath) so the mobility of Pt atoms was low and Pt-Au interdiffusion was not expected.

When stimulated by an adequate dose (C2 = 150 µm, extraction voltage = 4200 V) of electron irradiation in TEM, the coating Pt aggregates were observed to fuse to each other and bind more strongly to the Au core, resulting in a well-defined $Au_{core}Pt_{shell}$ configuration. The elemental mapping of such an $Au_{core}Pt_{shell}$ particle is shown in Figure 7.8.

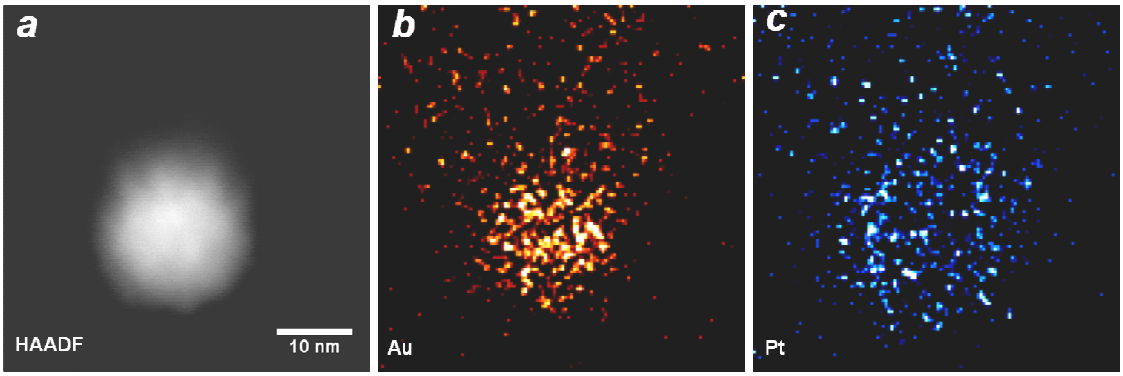


**Figure 7.8.** SDD-EDX mapping of a citrate-stabilized $Au_{core}Pt_{shell}$ nanoparticle: **(a)** HAADF image; **(b)** $L_\alpha$ X-ray signal of Au; **(c)** $L_\alpha$ X-ray signal of Pt; the estimated Pt:Au atomic ratio for the particle is approximately 0.87.

The HAADF image of the particle is shown in Figure 7.8a. The less bright outer edge can be attributed to the bumpy morphology of the Pt shell (the mass-density along the beam direction is low) which results from the fusion of the coating Pt aggregates. The Au X-ray signal shown in Figure 7.8b correlates well with the centre of the particle (Figure 7.8a). Figure 7.8c shows the Pt X-ray signal, confirming the Pt shell of the particle. The signal

regions of Au and Pt which are away from the particle (the upper parts of the Au and Pt maps) can be attributed to a trace of contamination left by the particle during its drift. The estimated Pt:Au atomic ration for the particle is approximately 0.87.

Figure 7.9 shows the elemental line-scanning for another $Au_{core}Pt_{shell}$ particle. The HAADF image marked with the scan line is shown in Figure 7.9a. The elemental scan was performed from left to right. The X-ray signal intensities along the line (from left to right) are shown in Figure 7.9b. The Au intensity (cyan line) peaks at the middle of the particle while the Pt intensity (red line) peaks at two opposite sides. The relatively high symmetry of the Pt and Au intensities supports the idea that the Au core is symmetrically coated by the Pt shell. From the rapid decrease of the Au intensity at the particle edges, the thickness of the Pt shell can be estimated to be roughly 2 nm. The particle has an estimated Pt:Au atomic ratio of approximately 0.97.

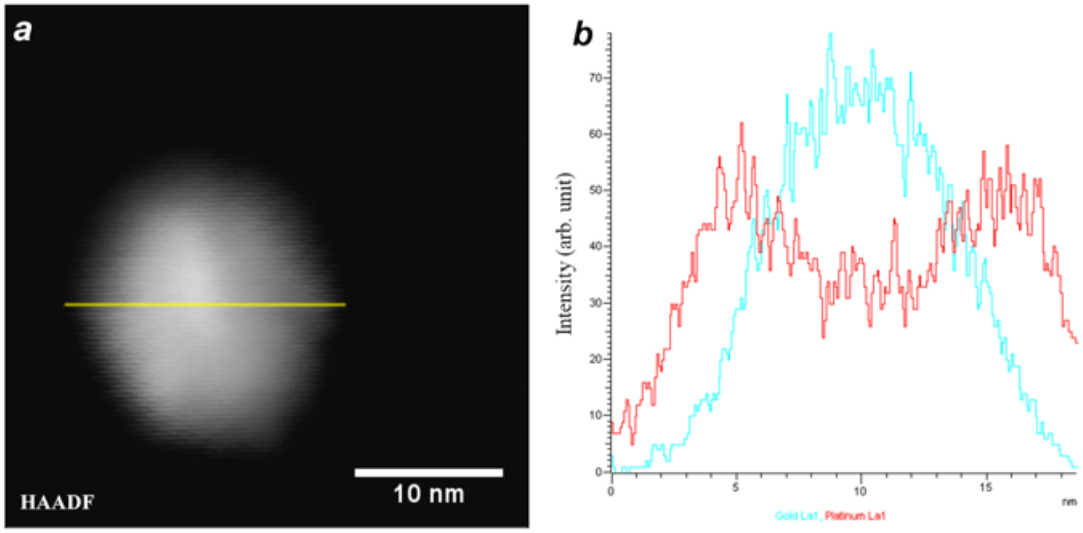


**Figure 7.9.** SDD-EDX line-scanning of a citrate-stabilized $Au_{core}Pt_{shell}$ nanoparticle: **(a)** HAADF image marked with a left-to-right scan line; **(b)** X-ray signal intensities of Pt (red line) and Au (cyan line); the estimated Pt:Au ratio for the particle is approximately 0.97.

The $Au_{core}Pt_{shell}$ configuration was previously found to be changed to a layer-segregated configuration when the particles were annealed at 600$^{o}$C [30]. We also observed changes in

the morphology and configuration of our particles under a strong electron beam. We used a high electron current (large condenser aperture C2 = 150 μm, extraction voltage = 4400 V) to irradiate the particles, which can cause an effect equivalent to thermal annealing at around 200°C [210-212]. Figure 7.10 shows the elemental mapping and line-scanning of a particle after an electron beam treatment for around 30 minutes.

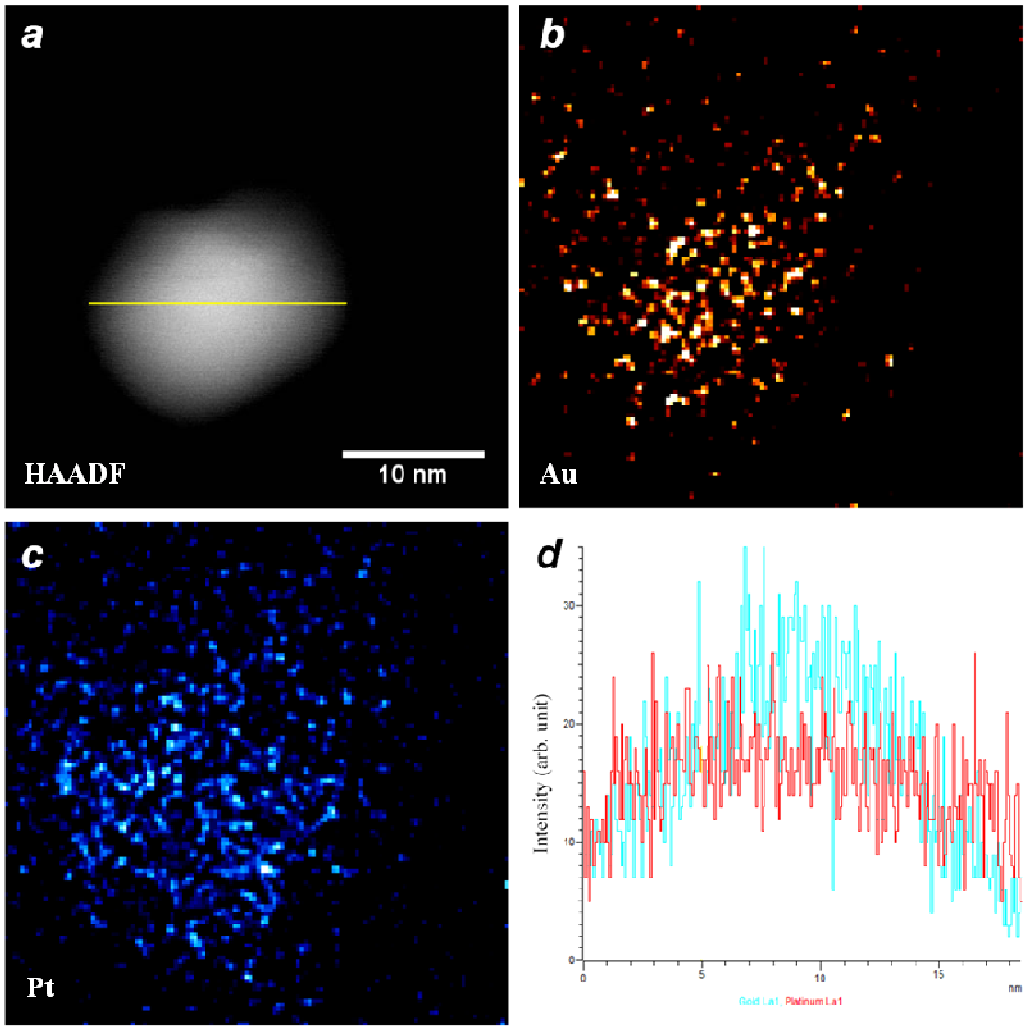


**Figure 7.10.** SDD-EDX mapping and line-scanning of a citrate-stabilized Pt-Au nanoparticle after an electron beam irradiation for around 30 minutes: **(a)** HAADF image marked with a left-to-right scan line; **(b)** $L_\alpha$ X-ray signal of Au; **(c)** $L_\alpha$ X-ray signal of Pt; **(d)** X-ray signal intensities of Pt (red line) and Au (cyan line) along the scanning line (from left to right); the estimated Pt:Au atomic ratio for the particle is approximately 1.16.

The particle shape was initially close to round (as commonly observed in Figure 7.6) but it became distorted and asymmetric after the electron beam treatment (Figure 7.10a). Although the electron beam effect (equivalent to 200$^{o}$C) was insufficient for a radical change in configuration as observed in the case of Pt-Au particles annealed at 600$^{o}$ and 800$^{o}$C [30], interdiffusion between the Au core and the Pt shell can be observed in the Au (Figure 7.10b) and Pt (Figure 7.10c) maps, being consistent with the observation of the 300$^{o}$C-annealed Pt-Au particles [30]. The interdiffusion is also confirmed by the Au and Pt intensities along the scanning line (Figure 7.10d). The electron beam also causes a contamination of Pt and Au in the carbon region surrounding the particle. That is the region why the X-ray signal areas of Pt and Au appear to be larger than the HAADF signal area of the particle. The estimated Pt:Au atomic ratio for the particle is approximately 1.16.

## 7.4. Conclusions

We have reported in this chapter TEM observations and SDD-EDX elemental mapping/line-scanning of bimetallic Pt-Au nanoparticles synthesized by two different wet-chemical methods: the polyol method and the citrate method.

Homogeneously mixed, $Au_{core}Pt_{shell}$, and $Pt_{core}Au_{shell}$ tendencies are found for different sizes of the PVP-stabilized Pt-Au particles synthesized at 140$^{o}$C by the polyol method. Strong Pt-Au interdiffusion is observed for small particles, which is the reason for an observed homogeneously mixed particle of around 4 nm. The temperature and the strong Pt-PVP interaction play important roles in the formation of bimetallic configurations. An $Au_{core}Pt_{shell}$ tendency is found for a particle of around 8 nm while a $Pt_{core}Au_{shell}$ tendency is found for a larger particle (~12 nm). Although these particles are heterogeneous, the Pt-Au interfacial strain field contrast is not observed. The Pt:Au atomic ratio for the particles is

observed to decrease dramatically when the particle size increases. In other words, the small particle (~4 nm) is found to be Pt-rich while the larger particles (~ 8 and 12 nm) are found to be Au-rich.

The citrate-stabilized Pt-Au nanoparticles synthesized by the Frens method (the citrate method) combined with a successive Pt coating procedure are heterogeneous agglomerates with large Au cores (~20 nm) surrounded by small satellite Pt aggregates (~ 3-4 nm). These agglomerates can be rearranged to be well-defined $Au_{core}Pt_{shell}$ particles when stimulated by an adequate electron dose. However, the $Au_{core}Pt_{shell}$ particles are found to be unstable under a further electron treatment (a strong electron irradiation for around 30 minutes) which induces morphological change and strong interdiffusion between the Au core and the Pt shell.

The difference between the PVP-stabilized Pt-Au particles and the citrate-stabilized Pt-Au particles can be attributed to the difference between the two methods. The particles from the polyol method are stabilized by steric effects while the particles from the citrate method are stabilized by the electrostatic repulsion [8]. Moreover, the interaction between Pt and Au in the polyol method was at ~ $140^{o}$C while in the Pt-coating procedure for the citrate-stabilized Au particles, the temperature was much lower (~ $0^{o}$C).

# CHAPTER 8. CONCLUSIONS AND FUTURE WORKS

## 8.1. Conclusions

In this thesis, we have reported computational and experimental studies of bimetallic Cu-Au, Pd-Au, and Pt-Au nanoparticles. We have theoretically studied structures, energetic stability, HOMO-LUMO gaps, and charge transfer of 38-atom Cu-Au clusters and 40-atom Pt-Au clusters using the Gupta-BCGA combined with DFT calculations. We have characterized the chemically synthesized Cu-Au and Pt-Au nanoparticles and the microbially synthesized Pd-Au nanoparticles using TEM techniques.

TO, inc-Ih-Mackay, pIh6, and amorphous-like structural motifs are found by the Gupta-BCGA for different compositions of $Cu_{38-n}Au_n$ clusters. The TO motif which predominates for Cu-rich compositions is distorted when having more than 8 Au atoms. The TO motif also exhibits a clear $Cu_{core}Au_{shell}$ tendency with the preference for centroid-(111)-facet occupation of Au atoms. The DFT calculations indicate that high HOMO-LUMO gaps often associate with structures having highly symmetric arrangements of Cu and Au atoms, but these structures are not necessarily most energetically stable. Cu-Au bond lengths are found to increase at the DFT level, making TO structures more distorted and promoting core-shell segregation. It is found by MPA that, charge transfer is governed in a complex way by cluster structure and individual atomic environment.

Dodecanethiol-stabilized Cu-Au nanoparticles having a range size of around 1-10 nm (2-5 nm are most frequent) were synthesized by a two-phase reaction method combined with a galvanic exchange procedure. After an investigation of morphological evolution stimulated by a strong TEM electron beam, cuboctahedron is found to be the thermodynamically stable morphology for the Cu-Au nanoparticles. Under the electron beam, cuboctahedral

nanoparticles can aggregate to form larger cuboctahedral particles. A mixed Cu-Au configuration is found by HAADF imaging and SDD-EDX elemental mapping for the cuboctahedral particles. It is also found by the elemental mapping that the Cu-Au nanoparticles are not significantly oxidized when exposed to ambient air. SPRs of the Cu-Au nanoparticles, investigated using plasmon-EELS beam positioning, are found to be strongly dependent on local morphologies and structures.

We used SDD-EDX elemental mapping, surface plasmon EELS, and tomography in HAADF-STEM mode to characterize the microbially synthesized bimetallic Pd-Au nanoparticles. Different compositional configurations of the bimetallic particles are reliably determined by utilizing HAADF contrast (Z-contrast and thickness contrast) combined with elemental mapping and plasmon-EELS beam-positioning. The configurations found include asymmetric segregation, homogenous mixing, $Pd_{core}Au_{shell}(Pd\text{-}Au)_{shell}$, and layered phase-segregation with a mixed interface. In accordance with the case of Cu-Au nanoparticles, the local structure dependence of SPRs is also observed in the Pd-Au nanoparticles. A tomogram which provides the 3D morphological information of a Pd-Au nanoparticle is achieved using HAADF-STEM tomography.

Inc-Ih-Mackay, inc-dou-pc5, bi-capped-TO, and c-Dh structural motifs with a $Pt_{core}Au_{shell}$ configuration are found in our theoretical study of $Pt_nAu_{40-n}$ clusters. At the DFT level, the $Pt_{core}Au_{shell}$ configuration is confirmed to be energetically favoured. The layered (phase-segregated) configuration is found to be more stable than the $Au_{core}Pt_{shell}$ and mixed configurations, consistent with an experiment in which $Au_{core}Pt_{shell}$ particles were observed to change to layer-segregated particles when annealed at 600$^{o}$C [30]. Electronic shell closure effects are observed in Inc-Ih-Mackay and inc-dou-pc5 structures which have large HOMO-LUMO gaps. Consistent with the case of the 38-atom Cu-Au clusters, structures having

highly symmetric atom arrangements are found to have abnormally large HOMO-LUMO gaps although these high gaps do not ensure high energetic stability. When investigated by MPA, charge transfer is again observed to be a complicated phenomenon highly sensitive to geometrical structure and individual atomic arrangement, neutralizing the Pt-Au electron transfer directed by the higher electronegativity of Au.

We synthesized PVP-stabilized Pt-Au nanoparticles by the polyol method and citrate-stabilized Pt-Au nanoparticles by Frens method combined with a successive reduction procedure. By using SDD-EDX elemental mapping, we found mixing, $Au_{core}Pt_{shell}$, and $Pt_{core}Au_{shell}$ tendencies corresponding to different sizes (~ 4, 8, and 12 nm, respectively) of the PVP-stabilized particles. These particles are also found to have decreasing Pt:Au compositional ratios when particle size increases. The citrate-stabilized particles are initially agglomerates with Au cores (~ 20 nm) coated by Pt aggregates (~ 3-4 nm). SDD-EDX elemental mapping confirms that well-defined $Au_{core}Pt_{shell}$ particles can be established under an adequate electron beam dose. However, the $Au_{core}Pt_{shell}$ particles are found to be unstable when irradiated further by the electron beam, with interdiffusion between the Au core and Pt shell indicated by the elemental mapping and line-scanning.

## 8.2. Future works

My thesis is going to be closed here with our computational studies, chemical syntheses, and TEM characterization of some gold containing bimetallic nanoparticles accomplished. However, we realize that there are further challenges opened, which may not be only of our interest but also of others' interest.

1. There is a size gap between our theoretical clusters and experimental nanoparticles. While the theoretical clusters are of a few tens (38, 40, and 54) of atoms, the

characterized nanoparticles are of roughly thousands of atoms. Directly or indirectly bridging this gap is desired. A direct bridge perhaps requires state-of-the-art characterizing instrumentation and further developments of computational technology. We would like to suggest that an indirect bridge can be made by some extrapolation of the experimental particle properties toward the size regime of the theoretical nanoclusters.

2. In our work, investigation of nanoparticle SPRs has been done by EELS beam-positioning. However, we suggest that nanoparticles can be more comprehensively investigated by EELS SPR-mapping which can reveal local structure and composition at high spatial resolution. The electronic structure of nanoparticles can also be studied using EELS. Knowledge of electronic structure is very important for applications of nanoparticles.
3. We encountered the complication of charge transfer in our theoretical studies of Cu-Au and Pt-Au clusters. The relation between charge transfer and stabilization of clusters has not been fully understood. We suggest that further investigations of charge transfer in clusters are needed and different charge population analyses (other than MPA) should be tested and compared.

# PUBLISHED/SUBMITTED PAPERS

1. Dung T Tran and Roy L Johnston, 2009, *Theoretical study of $Cu_{38-n}Au_n$ clusters using a combined empirical potential–density functional approach, Phys. Chem. Chem. Phys*., **11**, 10340

2. Dung T Tran, Ian P Jones, Roy L Johnston, Jon A Preece, and Coenraad R van den Brom, 2010, *Truncated-octahedral copper-gold nanoparticles*, *J. Phys.: Conf. Ser.*, **241**, 012086.

3. K. Deplanche, M. Merroun, M. Casadesus, D. T. Tran, I. M. Mikheenko, J. A. Bennett, I. P. Jones, J. A. Preece, R. L. Johnston, G. A. Attard, S. Selenska-Pobell and L. E. Macaskie, 2010, *Microbial synthesis of gold/palladium nanoparticles for applications in green chemistry* (submitted).

4. Dung T Tran and Roy L Johnston, 2010, *Study of 40-atom Pt-Au clusters using a combined empirical potential-density functional approach* (submitted)

5. Dung T Tran, Ian P Jones, Roy L Johnston, Jon A Preece, and Coenraad R van den Brom, 2010, *TEM characterisation of chemically-synthesized copper-gold nanoparticles* (submitted).

6. Dung T. Tran, Ian P. Jones, Jon A. Preece, Roy L. Johnston, Kevin Deplanche, and Lynne E. Macaskie, 2010, *Characterization of microbially synthesized Pd-Au nanoparticles using STEM-based techniques* (to be submitted).

# BIBLIOGRAPHY


1. I. Freestone, N. Meeks, M. Sax, and C. Higgitt. *Gold Bulletin*, 2007, **40**, 270.

2. M. Faraday, *Philos. Trans. R. Soc*. London, 1857, **147,** 145.

3. A. Einstein, *Ann. Phys*. 1905, **17**, 549.

4. G. Mie, *Ann. Phys,* 1908, **25**, 377.

5. R. Zsigmondy, 1906, *Z. Phys. Chem.* **56** 65.

6. R. Zsigmondy, 1926, *Nobel Lecture: Properties of Colloids*, Nobel Foundation.

7. W. Ostwald, 1914, *Die Welt der vernachlässigten Dimensionen*, Steinkopf, Dresden.

8. C.N.R. Rao, P.J. Thomas, and G.U. Kulkarni, 2007, *Nanocrystals: Synthesis, Properties and Applications*, Springer, Berlin.

9. R. Ferrando, J. Jellinek, and R. L. Johnston, 2008, *Chem. Rev.*, **108**, 845.

10. J. Turkevich, P. C. Stevenson, and J. Hillier, 1951, *Discuss. Faraday. Soc.*, **11**, 55.

11. G. Frens, 1973, *Nature: Phys. Sci*., **241**, 20.

12. M. Brust, M. Walker, D. Bethell, D. J. Schiffrin, and R. Whyman, 1994, *Chem. Commun*., 801.

13. G. Schmid, A. Lehnert, J.O. Malm, and J. O. Bovin. *Angew.Chem.Int.Ed*, 1991, **30**, 874.

14. Y-S Shon, G. B. Dawson, M. Porter, and R. W. Murray, *Langmuir*, 2002, **18**, 3880.

15. Schmid G, Ed., 2004, *Nanoparticles: From Theory to Application*, WILEY-VCH Verlag GmbH & Co. KGaA, Weinheim.

16. J. Jellinek and E. B. Krissinel, 1999, *Theory of Atomic and Molecular Clusters*, Springer, Berlin, 1999.

17. R. L. Johnston, 2002, *Atomic and Molecular Clusters*, Taylor and Francis, London.

18. M. Hosokawa, K. Nogi, M. Naito, and T. Yokoyama, 2007, *Nanoparticle Technology Handbook*, Elsevier, Oxford, 1st Ed.

19. S. Link and M. A. El-Sayed, 1999, *J. Phys. Chem. B*, ***103,*** 4212.

20. M. Haruta, 2003, *Chem. Record*, **3**, 75.

21. Ph. Buffat and J-P. Borel, 1976, *Phys. Rev. A*, **13**, 2287.

22. Z. Y. Li, N. P. Young, M. Di Vece, S. Palomba, R. E. Palmer, A. L. Bleloch, B. C. Curley, R. L. Johnston, J. Jiang, and J. Yuan, 2008, *Nature (Lett.)*, **451**, 46.

23. W.H. Qi and M.P. Wang, 2005, *J. Nanoparticle Res.*, **7**, 51.

24. D..M. Schaefer, A. Patil, R.P. Andres, and R. Reifenberger, 1995, *Phys. Rev. B*, **51**, 5322.

25. W.P. Halperin, 1986, *Rev. Mod. Phys.*, **58**, 533.

26. V. Volokitin, J. Sinzig, L. J. de Jongth, G. Schmid, M. N. Vargaftik, and I. I. Moiseev, 1996, *Nature*, **384**, 621.

27. F. Weigend and R. Ahlrichs, 2010, *Phil. Trans. R. Soc. A*, **368**, 1245.

28. K. Clemenger, 1985, *Phys. Rev. B*, **32**, 1359.

29. W. B. Pearson, Ed, 1972, *Crystal Chemistry and Physics of Metals and Alloys*, Wiley: New York.

30. N. Braidy, G.R. Purdy, and G.A. Botton., 2008, *Acta Materialia*, **56**, 5972.

31. D. Astruct, Ed., 2004, *Nanoparticles and catalysis*, 2008 WILEY-VCH Verlag GmbH & Co. KGaA, Weinheim

32. H. S. Oh, J. H. Yang, C. K. Costello, Y. M. Wang, S. R. Bare, H. H. Kung, and M. C. Kung, 2002, *J. Catal.*, ***210***, 375386.

33. M. C. Kung, R. J. Davis, and H. Kung, 2007, *J. Phys. Chem*., **111**, 1176711775.

34. M. Turner, V. B. Golovko, O. P. H. Vaughan, P. Abdulkin, and A. Berenguer-

Murcia, 2008, *Nature*, **454**, 981.

35. M. S. Tikhov, B. F. G. Johnson, and R. M. Lambert, 2008, *Nature*, **454**, 981.
36. S. Kidambi, J. Dai, J. Li, and M. L. Bruening, 2004, *J. Am. Chem. Soc.*, **126**, 2658
37. E. Schmidt, A. Vargas, T. Mallat, and A. Baiker, 2009, *J. Am. Chem. Soc.*, **131**, 12358.
38. C. Wang, M. Waje, X. Wang, J. M. Tang, R. C. Haddon, and Y. Yan, 2004, *Nano Lett.*, **4**, 345.
39. N. Tian, Z.-Y. Zhou, S.-G. Sun, Y. Ding, and Z. L. Wang, 2007, *Science,* **316,** 732.
40. V. R. Stamenkovic, B. Fowler, B. S. Mun, G. Wang, P. N. Ross, C. A. Lucas, and N. M. Marković, 2007, *Science,* **315**, 493.
41. C. Wang, H. Daimon, T. Onodera, T. Koda, and S. Sun, 2008, *Angew. Chem. Int. Ed.,* **47,** 3588.
42. S. Alayoglu, A. U. Nilekar, M. Mavrikakis, and B. Eichhorn, 2008, *Nature. Mater.*, **7**, 333.
43. P. Alivisatos, 2004, *Nat. Biotechnol., **22***, 47.
44. N. L. Rosi and C. A. Mirkin, 2005, *Chem. Rev., **105***, 1547.
45. H. Li and L. Rothberg, 2004, *Proc. Natl. Acad. Sci.*, **101**, 14036.
46. E. Kai, S. Sawata, K. Ikebukuro, T. Iida, T. Honda, and I. Karube, 1999, *Anal. Chem.,* **71**, 796.
47. S. J. Green, J. J. Stokes, M. J. Hostetler, J. J. Pietron, and R. W. Murray, 1997, *J. Phys. Chem.*, **B 101***,* 2663.
48. DI Gittins, D. Bethell*,* DJ Schiffrin, and RJ Nichols, 2000, *Nature*, **408,** 67.

49. V. V. Agarwal, R. Thomas, G. U. Kulkarni, and C. N. R. Rao, 2005, *Pramana - J. Phys*., **65**, 769.

50. D. L. Klein, R. Roth, A. K. L. Lim, A. P. Alivisatos, and P. L. McEuen, 1997, *Nature*, **389**, 699.

51. S. Sun, C. B. Murray, D. Weller, L. Folks, and A. Moser, 2000, *Science,* **287**, 1989.

52. J. Y. Ouyang, C. W. Chu, D. Sieves, and Y. Yang, 2005, *Appl*. *Phys*. *Lett*., **86**, 123507.

53. R. J. Tseng, J. Huang, J. Ouyang, R. B. Kaner, and Y. Yang, 2005, *Nano Lett.*, **5**, 1077.

54. I. Lee, F. Delbecq, R. Morales, M. A. Albiter, and F. Zaera, 2009, *Nature Mater.*, **8**, 132.

55. D. J. Wales, 2004, *Energy Landscape,* Cambridge University Press, Cambridge.

56. R. L. Johnston, 2003, *Dalton Trans.*, 4193.

57. D. J. Wales and J. P. K. Doye, 1997, *J. Phys. Chem. A***, 101**, 5111.

58. J. P. K. Doye and D. J. Wales, 1997, *J. Chem. Soc., Faraday Trans.*, **93**, 4233.

59. D. J. Wales and H. A. Scheraga, 1999, *Science*, **285**, 1368.

60. J. Jellinek and E. B. Krissinel, 1996, *Chem. Phys. Lett.*, **258**, 283.

61. J. H. Holland, 1975, *Adaptation in natural and artificial system,* Ann Arbor, The University of Michigan Press.

62. D. E. Goldberg, 1989, *Genetic Algorithms in Search, Optimization and Machine Learning*, Addison-Wesley, Reading, MA.

63. M. Mitchell, 1996, *An Introduction to Genetic Algorithms*, *MIT Press*, Cambridge, MA.

64. B. Hartke, 1993, *J. Phys. Chem.*, **97**, 9973.

65. Y. Zeiri, 1995, *Phys. Rev. E*, **51**, 2769.

66. R. H. Byrd, P. Lu, J. Nocedal and C. Zhu, 1995, *SIAM J. Sci. Comput.*, **16**, 1190.

67. D. M. Deaven and K. M. Ho,1995, *Phys. Rev. Lett.*, **75**, 288.

68. R. P. Gupta, 1981, *Phys. Rev. B*, **23**, 6265.

69. F. Cleri and V. Rosato, 1993, *Phys. Rev. B*, **48**, 22.

70. R. Ferrando, A. Fortunelli, and G. Rossi, *Phys. Rev. B*, 2005, **72**, 085449.

71. E.K.U. Gross and R.M. Dreizler, 1995, *Density Functional Theory*, NATO ASI Series B, **337**, Plenum Press, New York.

72. D.S. Sholl and J.A. Steckel, 2009, *Density Functional Theory: a practical introduction*, John Wiley & Sons, New Jersey.

73. R. G. Parr, and W. Yang, 1989, *Density-Functional Theory of Atoms and Molecules*, OUP, Oxford.

74. L. H. Thomas, 1927, *Proc. Cambridge Phil. Soc.* **23**, 542

75. E. Fermi, 1927, *Rend. Accad. Naz. Lincei*, **6**, 602.

76. P. Hohenburg and W. Kohn, 1964, *Phys. Rev. B*, **136**, 864.

77. W. Kohn and L. J. Sham, 1956, *Phys. Rev. A,* **140**, 1133.

78. W. Kohn, *Rev. Mod. Phys.,* 1999, **71**, 1253.

79. R. M. Dreizler and E. K. U. Gross, 1990, *Density Functional Theory*, Springer Verlag, Berlin.

80. J. P. Perdew and Y. Wang, 1986, *Phys. Rev.* B, **33**, 8800.

81. J. P. Perdew, 1991, *Electronic Structure of Solids 91*, Ed. P. Ziesche and H. Eschrig, Akademie Verlay, Berlin.

82. A. Khein, D. J. Singh, and C. J. Umrigar,1995, *Phys. Rev. B*, **51**, 4105.

83. J. Kuang and C. D. Lin, 1997, *J. Phys. B: At. Mol. Opt. Phys*. **30,** 2529.

84. R. Ferrando, R. L. Johnston, and A. Fortunelli, 2008, *Phys. Chem. Chem. Phys*, **10**, 640.

85. W. Koch and M. C. Holthausen, 2001, *A Chemist's Guide to Density Functional*, *Theory*, *2nd Ed.*, Wiley-VCH Verlag GmbH.

86. M. Pope and C. E. Swenberg, 1999, *Electronic Processes in Organic Crystals and Polymers,* 2nd Ed., Oxford University Press, New York.

87. R. S. Mulliken, 1955, *J. Chem. Phys.*, **23**, 1833.

88. I. G. Csizmadia, 1976, *Theory and Practice of MO Calculations on Organic* Molecules, Elsevier, Amsterdam.

89. C. J. Cramer, 2002, *Essentials of Computational Chemistry: Theories and Methods*, Wiley, New York.

90. G. Schmid and D. Fenske*,* 2010, *Phil. Trans. R. Soc. A*, **368**, 1207.

91. W. H. Binder, 2005, *Angew. Chem., Int. Ed. Engl.*, **44**, 5172.

92. B. L. Cushing, V. L. Kolesnichenko, and C. J. O'Connor, 2004, *Chem. Rev.,* **104**, 3893.

93. G. Madras and B. J. McCoy, 2002, *J. Chem. Phys.*, **117,** 8042.

94. H. Bönnemann and R. M. Richards, 2001, *Eur. J. Inorg. Chem.*, 2455.

95. N. Toshima and T. Yonezawa, 1998, *New J. Chem.*, 1179.

96. D. V. Goia and E. Matijevic, 1998, *New J. Chem., **22***, 1203.

97. X. Lu, H-Y. Tuan, J. Chen, Z-Y. Li, B. A. Korgel, and Y. Xia, 2007, *J. Am. Chem. Soc*., **129**, 1733.

98. K. Araki, E. Mizuguchi, H. Tanaka, T. Ogawa, 2006, *J. Nanosci. Nanotechnol.*, **6**, 708.

99. R.G. Nuzzo and D.L. Allara, 1983, *J. Am. Chem. Soc.,* **105**, 4481.

100. Y. Xia and G. M. Whitesides,1998, *Angew. Chem. Int. Ed.*, **37**, 550.

101. P. J. G. Goulet and R. B. Lennox, 2010, *J. Am. Chem. Soc.,* **132**, 9582.

102. J.R. Heath, C.M. Knobler, and D.V. Leff, 1997, *J. Phys. Chem.*, **101**, 189.

103. S. Chen, K. Huang, and J.A. Stearns, 2007, *Chem. Mater.*, **12,** 540.

104. M-C Daniel and D. Astruc, 2004, *Chem. Rev.*, **104***,* 293.

105. F. Fievet, J.P. Lagier, B. Blin, B. Beaudoin and M. Figlarz., 1989, *Sol. Stat. Ion.*, **32**, 198.

106. C. Ducamp-Sanguesa, R. Herrera-Urbina, and M. Figlarz, 1992, *J. Sol.Stat.Chem,* **100**, 272.

107. F. Fivet, J.P. Lapier, and M. Figlarz, 1989 *Mater. Res. Soc. Bull.*, 29 (1989)

108. R. Seshadri and C.N.R. Rao, 1994, *Mater. Res. Bull*., **29,** 795.

109. X. Yan, H. Liu, and K.Y. Liew, 2001, *J. Mater. Chem.*, **11,** 3387.

110. D. I. Garcia-Gutierrez, C. E. Gutierrez-Wing, L. Giovanetti, J. M. Ramallo-López, F. G. Requejo, and M. Jose-Yacaman, 2005, *J. Phys. Chem. B*, **109,** 3813.

111. N. Toshima and Y. Wang, 1993, *Chem. Lett.*, 1611.

112. E.A. Hauser and J.E. Lynn,1940, *Experiments in Colloid Chemistry*, McGraw-Hill, New York.

113. R.S. Miner, S. Namba, and J. Turkevich, 1981, in: *Proceedings of the 7th International Congress on Catalysis*, ed. T. Seiyama and K. Tanabe, Kodansha, Tokyo.

114. L. H. Lu, G. Y. Sun, H. J. Zhang, H. S. Wang, S. Q. Xi, J. Q. Hu, Z. Tian, and R. Chen, 2004, *J. Mater.Chem*., **14**, 1005.

115. M. Green and P. O'Brien, 2000, *Chem. Comm.*, 183.

116. M. Sarikaya, C. Tamerler, A. K.-Y. Jen, K. Schulten, and F. Baneyx, 2003, *Nat. Mater.*, **2**, 577.

117. K. Deplanche and L.E. Macaskie, 2008, *Biotech. Bioeng*, **99**, 1055.

118. T. Klaus, R. Joerger, E. Olsson and G. Granqvist, 1999, *Proc.Natl.Acad.Sci.U S A*. **96**,13611.

119. Y. Konishi, T. Tsukiyama, T. Tachimi, N. Saitoh, T. Nomura, and S. Nagamine, 2007, *Electrochimica Acta,* **53**, 186.

120. M. D. Redwood, K. Deplanche, V. S. Baxter-Plant, and L. E. Macaskie, *Biotech. Bioeng*, **99**, 2008, 1405.

121. K. Deplanche, R. D. Woods, I. P. Mikheenko, R. E. Sockett, and L. E. Macaskie, *Biotech. Bioeng*, **101**, 2008, 873.

122. I. Mikheenko, 2004, *Nanoscale palladium recovery*, PhD Thesis, University of Birmingham, UK.

123. D. B. Williams and C. B. Carter, 2009, *Transmission Electron Microscopy - a text book for Material Science.*, 2nd Ed., Springer.

124. Z. L. Wang, 2000, *J. Phys. Chem. B***, 104***,* 1153.

125. L. de Broglie, 1929, *Nobel Lecture: The wave nature of the electron*, Nobel Foundation.

126. E. Ruska, 1986, *Nobel Lecture: The development of the electron microscope and of electron microscopy*, Nobel Foundation.

127. W.L. Bragg, 1913, *Proc. Cambridge Phil. Soc.*, **17**, 43.

128. J. A. Ascencio, C. Gutiérrez-Wing, M. E. Espinosa, M. Marín, S. Tehuacanero, C. Zorrilla, and M. José-Yacamán, 1998, *Surf. Sci*., **396**, 349

129. A.V. Crewe, J.P.Wall, and J.P. Langmore, 1970, *Science*, **168**, 1138.

130. S. J. Pennycook, L. A. Boatner, 1988, *Nature*, **336**, 565.

131. S. J. Pennycook, D. E. Jesson, 1991, *Ultramicroscopy*, **37**, 14.

132. P.D. Nellist and S. J. Pennycook, 2000, *Advances in imaging and electron physics*, **113**, 147.

133. J. S. Rayleigh, 1896, *Phil. Mag.*, **42**, 167.

134. T. Epicier and S. Benlekbir, 2009, *STEM-HAADF in Materials Science* (link: http://www.mpq.univ-paris-diderot.fr/mpq/nanoalliages/Epicier.pdf )

135. P.W. Hawkes, 1992, in: *Electron Tomography: Three-Dimensional Imaging with the Transmission Electron Microscope*, ed. J. Frank, Plenum Press, New York, London.

136. R.A. Crowther, D.J. de Rosier and A. Klug, 1970, *Proc. Roy. Soc. Lond.*, **A317**, 319.

137. D.J. De Rosier and A. Klug, 1968, *Nature*, **217**, 130.

138. M. Weyland, 2002, *Topics Catal.*, **21**, 175.

139. P. A. Midgley and R. E. Dunin-borkowski, 2009, *Nat. Mater.*, **8**, 271.

140. P. A. Midgley, E. P. W. Ward, A. B. Hungría, and J. M. Thomas, 2007, *Chem. Soc. Rev.*, **36**, 1477.

141. A. J. Garratt-Reed and D. C. Bell, 2003, *Energy-Dispersive X-Ray Analysis in the Electron Microscope*, BIOS Scientific Publishers Limited.

142. P. Lechner, C. Fiorini, R. Hartmann, J. Kemmer, N. Krause, P. Leutenegger, A. Longoni, H. Soltau, D. Stötter, R. Stötter, L. Strüder, and U. Weber, 1996, *Nucl. Instr. Meth.*, **377**, 346.

143. L. Strüder and H. Soltau, 1995, *Radiation Protection Dosimetry*, **61**, 39.

144. http://www.oxford-instruments.com

145. R. F. Egerton, 1996, *Electron Energy Loss Spectroscopy in the Electron*

*Microscope*, 2nd Ed., Plenum, New York

146. R.F. Egerton, 2009, *Rep. Prog. Phys*., 72, 016502.

147. C. Colliex and O. Stephan, 2005, *Sub-nm Spatially Resolved Electron Energy-Loss Spectroscopy*, in *Hanbook of Microscopy for Nanotechnology*, Springer, US.

148. P. Drude, 1900, *Annalen der Physik,* **306**, 566.

149. M. Achèche, C. Colliex, H. Kohl, A. Nourtier and P. Trebbia, 1986, *Ultramicroscopy*, **20**, 99.

150. T. V. Shahbazyan and I. E. Perakis, 1998, *Phys. Rev. Lett.*, **81**, 3120.

151. C. Noguez, 2007, *J. Phys. Chem. C*, **111***,* 3806.

152. M. Bosman, V. J. Keast, M. Watanabe, A. Maaroof, and M. B. Cortie, 2007, *Nanotechnology*, **18**, 165505.

153. J. Nelayah, M. Kociak, O. Stéphan, F. J. García de Abajo, M. Tencé, L. Henrard, D. Taverna, I. Pastoriza-Santos, L. M. Liz-Marzán, and C. Colliex, 2007, *Nat. Phys.*, **3**, 348.

154. A. L. Koh, K. Bao, I. Khan, W. E. Smith, G. Kothleitner, P. Nordlander, Stefan A. Maier, and D. W. McComb, 2009, *Acsnano*, **3**, 3015.

155. M. J. López, P. A. Marcos, and J.A. Alonso, 1996, *J. Chem. Phys.*, **104**, 1056.

156. N. T. Wilson and R. L. Johnston, 2002, *J. Mater. Chem.*, **12**, 2913.

157. S. Darby, T. V. Mortimer-Jones, R. L. Johnston, and C. Roberts, 2002, *J. Chem. Phys.*, **116**, 1536.

158. R. A. Lordeiro, F. F. Guimaraes, J. C. Belchior, and R. L. Johnston, 2003, *Int. J. Quant. Chem.*, **95**, 112.

159. G. Rossi, A. Rapallo, C. Mottet, A. Fortunelli, F. Baletto, and R. Ferrando, 2004,

*Phys. Rev. Lett.*, **93**, 105503.

160. A. Rapallo, G. Rossi, R. Ferrando, A. Fortunelli, B. C. Curley, L. D. Lloyd, G. M. Tarbuck, and R. L. Johnston, 2005, *J. Chem. Phys.*, **122**, 194308.

161. P. J. Hsu and S.K. Lai, 2006, *J. Chem. Phys.*, **124**, 044711.

162. X. Wu, W. Cai, and X. Shao, 2009, *J. Comput. Chem.*, **30**, 1992.

163. G. Barcaro, A. Fortunelli, G. Rossi, F. Nita, and R. Ferrando, 2006, *J. Phys. Chem. B*, **110**, 23197.

164. E. M. Fernández, L.C. Balbás, L. A. Pérez, K. Michaelian, and I. L. Garzón, 2005, *Int. J. Mod. Phys. B*, **19**, 2339.

165. D. C. Rodrigues, A. M. Nascimento, H. A. Duarte, andJ. C. Belchior, 2008, *Chem. Phys.*, **349**, 91.

166. E. J. Bylaska, W. A. de Jong, N. Govind, K. Kowalski, T. P. Straatsma, M. Valiev, D. Wang, E. Apra, T. L. Windus, J. Hammond, P. Nichols, S. Hirata, M. T. Hackler, Y. Zhao, P.-D. Fan, R. J. Harrison, M. Dupuis, D. M. A. Smith, J. Nieplocha, V. Tipparaju, M. Krishnan, Q. Wu, T. Van Voorhis, A. A. Auer, M. Nooijen, E. Brown, G. Cisneros, G. I. Fann, H. Fruchtl, J. Garza, K. Hirao, R. Kendall, J. A. Nichols, K. Tsemekhman, K. Wolinski, J. Anchell, D. Bernholdt, P. Borowski, T. Clark, D. Clerc, H. Dachsel, M. Deegan, K. Dyall, D. Elwood, E. Glendening, M. Gutowski, A. Hess, J. Jaffe, B. Johnson, J. Ju, R. Kobayashi, R. Kutteh, Z. Lin, R. Littlefield, X. Long, B. Meng, T. Nakajima, S. Niu, L. Pollack, M. Rosing, G. Sandrone, M. Stave, H. Taylor, G. Thomas, J. van Lenthe, A. Wong, and Z. Zhang, 2007, *NWChem, A Computational Chemistry Package for Parallel Computers, Version 5.1*, Pacific Northwest National Laboratory, Richland, Washington, USA, 99352.

167. J.P. Perdew, J.A. Chevary, S.H. Vosko, K.A. Jackson, M.R. Pederson, D.J. Singh, and C. Fiolhais, 1992, *Phys. Rev. B,* **46**, 6671.

168. A. Schäfer, C. Huber, and R. Ahlrichs, 1994, *J. Chem. Phys*, **100**, 5829.

169. D. Andrae, U. Haeussermann, M. Dolg, H. Stoll, and H. Preuss, 1990, *Theor. Chim. Acta.,* **77**, 123.

170. F. Weigend, M. Häser, H. Patzelt, and R. Ahlrichs, 1998, *Chem. Phys. Lett.*, 1998, **294**, 143.

171. F. Weigend and R. Ahlrichs, 2005, *Phys. Chem. Chem. Phys.*, **7**, 3297.

172. http://www.ipc.uni-karlsruhe.de/tch/tch1/TBL/tbl.html

173. W. J. Stevens, M. Krauss, H. Bausch, and P. G. Jasien, 1992, *Can. J. Chem.,* **70**, 612.

174. F. Weigend, 2006, *Phys. Chem. Chem. Phys.,* **8**, 1057.

175. ftp://ftp.chemie.uni-karlsruhe.de/pub/jbasen/cu

176. C. Elsässer, M. Fähnle, C. T. Chan, and K. M. Ho, 1994, *Phys. Rev. B*, **49**, 13975.

177. R. W. Warren and B. I. Dunlap, 1996, *Chem. Phys. Lett.*, **262**, 384.

178. E. Aprà and A. Fortunelli, 2003, *J. Phys. Chem. A,* **107**, 2934.

179. http://www.bear.bham.ac.uk

180. L. O. Paz-Borbón, R. L. Johnston, G. Barcaro, and A. Fortunelli, 2008, *J. Chem. Phys.*, **128**, 134517.

181. I. L. Garzón, K. Michaelian, M. R. Beltrán, A. Posada-Amarillas, P. Ordejón, E. Artacho, D. Sánchez-Portal, and J. M. Soler, 1998, *Phys. Rev. Lett.*, **81**, 1600.

182. E. Aprà, F. Baletto, R. Ferrando, and A. Fortunelli, 2004, *Phys. Rev. Lett.*, **93**, 065502.

183. J. M. Soler, M. R. Beltrán, K. Michaelian, I. L. Garzón, P. Ordejón, D. Sánchez-Portal, and E. Artacho, 2000, *Phys. Rev. B*, **61**, 5771.

184. S. Olivier, R. Conte, and A. Fortunelli, 2008, *Phys. Rev. B*, **77**, 054104.

185. A. J. Cohen and N. C. Handy, 2000, *Chem. Phys. Lett.*, **316**, 160.

186. F. Y. Chen and R. L. Johnston, 2008, *Acta Materialia*, **56**, 2374.

187. C. L. Bracey, P. R. Ellis, and G. J. Hutchings, 2009, *Chem. Soc. Rev.*, **38**, 2231.

188. W. Yoo and C. Li, 2007, *Tetrahedron Lett.*, **48**, 1033.

189. A. Corma and H. Garcia, 2008, *Chem. Soc. Rev.*, **37**, 2096.

190. T. Mitsudome, A. Noujima, T. Mizugaki, K. Jitsukawaa, and K. Kaneda, 2009, *Chem. Commun.*, 5302.

191. B. Zhu, Q. Guo, X. Huang, S. Wang, S. Zhang, S. Wu and W. Huang, 2006, *J. Mol. Catal. A: Chem.*, **249**, 211.

192. H. Mori, M. Komatsu, K. Takeda, H. Fujita, 1991, *Philos. Mag. Lett.,* **63**, 173.

193. H. Yasuda, H. Mori, M. Komatsu, K. Takeda, and H. Fujita, 1992, *J. Electron. Microsc.,* **41**, 267.

194. H. Yasuda and H. Mori, 1994, *Z. Phys. D*, **31**, 131.

195. H. Yasuda and H. Mori, 1996, *Z. Phys. D*, **37**, 181.

196. K. Fukumi, A. Chayahara, K. Kadono, T. Sakaguchi, Y. Horino, M. Miya, K. Fujii, and J. Hayakawa, 1994, *J. Appl. Phys.*, **75**, 3075.

197. D. Lu and K. Tanaka, 1997, *Phys. Rev. B.*, **55**, 13685.

198. F. Gonnella, G. Mattei, P. Mazzoldi, C. Sada, G. Battaglin, and E. Cattaruzza, 1999, *Appl. Phys. Lett.*, **75**, 55.

199. B. Pauwels, G. Van Tendeloo, E. Zhurkin, M. Hou , G. Verschoren, L. Theil Kuhn, W. Bouwen, P. Lievens, 2001, *Phys. Rev. B*, **63**, 165406.

200. C. Maurizio, G. Mattei, P. Mazzoldi, S. Padovani, E. Cattaruzza, F. Gonella, F. D'Acapito and F. Zontone, 2003, *Nucl. Instrum. Methods Phys. Res., Sect. B*, **200**, 178.

201. U. Pal, J. F. Sanchez Ramirez, H. B. Liu, A. Medina, and J. A. Ascencio, 2004, *Appl. Phys. A*., **79**, 79.

202. A. K. Sra and R. E. Schaak, 2004, *J. Am. Chem. Soc.*, **126**, 6667.

203. R. E. Schaak, A. K. Sra, B. M. Leonard, R. E. Cable, J. C. Baur, Y.-F. Han, J. Means, W. Teizer, Y. Vasquez and E. S. Funck, 2005, *J. Am. Chem. Soc.*, **127**, 3506.

204. A. K. Sra, T. D. Ewers and R. E. Schaak, 2005, *Chem.Mater.,***17**, 759.

205. T. D. Castillo-Castro, E. Larios-Rodriguez, Z. Molina-Arenas, M. M. Castillo-Ortega and J. Tanori, 2006, *Composites, Part A*, **38**, 107.

206. J. A. Ascencio, H. B. Liu, U. Pal, A. Medina, and Z. L. Wang, 2006, *Micro. Res. Tech*., **69**, 522.

207. M. D. Abramoff, P. J. Magelhaes, and S. J. Ram, 2004, *Biophotonics International*, **11**, 36.

208. H.S. von Harrach, B. Freitag, W. Gerits, A. Sandborg, 2003, *Micron*, **34**, 185.

209. D. J. Smith, A. K. Petford-Long, R. L. Wallenberg, and J. O. Bovin, 1986, *Science*, **233**, 872.

210. H. B. Liu, J. A. Ascencio, M. Pérez, and M. José-Yacamán, 2001, *Surf. Sci.*, **491**, 88.

211. H. B. Liu, R. Perez , G. Canizal, and J. A. Ascencio, 2002, *Surf. Sci.*, **518**, 14.

212. H. B. Liu, M. José-Yacamán, R. Pérez, and J. A. Ascencio, 2003, *Appl. Phys. A, Mater. Sci. Process*, **77**, 63.

213. B. Pauwels, G. Van Tendeloo, W. Bouwen, L. Theil Kuhn, P. Lievens, H. Lei, and M. Hou, 2000, *Phys. Rev. B,* **62**, 10.

214. J. L. Plaza, P. M. Mendes, S. Diegoli, Y. Chen, J. A. Preece, and R. E. Palmer, 2005, *Nanosci. Nanotech.,* **5**, 1826.

215. M. Watanabe, A. Burrows, A. A. Herzing, C. J. Kiely, D. B. Williams, G. Hutchings, and L. M. Liz-Marzin, 2004, *Microscopy and Microanalysis*, **10**, 468.

216. P. Kanninen, C. Johans, J. Merta, and K. Kontturi, 2008, *J. Colloid. Interface. Sci*., **318**, 88.

217. E. Cattaruzza, G. Battaglin, F. Gonella, R. Polloni, B. F. Scremin, G. Mattei, P. Mazzoldi, and C. Sada, 2007, *App. Surf. Sci.*, **254**, 1017.

218. P. Kanninen, C. Johans, J. Merta, and K. Kontturi, 2008, *J. Colloid. Interface. Sci*., **318**, 88.

219. J.K. Edwards, B. Solsona, P. Landon, A.F. Carley, A. Herzing, M. Watanabe, C.J. Kiely, and G.J. Hutchings, 2005, *J. Mater. Chem*., **15**, 4595.

220. B.E. Solsona, J.K. Edwards, P. Landon, A.F. Carley, A. Herzing, C.J. Kiely, and G.J. Hutchings, 2006, *Chem. Mater,* **18**, 2689.

221. D. I. Enache, J. K. Edwards, P. Landon, B. E. Solsona, A. F. Carley; A. Herzing, M. Watanabe, C. J. Kiely, D. W. Knight, and G. J. Hutchings, 2006, *Science*, **311**, 362.

222. P. Dash, N. A. Dehm, and R. J. Scott, 2008, *J. Mol. Cat. A: Chem*, **286**, 114.

223. M. Nakanishi, H. Takatani, Y. Kobayashi, F. Hori, R. Taniguchi, A. Iwase, and R. Oshima, 2005, *Appl. Surf. Sci.*, **241,** 209.

224. H. Nitani, M. Yuya, T. Ono, T. Nakagawa, S. Seino, K. Okitsu, Y. Mizukoshi, S.

Emura, and T.A. Yamamoto, 2006, *J. Nanoparticle Res.*, **8**, 951.

225. T. Akita, T. Hiroki, S. Tanaka, T. Kojima, M. Kohyama, A. Iwase, and F. Hori, 2008, *Catalysis Today*, **131**, 90.

226. N. Taguchi, F. Hori, T. Iwai, A. Iwase, T. Akita, and S. Tanaka, 2008, *App. Surf. Sci.*, **255**, 164.

227. J. Turkevich and G. Kim, 1970, *Science*, **169**, 873.

228. M. Harada, K. Asakura, and N. Toshima, 1993, *J. Phys. Chem.*, **97**, 5103.

229. G. Schmid, H. West, J.-O. Malm, J.-O. Bovin, and C. Grenthe, 1996, *J. Chem. Eur.*, **2**, 1099.

230. H. Bönnemann, W. Brijoux, 1999, In *Metal Clusters in Chemistry*, P. Braunstein, L. A. Oro, P. R. Raithby, Eds., Wiley-VCH: Weinheim, Germany, **2**, 913.

231. G. Schmid, 1999, In *Metal Clusters in Chemistry*, P. Braunstein, L. A. Oro, P. R. Raithby, Eds., Wiley-VCH: Weinheim, Germany, **3**, 1325.

232. H. Remita, M. Mostafavi, and M. O. Delcourt, 1996, *Radiat. Phys. Chem.*, **47**, 275.

233. E. Pérez-Tijerina, M. Gracia-Pinilla, S. J. Mejia-Rosales, U. Ortiz-Méndez, A. Torres, M. José-Yacamán, 2008, *Faraday Discuss,* **138**, 353.

234. D. Ferrer, D. A. Blom, L. F. Allard, S. J. Mejia-Rosales, E. Pérez-Tijerina, M. José-Yacamán, 2008, *J. Mater. Chem.*, **18**, 2442.

235. J. A. Ascencio, H. B. Liu, U. Pal, and R. J. Perez, 2006, *Phys. Chem. B,* **110**, 5191.

236. F. Pittaway, L. O. Paz-Borbón, R. L. Johnston, H. Arslan, R. Ferrando, C. Mottet, G. Barcaro, and A. Fortunelli, 2009, *J. Phys. Chem. C*, **113**, 9141.

237. D. W. Yuan, X. G. Gong, and R. Wu, 2007, *Phys. Rev. B,* **75**, 085428.

238. N. Taguchi, A. Iwase, N. Maeda, T. Kojima, R. Taniguchi, S.Okuda, T.Akita, T. Abe, T. Kambara, H. Ryuto, and F. Hori, 2009, *Rad. Phys. Chem.*, **78**, 1049.

239. J-B. Park, J. H. Lee, and H-R. Choi, 2007, *App. Phys. Lett.,* **90**, 093111.

240. S. Benlekbir, T. Epicier, M. Bausach, M. Aouine, and G. Berhault, 2009, *Phil. Mag. Lett.,* **89**, 145.

241. B. Schaffer, U. Hohenester, A. Trügler, and F. Hofer, 2009, *Phys. Rev. B*, **79**, 041401

242. B. Schaffer, W. Grogger, G. Kothleitner, and F. Hofer, 2010, *Ultramicroscopy,* **110**, 1004.

243. K. Deplanche, 2008, *New nanocatalysts made by bacteria from metal solutions and recycling of metal wastes*, PhD thesis, University of Birmingham, UK.

244. N. Kawase, M. Kato, H. Nishioka, and H. Jinnai, 2007, *Ultramicroscopy*, **107**, 8.

245. C. Messaoudi, T. Boudier, C. O. Sanchez-Sorzano CO, and S. Marco, 2007, *BMC Bioinformatics*., **8**, 288.

246. R. Gordon, R. Bender and G.T. Herman, 1970, *J. Theor. Biol.*, **29**, 471.

247. A.C. Kak and M. Slaney, 2001, *Principles of Computerized Tomographic Imaging (Classics in Applied Mathematics)*, **346**, SIAM, Philadelphia, PA-USA.

248. E. F. Pettersen, T. D. Goddard, CC. Huang, G. S. Couch, D. M. Greenblatt, E. C. Meng, and T. E. Ferrin, 2004, *J. Comput. Chem.*, **13**, 1605.

249. M. Stöger-Pollach, 2008, *Micron*, **39**, 1092.

250. E. Hutter and J. H. Fendler, 2004, *Adv. Mater.*,**16**, No.19, 1685.

251. S. Chen and K. Huang, 2000, *J. Clust. Sci*., **11**, No. 3, 405.

252. R. Tatumi, T. Akitab, and H. Fujihara, 2006, *Chem. Commun*., 3349.

253. L. Jia, Q. Zhang, Q. Li, and H. Song, 2009, *Nanotechnology*, **20**, 385601.

254. T. Azzam, L. Bronstein, and A. Eisenberg, 2008, *Langmuir*, **24**, 6521.

255. N. Toshima, M. Harada, Y. Yamazaki, and K. Asakura, 1992, *J. Phys. Chem*., **96**, 9927.

256. H. Takatani, H. Kago, M. Nakanishi, Y. Kobayashi, F. Hori, and R. Oshima, 2003, *Rev. Adv. Mater. Sci.*, **5**, 232.

257. J-S. Lim, S-M. Kim, S-Y. Lee, E. A. Stach, J. N. Culver, and M. T. Harris, 2010, *J. Nanomaterials.* (doi:10.1155/2010/620505).

258. H. Okamoto, T. B. Massalski, 1985, *Bull Alloy Phase Diagrams*, **6**, 46.

259. J. Luo, M. M. Maye, V. Petkov, N. N. Kariuki, L. Wang, P. Njoki, D. Mott, Y. Lin, and C. J. Zhong, 2005, *Chem. Mater*., **17**, 3086.

260. C. Mihut, C. Descorme, D. Duprez, and M. D. Amiridis, 2002, *J. Catal.*, **212**, 125.

261. G. Selvarani, S. V. Selvaganesh, S. Krishnamurthy, G. V. M. Kiruthika, P. Sridhar, S. Pitchumani, and A. K. Shukla, 2009, *J. Phys. Chem. C*, **113**, 7461.

262. B. L. Abrams, P. C. K. Vesborg, J. L. Bonde, T. F. Jaramillo, and I. Chorkendorff, 2009, *J. Electrochem Soc.*, **156**, 273.

263. D. F. Yancey, E. V. Carino, and R. M. Crooks, 2010, *J. Am. Chem. Soc.*, **132**, 10988.

264. D. Dai and K. Balasubramanian, 1994, *J. Chern. Phys*., **100**, 4401.

265. W. Q. Tian, M. Ge, F. Gu, T. Yamada, and Y. Aoki, 2006, *J. Phys. Chem. A***, 110***,* 6285.

266. Q. Ge, C. Song, and L. Wang, 2006, *Comput. Mater. Sci.*, ***35***, 247.

267. A. Logsdail, L. O. Paz-Borbón, and Roy L. Johnston, 2009, *J. Comp. Theor. Nanosci.*, **6**, 857.

268. Dung T. Tran and Roy L. Johnston, 2009, *Phys. Chem. Chem. Phys*., **11**, 10340.

269. C. Kittel, 1996, *Introduction to Solid State Physics*, 7th Ed., John Wiley & Sons.

270. P. Hernández-Fernández, S. Rojas, P. Ocón, J. L. de la Gómez Fuente, J. San Fabián, J. Sanza, M. A. Peña, F. J. García-García, P. Terreros, and J. L. G. Fierro, *J. Phys. Chem. C,* 2007, **111**, 2913.

271. J. T. Zhang, H. Y. Ma, D. J. Zhang, PP. Liu, F. Tian, andY. Ding, 2008, *Phys. Chem. Chem. Phys.*, **10**, 3250.

272. Z. M. Peng and H. Yang, *Nano. Res*., 2009, **2**, 406.

273. G.C. Bond, C. Louis, and D.T. Thompson, *Catalysis by Gold*, I.C. Press, London, 2006.

274. M. J. Hostetler, C. J. Zhong, B. K. H. Yen, J. Anderegg, S. M. Gross, N. D. Evans, M. Porter, and R. W. Murray, 1998, *J. Am. Chem. Soc.***, 120**, 9396.

275. J. Belloni, M. Mostafavi, H. Remita, J-L. Marignier, and M-O. Delcourt, 1998, *New J. Chem., **22***, 1239.

276. A. Henglein, 2000, *J. Phys. Chem. B*, **104**, 2201.

277. D. Garcia-Gutierrez, C. Gutierrez-Wing, M. Miki-Yoshida, and M. Jose-Yacaman, 2004, *Appl. Phys. A*, **79**, 481.

278. P. Jiang, J-J. Zhou, R. Li, Z-L. Wang, and S-S. Xie, 2006, *Nanotechnology*, **17**, 3533.

279. C. P. Liu, R. D. Twesten, and J. M. Gibson, 2001, *Ultramicroscopy*, **87**, 79.